



POLITECNICO
MILANO 1863

SCUOLA DI INGEGNERIA INDUSTRIALE
E DELL'INFORMAZIONE

Techno-economic optimization of a modular CSP tower plant of 5 MW_{el}

TESI DI LAUREA MAGISTRALE IN
ENERGY ENGINEERING
INGEGNERIA ENERGETICA

Author: **Luca Corradini**

Student ID: 10571936

Advisor: Prof. Giampaolo Manzolini

Co-advisors: Giancarlo Gentile, Ettore Morosini

Academic Year: 2021-22

Abstract

This thesis work compares different modular concentrated solar power (CSP) tower plants with their corresponding single field counterparts. For the modular configurations different heliostat dispositions and module sizes are investigated. Two ranges of operating temperatures are also considered. Sodium is adopted as heat transfer fluid (HTF), advanced molten salts are used as storage media, and a supercritical CO₂ cycle is considered for the 5 MW_{el} power block. Solar field, receiver, piping system, thermal energy storage (TES) system and power block are modelled to design and evaluate the performances of the plant. The piping system model is developed as part of this thesis work. For each configuration, tower height and receiver area are determined by optimization of the levelized cost of heat (LCOH). The solar multiple and the TES size of each configuration are determined by optimization of the levelized cost of electricity (LCOE). The identified best modular plant, consisting of 10 polar field modules, each one of 5 MW_{th} of incident power on the receiver, achieves a LCOE value of 143.6 \$/MWh, a reduction of 6.5 % with respect to the LCOE provided by the corresponding best single field plant.

Key-words: CSP, solar tower, modular plant, techno-economic optimization, LCOE

Abstract in italiano

Questo lavoro di tesi considera diverse possibili configurazioni per la modularizzazione di un impianto solare a concentrazione (CSP). Le configurazioni modulari sono confrontate con dei corrispondenti impianti a singola torre. Due diversi intervalli di temperatura sono analizzati per il funzionamento dell'impianto. Sodio liquido è adottato come fluido termovettore (HTF), per l'accumulo di calore vengono utilizzati sali fusi, e un ciclo a CO₂ supercritico è utilizzato per il blocco di potenza da 5 MW_{el}. Campo solare, ricevitore, sistema di tubazioni, sistema di accumulo e blocco di potenza sono modellizzati per il design e l'analisi delle prestazioni dell'impianto. Il modello del sistema di tubazioni è stato sviluppato durante questo lavoro di tesi. Per ogni configurazione l'altezza della torre e le dimensioni del ricevitore sono determinate dall'ottimizzazione del costo livellato del calore (LCOH). Il multiplo solare e le dimensioni del sistema di accumulo sono determinati, per ogni configurazione, in base all'ottimizzazione del costo livellato dell'energia (LCOE). Il miglior impianto modulare individuato consiste in 10 moduli, ognuno da 5 MW_{th} al ricevitore, e raggiunge un LCOE di 143.6 \$/MWh, una riduzione del 6.5 % rispetto al valore di LCOE ottenuto con un corrispondente impianto a singola torre.

Parole chiave: solare a concentrazione, torre solare, modularizzazione, ottimizzazione techno-economica, LCOE

Contents

Abstract	i
Abstract in italiano	iii
Contents	v
1 Introduction	1
1.1. Structure and objectives of the work.....	1
1.2. Energy sector.....	3
1.3. CSP state of the art	7
1.4. Modular tower plants.....	14
2 Modelling	31
2.1. Overview	31
2.2. Solar field.....	32
2.3. Receiver.....	38
2.4. Piping	46
2.5. TES and PB	59
2.6. Annual simulation	60
2.7. Economic parameters	64
3 Case Study	67
3.1. Overview	67
3.2. Jemalong pilot plant.....	69
3.3. Part I - Cornfield module	71
3.4. Part II - Module optimization.....	74
4 Results	77
4.1. Part I – Cornfield module	77
4.2. Part II – Module optimization	88
5 Conclusion	105
Bibliography	107
A Appendix A	113
List of Figures	119
List of Tables	125

1 Introduction

1.1. Structure and objectives of the work

The present work focuses on the techno-economic optimization of a modular concentrated solar power (CSP) tower plant and its comparison with a single tower plant. The aim of the work is to evaluate the possible advantages and disadvantages of adopting a modular configuration with respect to a single solar field plant, both from a thermodynamic and economic point of view. The work is divided into 5 chapters.

In this chapter (Chapter 1) it is presented the current situation of the energy sector: the energy sources that are now employed to satisfy the world electricity demand and the increasing penetration of renewable sources, in the context of the human driven climate changes that the world is facing. In the first chapter concentrated solar power technologies are presented and especially the state of the art for plants based on solar towers. The available literature on modular tower plants and the existing pilot plants are also analysed.

Chapter 2 explains more in detail the employed tools and the methodology adopted. The models used and implemented for the design and the simulation of the CSP systems are described, in particular regarding the modelling of the solar field, the receiver, and the piping system. In this chapter also the assumed economic parameters are discussed.

Chapter 3 focuses on the case study which is the subject of the analysis of this work: a 5-megawatt electric (MW_{el}) modular tower plant with different investigated configurations for the modules with the aim of optimizing the plant as much as possible. The optimization was based on the levelized cost of heating (LCOH) and the levelized cost of electricity (LCOE).

The results for the considered configurations are reported and analysed in chapter 4 and they are compared with the results of the single tower plant. Finally in chapter 5 the conclusive considerations and the future work perspectives are given.

This thesis presents multiple elements of innovation that have both theoretical and practical applications. These include:

- The implementation of a complete and flexible piping model for the evaluation of thermal and pressure losses.

- The identification of more advantageous alternatives in the design of CSP tower plants which can serve as guidelines for future projects and designs.

In Figure 1 it is summarized the workflow of the presented thesis work.

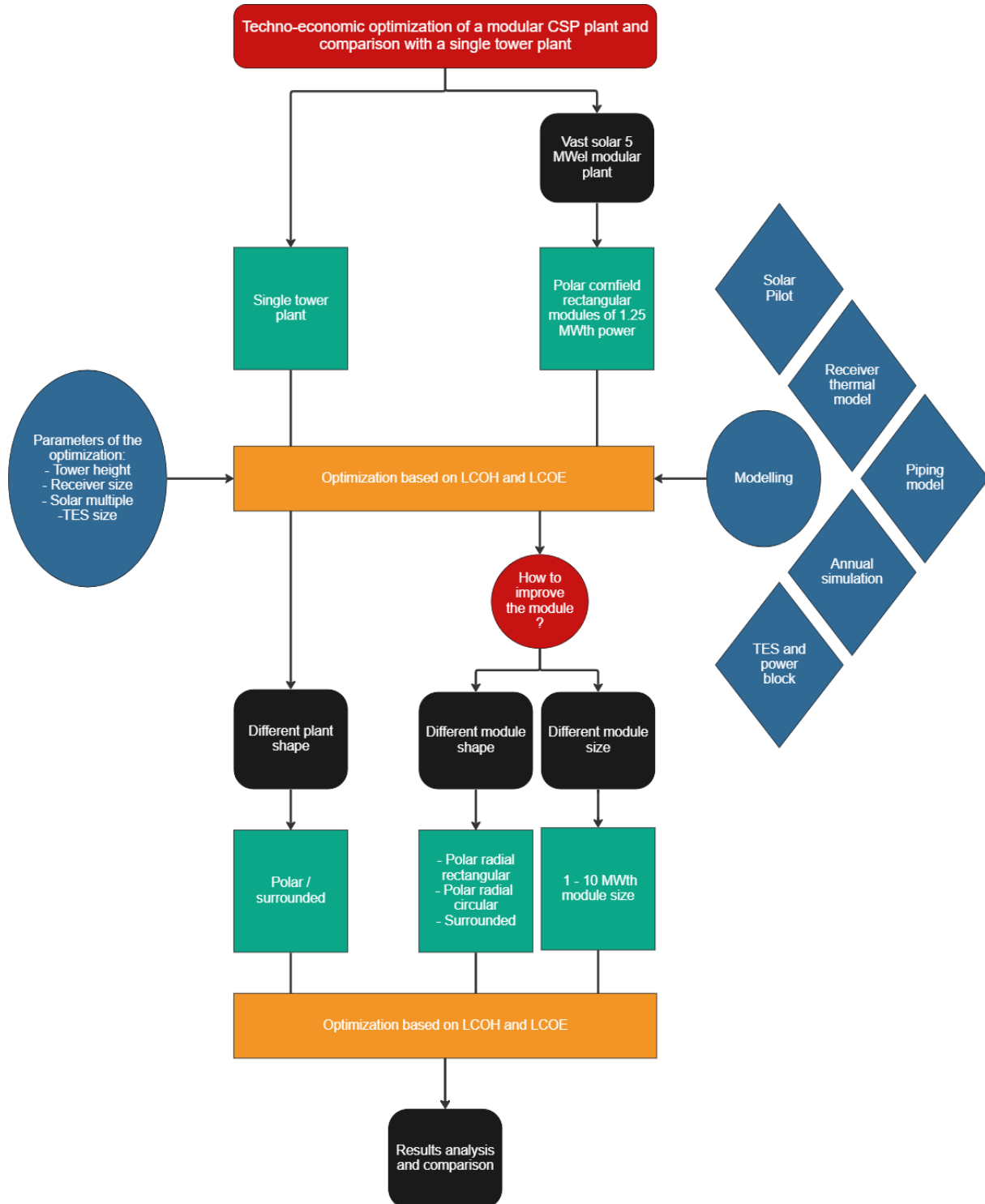


Figure 1 Workflow of the thesis work

1.2. Energy sector

The world primary energy demand in 2021 was 595 exajoule (EJ). Primary energy demand grew by 31 EJ in 2021 with respect to 2020: this was the largest increase in history, and it reversed and overcame the sharp decline seen in 2020 due to the COVID-19 pandemic. In 2021 fossil fuels accounted for more than 80 % of global primary energy consumption, while hydroelectricity (6.8 %), nuclear energy (4.3 %) and renewables (6.7 %) covered the remaining share [1].

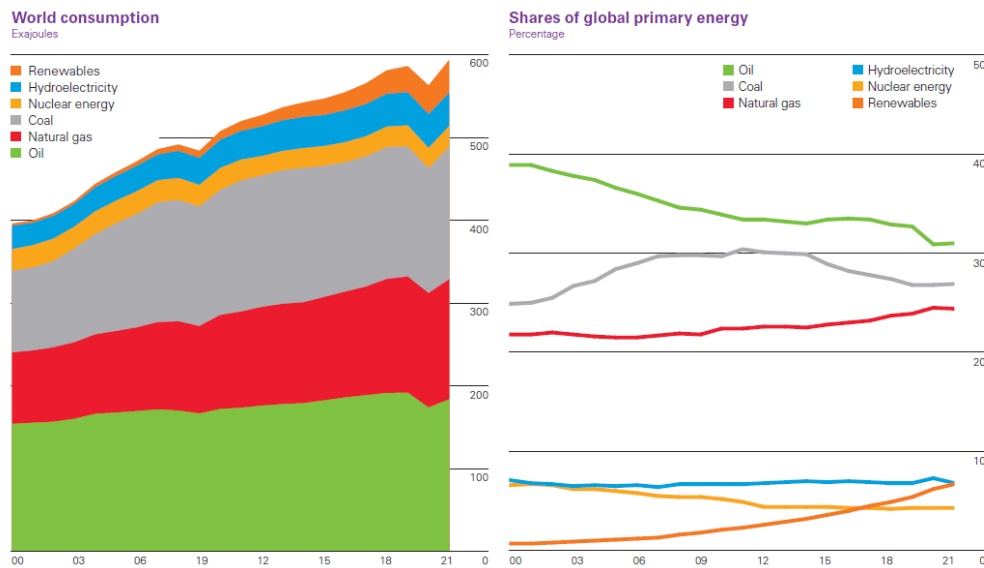


Figure 2 World primary energy consumption by source [1]

The most important sector when discussing energy consumption is the power generation sector, as electrification is the key for the transition from fossil fuels to renewable sources. In 2021 62% of the electricity was generated from fossil fuels, mainly coal (36%) and gas (22%). Nevertheless, solar and wind capacity continued to grow rapidly, increasing by 226 GW [1]. Solar generation rose by 23% in 2021, and wind by 14%. Combined, this took them to more than 10% of global electricity generation. All clean electricity sources generated 38% of the world’s electricity in 2021. Coal power rose by 9.0% in 2021 more-than rebounding from a 4.2% fall in 2020. It was the biggest percentage rise on record since at least 1985. Coal power rose in 2021 because clean electricity was not deployed quickly enough to keep up with unprecedented demand growth. Despite a record rise in wind and solar generation, only 29% of the global rise in electricity demand in 2021 was met with wind and solar. Remaining demand increase was therefore met by fossil fuels (Figure 3) [2].

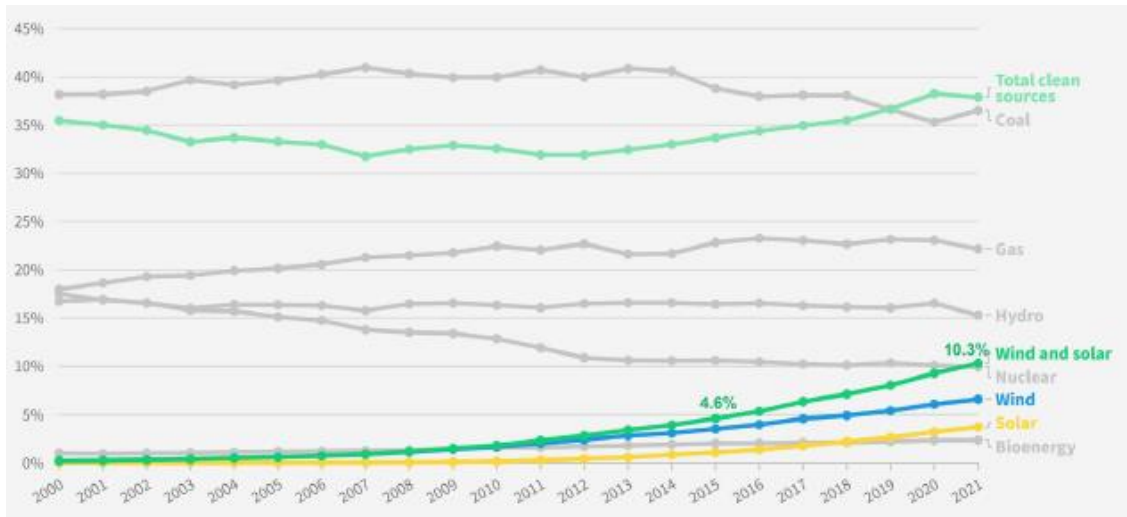


Figure 3 Share of global electricity generation by source [2]

Emerging technologies still provide no meaningful electricity generation, including fossil fuels with carbon capture, hydrogen-based fuels, concentrated solar power (CSP), geothermal and marine. These other technologies generally complement, rather than compete with, wind and solar. In particular, they provide benefits to the grid to support the variability of wind and solar. Stalling on these complementary technologies will make it even more difficult to achieve the emissions cuts needed and it would likely increase the cost of reaching zero carbon power production [2], as it will be discussed later in this Chapter.

Energy-related and industrial process CO₂ emissions rebounded by 1.9 Gt in 2021, the largest ever annual rise in emissions, with global CO₂ emissions in 2021 totalling 36.6 Gt [3]. CO₂ emissions are directly related to the greenhouse effect and the increase in global temperatures: in 2011-2020 the increase in global surface temperature was assessed at 1.09 °C above 1850–1900 level, and the consequences can already be observed all over the world. For the future three possible scenarios are reported and discussed. The stated policies scenario (STEPS) would lead to a 2.5 °C temperature rise in 2100. In the announced pledges scenario (APS) the projected global median temperature rise in 2100 is about 1.7 °C. This gets close to achieving the goal of the Paris Agreement to limit the temperature rise to “well below 2 °C”. However warming of close to 2 °C would still entail strong negative impacts for societies around the world. In the net zero emissions (NZE) by 2050 scenario the global temperature rise peaks below 1.6 °C around 2040, before dropping to around 1.4 °C in 2100. As a result, the NZE Scenario falls within the group of scenarios categorised by the International Panel on Climate Change (IPCC) as a “no or low overshoot” scenario, and aligns with the goal, agreed in Glasgow at COP26 in 2021, to “pursue efforts to limit the temperature increase to 1.5 °C” (Figure 4) [3] [4].

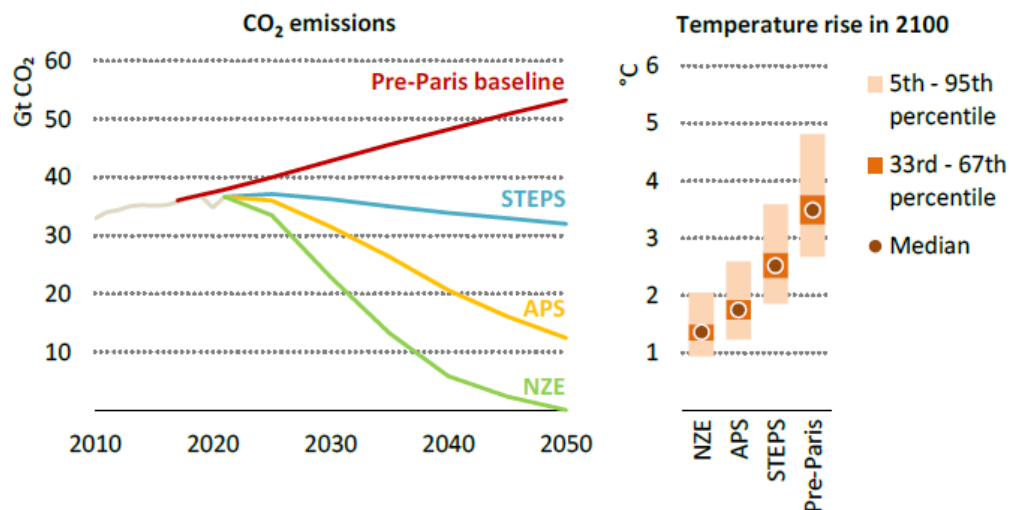


Figure 4 Energy-related and process CO₂ emissions, 2010-2050 and temperature rise in 2100 by scenario [3]

The 1.09 °C increase reached in global surface temperature has already led to significant consequences. Human-induced climate change, including more frequent and intense extreme events, has already caused widespread adverse impacts and related losses and damages to nature and people, beyond natural climate variability. The rise in weather and climate extremes has led to some irreversible impacts as natural and human systems are pushed beyond their ability to adapt. Global warming, reaching 1.5°C in the near-term, would cause unavoidable increases in multiple climate hazards and present multiple risks to ecosystems and humans. Near-term actions that limit global warming to close to 1.5°C would substantially reduce projected losses and damages related to climate change in human systems and ecosystems, compared to higher warming levels, but cannot eliminate them all [4].

There are many uncertainties in the future of the energy sector, but one point which is common to all the scenarios is the rising share of electricity in global final energy consumption. This is associated with a huge overall increase in global electricity demand over the coming decades. Deployment of solar PV and wind power accelerates in all scenarios. Within ten years, if countries are taking the necessary action to deliver on their climate pledges, the world will be deploying around 210 gigawatts (GW) of wind capacity each year and 370 GW of solar. Electricity is the first energy sector to reach net zero emissions, and that helps bring about emissions reductions in other sectors as they increasingly look to electricity to meet rising demand for energy services (Figure 5) [3].

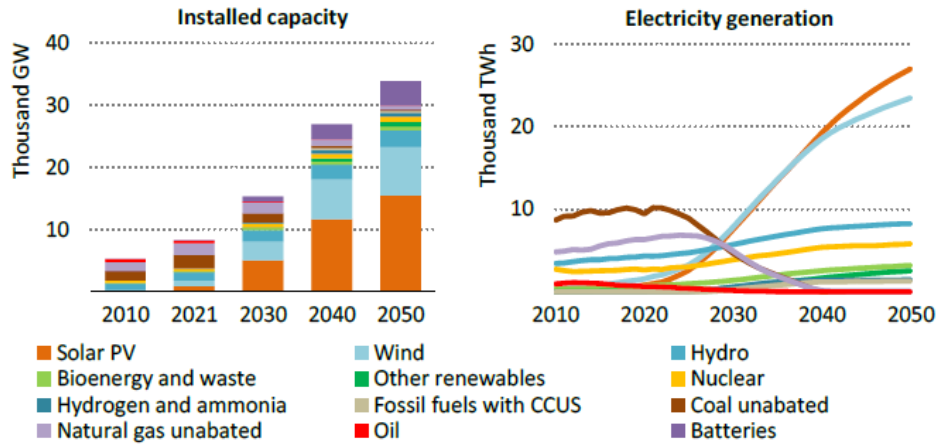


Figure 5 Total installed capacity and electricity generation by source in the NZE scenario, 2010-2050 [3]

The huge rise in the share of solar PV and wind in total generation in all scenarios fundamentally reshapes the power system and significantly increases the demand for power system flexibility to maintain electricity security. Electricity supply has always required the capability to meet demand continuously, down to the scale of seconds or less, in order to maintain system stability. Most of the flexibility required to maintain power system reliability today is provided by dispatchable thermal power plants and hydropower. Sharply rising flexibility needs and changes in the composition of the power plant fleet, with the phase-out of large unabated coal-fired thermal power stations in many regions, see the share of flexibility demand served by thermal power plants drop significantly (Figure 6) [3].

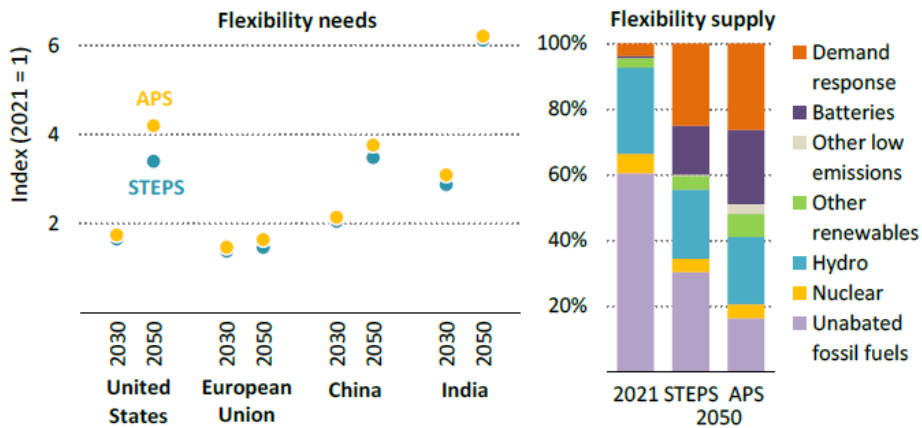


Figure 6 Flexibility needs and supply by region and scenario [3]

This increases the need for alternative sources of flexibility to maintain grid stability and security of supply. Reinforced power grids and additional interconnections can help even out fluctuations in the supply of weather-dependent variable renewables, within and between countries and regions. Certain grid assets, such as high voltage direct current interconnections, can also provide flexibility services like fast ramping or voltage control directly. Demand-side response is another emerging option for the

provision of electricity system flexibility. It helps to align consumption with the available supply, reducing the need for other sources of flexibility [3].

All three scenarios show battery storage emerging as an important flexibility option in power systems characterised by high shares of variable renewables. This growth reflects its increasingly important role in helping to integrate rising shares of solar PV and wind by regularly charging at times of plentiful renewables supply and discharging when most needed in the system. Battery storage is also able to bolster the stability and reliability of electricity networks, for example by providing fast frequency response. Other storage technologies also play important roles: pumped hydro is the largest source of electricity storage today and is set to increase further over the next ten years. Hydrogen and ammonia are emerging as solutions for the seasonal storage of renewable electricity. In this frame CSP technologies can play a relevant role as they represent a complementary renewable source to solar PV and wind, and they can also provide additional flexibility and stability to the grid thanks to thermal energy storage.

1.3. CSP state of the art

Concentrating solar power plants use mirrors to concentrate the sun rays. In most systems today, this heats a fluid used to produce power-generating steam. CSP plants then generate electricity in a similar way to conventional power stations, using steam turbines. The inclusion of thermal energy storage (TES) with a CSP plant offers a particular advantage relative to variable-generation renewable technologies such as photovoltaics and wind. By integrating CSP with TES, the variability of generation associated with the intermittency of the solar resource is eliminated to a large extent. CSP-TES provides additional benefits, including dispatchable high-value energy, operating reserves, and reliable system capacity. The dispatchability of CSP results in energy production during periods of highest demand, offsetting the more costly (and higher emissions) fossil generators. CSP can also ramp rapidly, providing multiple ancillary services such as regulation and spinning reserves [5].

The first CSP plants were built in the 1980s in the Mojave Desert in California. After a lull in activity during the 1990s, there was a renaissance for the technology in the 2000s driven by support policies that resulted in commercial projects in Spain and the United States. As a result, these two countries accounted for around 88% of total installed capacity globally at the end of 2015. During the last years emerging markets with high solar resources like Morocco, the United Arab Emirates, South Africa and Chile have started to gain momentum in terms of CSP deployment and plans [6].

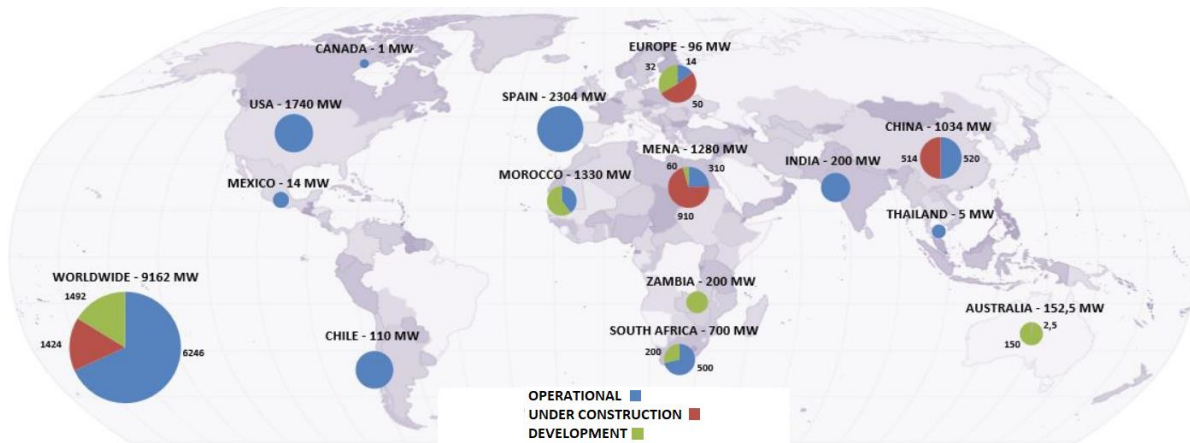


Figure 7 CSP projects around the world, 2020 [7]

In 2021, the global market for concentrating solar thermal power contracted for the first time since the commercial establishment of the industry in the 1980s, to reach a total cumulative capacity of 6 GW. This contraction occurred as the launch of the long-awaited 110 MW Cerro Dominador plant in Chile was offset by the decommissioning of nearly 300 MW of older CSP units in the United States. Growth in the global CSP market has trended downwards since 2015, despite consistent cost declines during this period. The recent decline is due largely to inactivity in the two countries with the most CSP installations, Spain and the United States, which added no new capacity for eight and six years, respectively, because of policy changes, project failures and competition from solar PV (Figure 8). Some market recovery was expected in 2022 with the addition of 750 MW of new capacity in China and the United Arab Emirates. Crucial to scaling the sector are policies that place greater value on the flexibility of CSP with thermal energy storage (TES), as well as continued efforts to reduce costs and increase capacity factors. Around 70% of the CSP capacity under construction in 2021 was based on parabolic trough technology, with the rest based on tower systems. The facilities under construction will include 8.8 GWh of TES capacity [8].

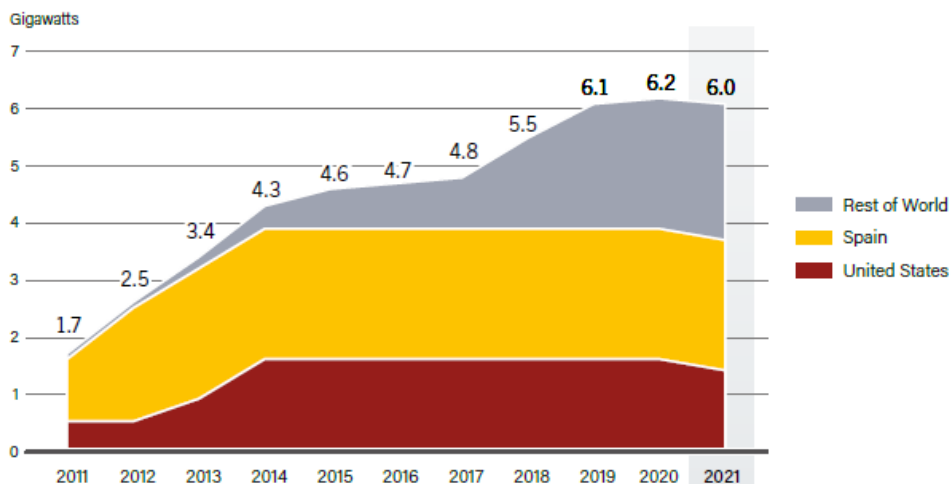


Figure 8 Concentrated solar thermal power global capacity, by country and region [8]

CSP costs continued to decline during the years reaching nearly a 70% decrease in average CSP costs during the decade ending in 2020 (Figure 9). Multiple factors have contributed to these declines, including technological innovation, improved supply chain competitiveness, and the growing CSP capacity in regions with high solar irradiance (which, along with increased TES capacity, has boosted the overall capacity factor of the global CSP fleet). The ability for CSP with TES to compete with other power technologies is influenced strongly by the structure of power auctions and procurement processes, and the value placed on specific benefits of these systems in terms of dispatch flexibility and capacity factor. CSP with TES has high potential to enhance power systems that incorporate large volumes of variable renewable power based on solar PV and wind [8]. Considering the assessment of the net system cost, that includes comparisons of both costs and grid-wide system benefits of different technologies, CSP configurations compare very favourably against both the conventional alternatives, such as natural gas power plants, and PV plants with batteries [5].

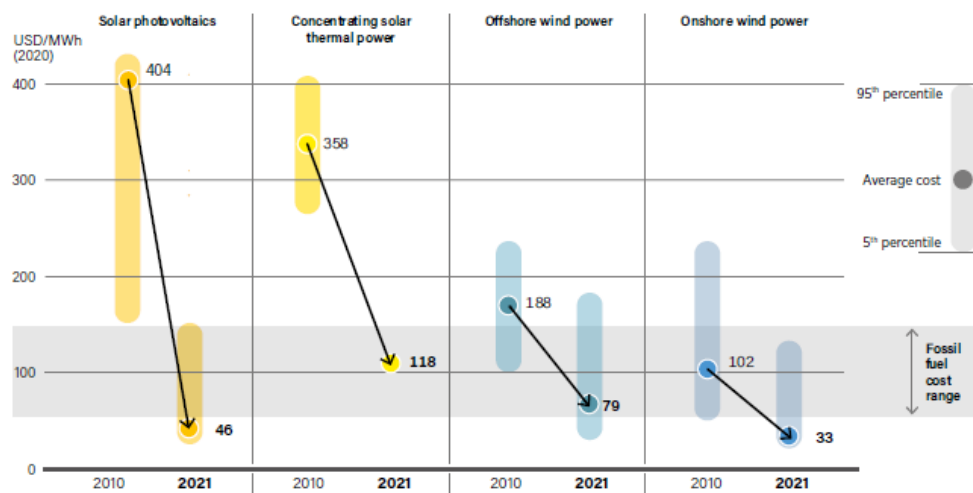


Figure 9 Global weighted-average LCOEs from newly commissioned, utility scale renewable power generation technologies [8]

At present, there are four main CSP technology families, which can be categorised by the way they focus the sun’s rays and the technology used to receive the sun’s energy (Figure 10). Parabolic troughs are the most mature of the CSP technologies and form the bulk of current commercial plants. Solar towers, also known as central receiver systems (CRS), use hundreds or thousands of small reflectors (called heliostats) to concentrate the sun’s rays on a central receiver placed atop a fixed tower. Power-tower CSP plants can achieve higher-temperature operation when compared to line-focus systems such as parabolic trough and linear Fresnel plants. These higher temperatures yield greater thermal-to-electric conversion efficiencies in the power block and can result in lower costs for storage. In addition, the concept is highly flexible; designers can choose from a wide variety of heliostats, receivers, transfer fluids and power blocks [6].

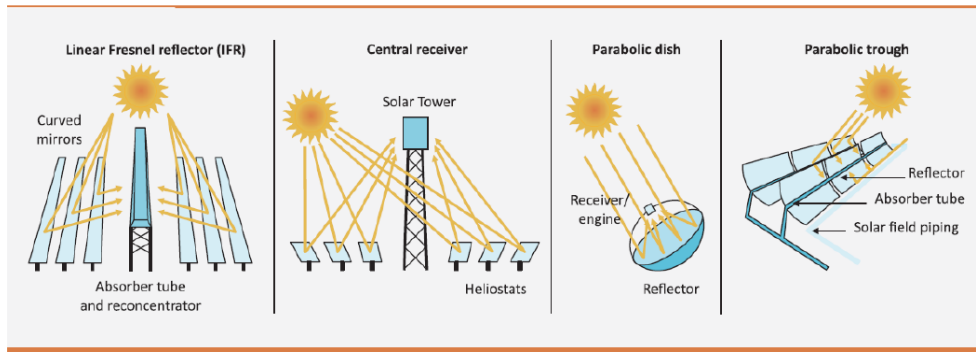


Figure 10 Main CSP technologies [6]

In direct-steam power towers, heliostats reflect sunlight onto a steam receiver located at the top of a tower. The receiver in a direct-steam power tower is similar in function to a boiler in a conventional coal-fired Rankine-cycle power plant. The feed water, pumped from the power block, is evaporated and superheated in the receiver to produce steam, which is then fed into a turbine/generator to generate electricity. Current steam conditions for direct-steam towers range from saturated steam at 250°C to superheated steam at over 550°C. Figure 11 shows a photo of the Ivanpah Solar Electric Generating System, which consists of three direct-steam power towers and more than 170,000 heliostats (each 15 m²), with a capacity of 390 MW_{el}. Although short-duration direct-steam/water storage has been demonstrated for steam-based towers, e.g., the 20-MW PS20 tower plant in Spain, the greater levels of storage necessary to provide firm capacity are currently considered cost prohibitive [5].



Figure 11 The Ivanpah Solar Electric Generating System

Molten-salt (MS) technology using nitrate salts in tubular external receivers is the current state-of-the-art CSP technology, operating at hot-salt temperatures of approximately 565°C. The hot salt is held in a storage tank, and when electric power generation is required, the hot salt is pumped to the steam generator to produce high-

pressure steam at nominal conditions of 100–150 bar and up to 540°C. The steam is converted to electrical energy in a conventional steam turbine/generator. By placing the storage between the receiver and the steam generator, solar energy collection is decoupled from electricity generation. The combination of salt density, salt specific heat, and temperature difference between the two tanks allows economic storage capacities of up to 15 hours of turbine operation at full load. Such a plant could run 24 hours a day, 7 days a week in the summer and part-load in the winter. Currently, there are very few commercial MS power towers that use this technology: Gemasolar (Spain, 19 MW_{el}, 15 hours TES), Crescent Dunes (Tonopah, Nevada, 110 MW_{el}, 10 hours TES), NOOR III (Morocco, 150 MW_{el}, 7 hours TES), Cerro Domindor (Chile, 110 MW_{el}, 17.5 hours TES), Shouhang Dunhuang Phase II (China, 100 MW_{el}, 11 hours TES). All these plants also use molten salts as storage medium for direct thermal energy storage (Figure 12) [5].

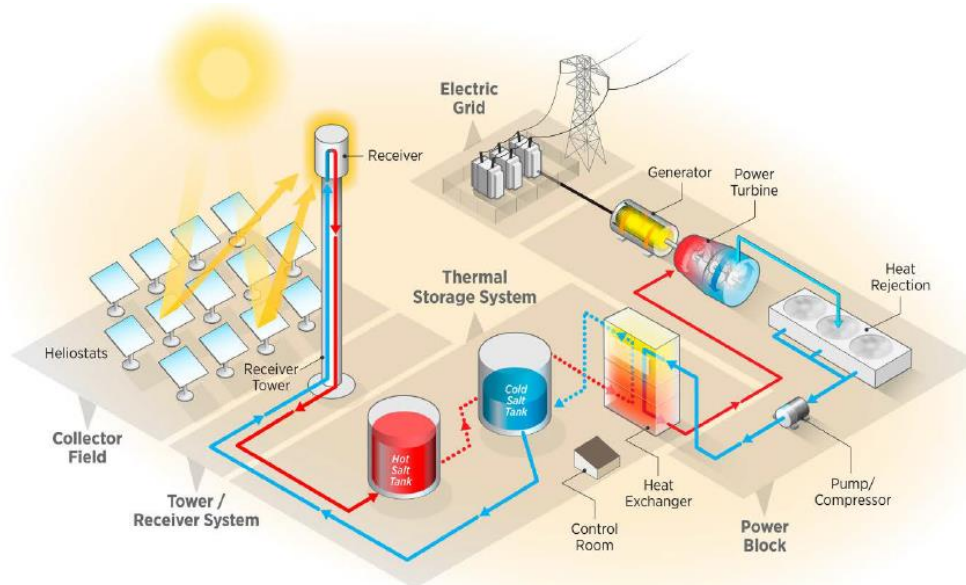


Figure 12 Molten-salt power tower with direct storage of salts [5]

A key driver for improving performance is through efficiency gains brought about by integrating CSP solar fields with advanced power cycles, with a leading candidate for CSP applications being the supercritical carbon dioxide (sCO₂) Brayton power cycle. To reach the desired efficiency of 50% these sCO₂ systems are expected to run at temperatures as high as 750°C, employing power blocks of 20 MW or greater. As such, this condition excludes parabolic trough, linear Fresnel, and dish systems as advanced, high-temperature power-tower systems are best positioned to deliver this high-temperature energy input to the sCO₂ power block [5].

Supercritical CO₂ Brayton-cycle energy conversion systems transform heat energy to electrical energy through the use of sCO₂ rather than through steam-Rankine cycle systems commonly used in today's CSP, coal, nuclear, and combined-cycle gas plants. Past studies indicate that the closed loop sCO₂ cycle offers the potential of higher cycle

efficiency versus superheated or supercritical steam cycles at temperatures relevant for CSP applications. Brayton-cycle systems using sCO₂ have a smaller weight and volume, lower thermal mass, and less complex power blocks versus Rankine cycles due to the higher density of the fluid and simpler cycle design. The simpler machinery and compact size of the sCO₂ process may also reduce the installation, maintenance, and operation cost of the system [5].

Cycle configurations such as the partial-cooling cycle and recompression with main compression intercooling, together with reheat, appear able to reach 50% efficiency, even when combined with dry cooling. As such, the U.S. Department of Energy (DOE) has selected the cycle as the leading candidate for achieving the target of 6 ¢/kWh for the overall cost of a CSP solar tower plant. To achieve these efficiencies, high temperatures ($\geq 700^{\circ}\text{C}$) are required. Such higher temperatures will require alternative HTFs to today's molten nitrate salts, which are limited to temperatures lower than 600°C . Particle, advanced molten-salt, and/or gas-phase HTFs and associated receivers are all technology pathways with the potential to deliver these high temperatures [5].

High-temperature particle receivers can increase the operating temperature of CSP systems above conventional molten-nitrate salt systems, improving solar-to-electric efficiency and lowering costs. Particle receivers are currently being designed and tested for operating temperatures above 700°C that can provide heat for inexpensive direct storage, thermochemical reactions, and process heat. Unlike conventional receivers that employ fluid flowing through tubular receivers, particle receivers use solid particles that are heated, either directly or indirectly by concentrated sunlight. Once heated, the particles may be stored in an insulated tank and used to heat a secondary working fluid (e.g., steam, CO₂, air) for the power cycle (Figure 13). Particle receivers have the potential to increase the maximum temperature of the heat-transfer media to over $1,000^{\circ}\text{C}$. Thermal energy storage costs can be significantly reduced by directly storing heat at higher temperatures in a relatively inexpensive medium (i.e., sand-like particles). Because the solar energy can be directly absorbed in the particles, the flux limitations associated with tubular central receivers (high stresses resulting from the containment of high-temperature, high-pressure fluids) are significantly relaxed [5].

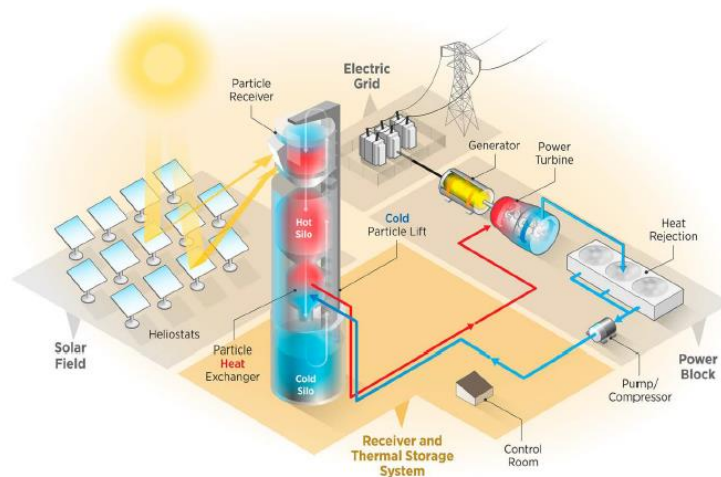


Figure 13 Falling particle receiver system with integrated storage and heat exchange for a power cycle [5]

Gas-phase (GP) receivers use a stable, intermediate-pressure, heat-transfer fluid in a closed-loop configuration to transfer energy to and from thermal storage. In the suggested configuration, a CO₂, helium, argon, or mixed GP fluid is circulated at intermediate pressure (on the order of 75 bar) through a receiver with relatively small flow channels, either small-diameter tubes, microchannels, or other geometries, and heated to temperatures sufficient to generate the target of 700°C sCO₂ after heat exchange into the power cycle (e.g., ~750°C). The hot fluid is transported down the tower to the TES system, which can be one of a variety of technologies. After charging the storage, the cooled fluid is again circulated through the receiver. Power generation is decoupled from thermal energy collection by the TES system. One possible system configuration that makes use of phase-change material (PCM) TES is illustrated in Figure 14 [5].

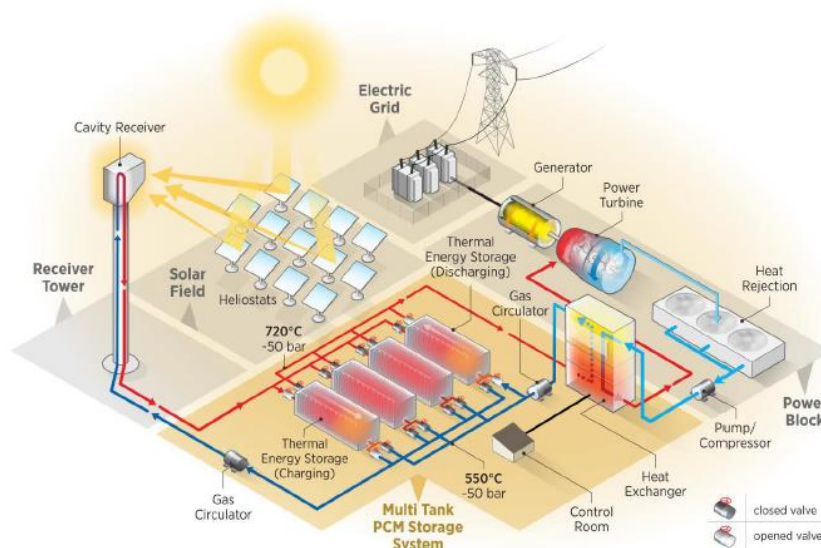


Figure 14 Conceptual design of gas-phase receiver system with a modular indirect PCM thermal storage system [5]

1.4. Modular tower plants

The concept of modular solar tower plants is still in a very early stage of development: very few research articles are available in literature and very few pilot projects have been realized. The current designs of CSP commercial tower plants are always tailor made in contrast to parabolic plants, which are quite modular allowing the increasing of the electricity production simply by implementing a larger number of collector loops. A study by *Lim et al. (2017)* [9] underlines how modular systems are being introduced in power generation technologies including wind turbines, solar PV and nuclear reactors. This is driven by the potential to lower the cost by mass production of standardized components of much smaller scale. Other advantages are claimed with the use of lower cost materials, which offers the potential for additional options to identify the economic optimum in LCOE. The complexity and technical challenges of construction are also lower for smaller modular CSP systems. In addition, for a large power plant with multiple modules, there is no need to shut down the entire plant in the event where there is a problem with one of the modules. This provides greater flexibility when operating a power plant. Another potential advantage is that the power station can be constructed in stages, therefore allowing cash-flow to be generated in stages.

Nevertheless, these potential advantages must be compared against the disadvantages that include an increase in operations and maintenance (O&M) costs, an increase in the number of components, and an increase in the thermal and parasitic losses due to an increase in surface area to volume ratio associated with reduced thermal scale of the components. Therefore, the trade-off between the aforementioned pros and cons for modular CSP systems has to be evaluated.

A study by *Crespo et al. (2020)* [10] points out the advantages of splitting the size of the heliostat field- receiver subsystems to avoid the impact on performance of enlarging surrounding fields, particularly in hazy locations. The limitation in size of tower plants mainly regards the atmospheric attenuation (or extinction) factor, as for large plants the reflected rays must go across a very long distance to impinge into the receiver. Solar energy is abated around one third in the few kilometers range and the extinction impact is greater at ground level. Therefore, heliostats much further away from the receiver see their efficiency significantly reduced. Modular systems are investigated in different research articles in combination with a range of different technologies such as particle receivers, PCM storage systems, solar combined cycles. A summary of the main research articles is reported in Table 1.

Research article	Plant technology	Plant configuration	Results
Tyner et al. (2013) [11]	Molten salts Direct TES	50 MW _{th} receivers 14 modules 13 h TES 2.5 SM	Annual solar to electric efficiency 15.8 %
Crespo et al. (2018) [12]		50 MW _{el} modules 2 modules	10.4 % less heliostats 2 % CAPEX savings
Puppe et al. (2018) [13]		140 MW _{th} receivers 5 modules 12 h TES	7 % higher LCOE
García Barberena et al. (2013) [14]	Decoupled solar combined cycle (DSCC)	32 modules 9 h TES 2.1 SM	LCOE 113 \$/MWh
Sorbet et al. (2018). [15]		14 modules	LCOE 128 \$/MWh
Rea et al. (2018). [16]	Solar Thermal to Electricity via Advanced Latent heat Storage (STEALS)	400 kW _{el} modules 5 h TES	LCOE 95 \$/MWh
Lindquist et al. (2019) [17]		13 kW _{el} modules 13 h TES	LCOE 77 \$/MWh

Table 1 Summary of research articles on modular solar tower plants

A study from *Tyner et al. (2013)* proposes the design of a molten salt system based on a 50-MW_{th} module comprised of a tower-mounted molten salt receiver surrounded by heliostats as illustrated in Figure 15. A hexagonal field layout is found to be close to the optimal circle in terms of optical performance, while allowing better packing of an array of fields and significantly improving field piping layouts and decreasing piping costs. The chosen field layout has a 1:1 aspect ratio, a small north field bias, and 44% heliostat density, and uses 2.2 m² heliostats. Although lower field densities give slightly better optical efficiency, the denser packing significantly decreases wind loads within the fields (because of self-shielding), allowing much lower-cost heliostats and improving overall plant economics significantly. The denser packing also shortens piping runs and reduces the effects of spillage. A small amount of mirror curvature is found to improve performances and is incorporated in the design.

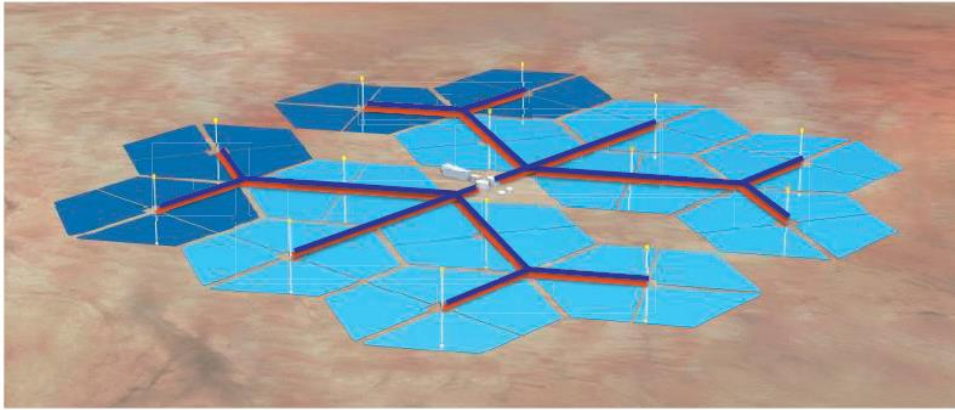


Figure 15 Modular field layout

The module size is optimized to allow a range of plant sizes and capacity factors using a replicated single module design, but not so many as to unduly complicate operations. While the projected LCOE is relatively flat for modules between 40 and 60 MW_{th}, the final selection of a 50-MW_{th} receiver and module is determined by the maximum receiver size that can ship fully assembled without excessive over-size shipping costs. A 100-MW power block rating is chosen as the basis for the primary configuration, while a 50-MW power block is selected for smaller plants. Three different tower configurations are considered, including lattice, concrete, and steel monopole. It is concluded that, for the selected module size, the monopole tower is the lowest cost configuration satisfying performance requirements and available from many suppliers leveraging the wind industry's well established supply chain. Tower height is optimized given the selected field configuration and receiver size. The obtained 100 m tower was relatively tall for this field size because of the high heliostat density. The receivers, rated at 50 MW_{th} absorbed power, are external, salt-in-tube, consisting of panels arranged in a box configuration.

The salt piping system includes all piping, supports, insulation, heat trace, and valves necessary to transport the cold salt from the cold salt pumps to the receiver inlet vessels and return it from the receivers to the hot salt storage tank. A 14-module, 75% capacity-factor plant requires about 10,000 m of cold salt piping and 17,000 m of hot salt piping. While overall the field piping contributes about 1% to total thermal energy losses, adds a few percent to overall plant capital costs, and adds slightly to the plant parasitic load (0.3% of total gross annual production). The field piping is made by insulated carbon steel for cold salt and insulated stainless steel for hot salt. The piping system is electrically heat traced to provide freeze protection of the molten salt and to preheat the empty pipes from ambient to minimum operating temperature during startup.

The TES system uses nitrate salt (60 wt % NaNO₃, 40 wt % KNO₃) which also serve as the heat transfer fluid. Each tank is about 39 m in diameter and 17.5 m tall. The cold tank shell is made of carbon steel and has an operating temperature of 288°C and a maximum temperature of 400°C. The hot tank's shell is made of stainless steel and has

an operating temperature of 565°C and a maximum temperature of 593°C. A 14-tower, 75% capacity factor plant requires about 36,500 tonnes of salt to provide 3500 MWh of storage (enough to run the 100-MW turbine generator at full power for 13.1 h). The power generation system includes a Rankine-cycle reheat steam turbine generator and the design main and reheat operating pressures and temperatures are 127 bar, 539°C and 28 bar, 538°C, respectively. For a baseload plant with a desired capacity factor of 75%, the optimized solar multiple is 2.5 and storage size is about 13 hours. For a 50% capacity factor plant, the solar multiple is about 1.8 with about 6 hours of storage. Solar multiple can be easily adjusted by changing the number of modules. For a 14-module, dry-cooled, 75% capacity factor plant the overall solar-to-electric efficiencies are 15.8% annually and 17.8% at design point.

To evaluate the benefits of the multitower approach with single storage and power block a study by *Crespo et al. (2018)* considers a surrounded field reference plant of 100 MW with 8 hours of storage at 38° northern latitude. This latitude can be representative for plants in the USA, Spain, and China. Heliostats of 120 m² surface and 2,9 mrad total image error are chosen to perform the study. The performance of this reference plant is compared with 2x50 MW and 3x33 MW north field plants providing the same yearly net electrical production of 450 GWh in a site with a DNI of 2660 kWh/m²/y (Figure 16). As the efficiency of large plants is very much depending on the cleanliness of the atmosphere two different cases, relatively clear and hazy sites, are considered to analyse the impact of the atmospheric attenuation. Besides, latitude also plays an important role for solar tower plants, therefore the same study for a site at 30° latitude is carried out as well.

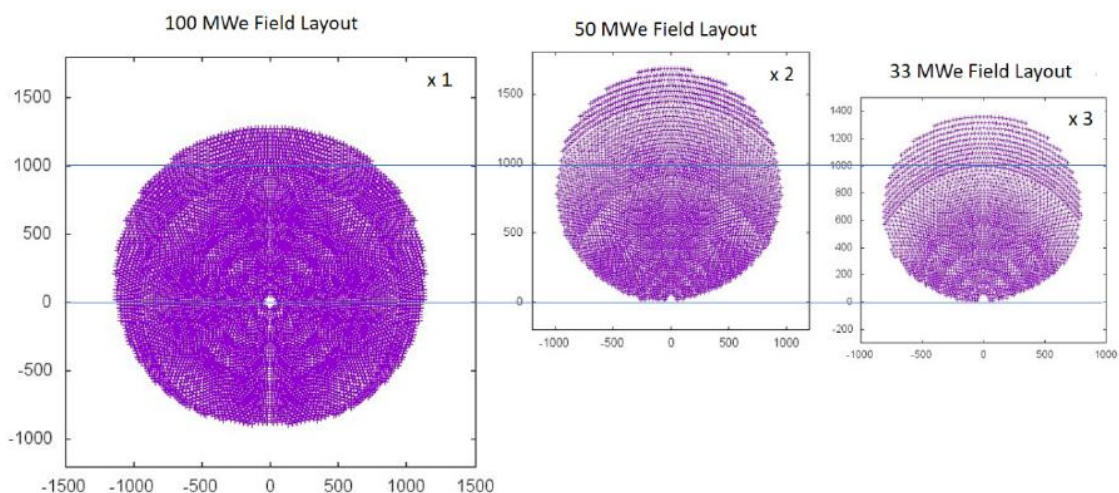


Figure 16 Considered heliostat field layouts for a 100 MW_{el}, 8 hours storage plant

This study reports that the efficiency of a northern field shows a significant decrease with the size of the plant. The field efficiency of a 100 MW plant with surrounded field and 8 hours of storage, in the same location with clear atmosphere, results 16 % higher than the efficiency of a northern field plant with the same power output, storage size and yearly production. The analysis conducted suggests that the breakeven point

between these two different field layout concepts is around 75 MW for plants with medium storage size. Therefore, for plants, smaller than 75 MW a northern field would be more efficient than a surrounded one. Considering this important fact, it would be better, in terms of plant efficiency and correspondently of minimum required number of heliostats, to build a plant with two or three independent northern heliostat fields with their corresponding towers and receivers.

The study also analyses the economic implications of building modular solar fields. Regarding the cost of the receiver, it is stated that the total surface of the panels would be very similar in all cases and similar number of vertical panels would be needed in any of the plants considered. Therefore, the main cost of this subsystem would not be significantly increased when building two or three receivers as the number of panels wouldn't be too much different. The height of the tower is slightly smaller in the northern field plants and the specifications regarding receiver weight would make them cheaper. Nevertheless, it would be more expensive to build two towers than one. Pumps, pipes and control and auxiliary systems would be certainly cheaper in the case of a single tower than in the case of split fields.

The results for relatively clear sites show that the plant using 2x50 MW northern field modules requires 10.36% less heliostats than a 100 MW surrounded plant. In the case of 3x33 MW the reduction in the heliostat field amounts to 11.01%. The largest effect happens when changing from the surrounded to the northern approach while there is not much gain when reducing from 50 to 33 MW. The height of the tower is significantly smaller when the size of the field is reduced. The most important difference in yearly performance is due to the cosine factor, which is much worse in the surrounded field. This effect is only partially compensated by a better shading and blocking as the heliostats in the southern part are much closer with almost no shading and blocking since they work almost horizontally for most of the time. As more heliostats can be placed closer to the receiver in the surrounded field the atmospheric attenuation efficiency is similar to the north modular fields even if the size is significantly different.

This study also indicates that another interesting advantage of the splitting could be achieving a more even distribution of the generated power between summer and winter seasons as well as some better availability factor in case of maintenance and repairs of the receiver or molten salt circuit. A very general and approximate economic analysis is also performed. The total cost of a 100 MW plant with 450 GWh/year generation is estimated around \$ 500 million. The heliostat field represents around 40 % of the total cost while the set tower/receiver represents around 15 %. Building two towers and two receivers increases this share to 17%. The 2x50 MW approach provides a rough estimation of around \$ 20 million savings in the heliostat field while the increase of cost of the tower/receiver subsystems is around \$ 10 million. In a nutshell, savings of around 2% in the CAPEX of the plants are estimated with the modular approach.

The results of the comparison between 30° North and 38° North, both with clear atmosphere, show that the 2x50 MW northern field plants at 30° North requires less heliostats than the 100 MW plant. This reduction was 9,95% at 30° North, which is slightly lower than the 10.36% at 38°. Nevertheless, as low latitude sites use to have a more even solar direct radiation this effect could be counterbalanced. It is also stated that the optimum design will require a slightly larger receiver in both cases at 30°, surround and northern fields, as compared with 38°. Slightly larger receivers will provide a better interception factor. On the other hand, this effect is partly attenuated by a certain increase in receiver losses.

The field/tower/receiver subsystems design in hazy atmosphere sites requires higher towers to put heliostats closer and avoid the losses caused by long distances between the heliostats and the receiver. In these cases, the shading and blocking efficiency are sacrificed with the aim of placing the heliostats as close as possible to the tower. In hazy locations, atmospheric attenuation plays a key role, and it makes the split and field type change more valuable. Although the cosine factor is practically equal for 50 MW and 33 MW northern field plants, the atmospheric attenuation is improved by more than 5 % when passing from 50 MW to 33 MW. Therefore, 33 MW appears to be a good compromise between technical improvements and cost increase. In terms of costs a rough estimation shows that the split in three plants provides a reduction of about \$ 37 million and net saving of over \$ 20 million, which correspond to around 4% on CAPEX reduction for a 100 MW plant.

A subsequent study by *Crespo et al. (2020)* furtherly investigates these concepts for a 150 MW plant concluding that multi-tower plants increase the efficiency and reduce the capital expenditure in the heliostat field as compared to plants with single heliostat fields. On the other hand, several towers, although smaller, cost more than one. Multi-towers also require lengthy molten salt pipes, in the 1 km range, with trace heating as well as a greater number of salt pumps. This study estimates that the cost of a 150 MW plant can be reduced close to 10% by choosing the multi-tower approach. This cost reduction figure can easily go to close to 15% if the plant internal consumption is fed by a PV installation next to the plant. Furthermore, it is underlined that the multitower approach is the proper way for solar tower plants to profit from all the efficiency and cost advantages of using single power blocks of the conventional power sector in the 250 – 500 MW range. Supercritical steam turbines, which are not commercial for the 100 MW range, can then be used straightforward in the solar sector providing significant improvement in the cost and efficiency figures.

Another study, by *Puppe et al. (2018)*, investigates a hypothetical 125 MW_{el} molten salt tower plant located in Postmasburg, South Africa with a solar multiple of 2.4 and 12 hours of storage capacity as reference case. This results in a power plant with approximately 700 MW_{th} power at design conditions. The receiver and HTF-system are designed for a single 700 MW_{th} receiver as well as a multi-tower system with five 140 MW_{th} receivers (Figure 17). A 121m² heliostat is chosen for all the solar fields. The

power block remains the same for all variants with 565 °C salt temperature. It includes dry-cooling and achieves a gross efficiency of 43.1% with steam parameters of 125 bar / 550°C. For the annual calculations a solar-only operational strategy of the plant is deployed, operating at full load during sunshine hours and while sufficient heat can be discharged from the storage tanks.

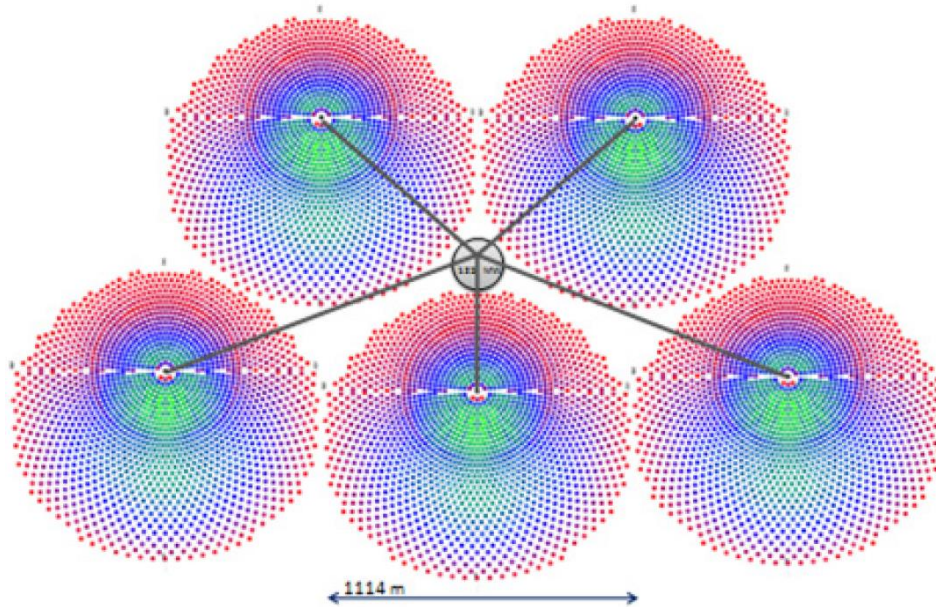


Figure 17 Plant layout of the multi tower system

Five smaller solar fields instead of one big solar field, feeding the same storage system and power block are investigated, together with alternative receiver designs and HTF temperature. The evaluation of the concepts is conducted primarily by annual yields, annual efficiencies and levelized cost of electricity (LCOE). In all cases the multi tower systems leads to distinctly higher LCOE than their single tower counterparts despite achieving a higher efficiency. The main reason behind this is seen in the investment cost breakdown, which shows much higher cost for the receiver and the HTF-system. Main contributors to the cost increase of the HTF-system are the connecting pipes of the 5 heliostat fields to the central power block and storage systems. The total length of connecting pipes is estimated to ~ 11.5 km with varying diameters. The pipes are built on elevated structures, to enable an incline so that the pipes can be drained into the storage tanks by gravity. This adds significant extra cost for the support structures. However, even with the additional cost of the HTF-system set to zero, the multi tower LCOE are still higher than the single tower variants due to the receiver cost increase. Another case study is conducted with higher atmospheric attenuation, which gives an advantage to multiple smaller heliostat fields. For each variant heliostat fields are designed with increased attenuation, which means a higher total amount of heliostat is necessary. Also in this case, the single tower variants achieve lower LCOE, even though only by ~5 % points.

Modular plant designs are particularly suitable for the combination of different technologies that can lead to flexible, reliable, and more cost-effective systems. In *García Barberena et al. (2013)* the use of a decoupled Brayton and Rankine combined cycle is investigated. In this study a multi-tower system using several small regenerative Brayton cycles feeds a single medium-temperature oil thermal storage system that, in turn, is used to drive a mid-temperature superheated Rankine cycle.

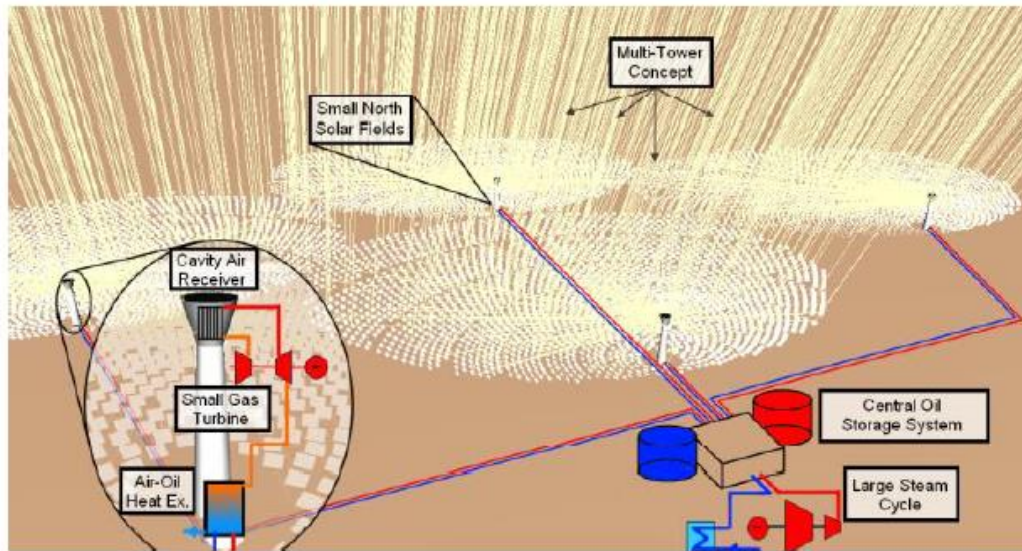


Figure 18 Scheme of the proposed plant concept

This concept takes advantage of the very competitive costs of medium size gas turbines alongside the specific cost reduction of steam turbines with size. Besides, the decoupled solar combined cycle (DSCC) operates in a decoupled way, so that the Rankine cycle is running at full nominal power or not running at all, thus substantially increasing its operating efficiency. In this plant a medium-to-high temperature air receiver is placed on top of the towers operating at about 800 °C and used for running a regenerative gas turbine in combination with a low temperature oil-based storage system, with smaller complexity and investment costs, operating at about 300 °C and used to run a slightly superheated steam turbine (280 °C, 40bar) as bottoming cycle.

A complete optimization of the proposed DSCC concept would need a multivariable optimization comprising a huge number of parameters. For this reason, many parameters that could have been optimized in a much deeper analysis, like the solar field configuration, the operating temperatures, the Brayton and Rankine cycle's sizes, are kept constant in this study. The optimization variables of the analysis are the number of solar towers for a single Rankine cycle, the storage capacity, and the solar multiple. For this preliminary optimization, a deterministic approach using the base cost and efficiency figures is used. The interesting results from this preliminary optimization show that, near the optimum, both the number of towers and the storage capacity can be selected over quite a large range with small influence in the energy cost, while the LCOE is strongly coupled to the solar multiple. Specifically, the

optimization shows an optimum value for the solar multiple of 2.10, while the number of towers can be between 30 and 40 and the storage capacity between 8 and 14 hours with small (<5 %) repercussion in the LCOE.

The final configuration selected in this study consists in 32 Brayton cycles giving a solar multiple of 2.1, feeding a storage system with a capacity of 9 Rankine cycle full load equivalent hours. With this configuration a deterministic LCOE of 11.27 c€/kWh is obtained. Also, a more detailed analysis of the LCOE taking into account probabilistic distributions for the most uncertain and relevant costs and efficiencies is performed. For each variable, the base value, as well as a minimum and a maximum value, are used to define the most likely value, the minimum value, and the maximum value of triangular probability distributions for each variable. The stochastic approach is applied to the components with the most uncertain costs and efficiencies and with strong influence in the results, i.e., the cost of the heliostats and the efficiency of the solar field, the cost and efficiency of the receiver, the thermal storage media cost. The results of the stochastic analysis performed within this work show a 90 % probability of achieving LCOE values between 10.42 c€/kWh and 11.36 c€/kWh with a mean value of 10.9 c€/kWh, according to the probability distributions assigned to the most uncertain figures.

The concept of decoupled solar combined cycles with modular solar fields is furtherly investigated by *Sorbet et al. (2018)*. Open volumetric air receiver solutions are analysed to fuel the Brayton cycle with high temperature solar power. Multi-tower schemes aiming at solar field downsizing are considered, to achieve better efficiency and modularity in the solar field and receiver subsystems, while keeping a larger size and thus more efficient Rankine cycle. This paper analyses the DSCC plant concept from a techno-economic, LCOE-based, optimization and financial evaluation.

In this work three plant schemes are considered, representing increasing levels of complexity and performance. The general DSCC scheme consists of a multi solar tower field working with atmospheric air as receiver heat transfer fluid. The heated air is used to feed a gas turbine obtaining electricity. An atmospheric air/pressurized air heat exchanger is used to transfer the heat from the receiver HTF stream to the Brayton cycle air stream. The rejected heat from the gas turbine is then used to transfer heat to the storage medium. In the first and simplest scheme (Figure 19), the exhaust gasses from several gas turbines are used to feed, through air/salts heat exchangers, a single two-tank molten salts storage system. Then the Rankine cycle is operated from the TES at rated capacity. This scheme is studied for two possible storage media alternatives: ternary nitrate salts (150°C to 500°C) and standard nitrate salt (290°C to 565°C).

with scheme 1 (12.85 ¢/kWh) with a difference of roughly ~0.4%. The optimized scheme 3 configuration results in a LCOE 2.5% higher than the lowest LCOE. It is noted that the minimum LCOE results from the plant configurations with relatively low global solar to electric efficiencies. In this sense, the third scheme presents the largest global efficiency (13.86%), based on smaller solar fields with larger efficiency than the rest of schemes and on increased heat recovery and hence thermal-to-electric conversion efficiency. However, this increased efficiency does not result in a more cost-effective solution. In the other schemes, the lower efficiency of the solar field and the additional heat losses in the air stream are partially compensated by larger and more efficient Rankine cycles.

The number of towers resulting from the optimization is also considered. Scheme 3 optimal configuration results in the maximum allowed number of towers (19), limited in this study for feasible spatial integration and reasonable pipe length and pressure drops in storage medium pumping. Also, the number of towers of the other schemes results in rather large numbers (14-15). Provided that scheme 1 is considered the best solution due to its reduced complexity yet achieving close to optimal LCOE values, a parametric analysis is carried out on scheme 1 to assess the sensitivity of the LCOE to the number of towers. For this study, the plant configuration is newly optimized each time the number of towers is changed. The optimization of scheme 1 configuration for different number of towers shows that the sensitivity of the LCOE to the number of towers is considerably low. Explicitly, the LCOE of the plant increases less than 0.3% if the number of towers is increased or decreased up by 27% (± 4 , from 11 to 19).

A different approach to modular tower system is proposed by *Rea et al. (2018)*. The design configuration that is considered is depicted in Figure 20 and is referred to as STEALS (Solar Thermal to Electricity via Advanced Latent heat Storage). A heliostat field reflects sunlight onto a solar receiver that is elevated by a steel truss tower. The entire thermal system is located on top of the tower. The receiver design is an optical cavity with an aperture that allows concentrated sunlight to be incident on the solar absorber (the bottom of the thermal energy storage tank). To transfer heat into and out of the TES, sodium heat pipes are attached to the top of the tank and extend down through the phase change material (PCM) to the solar absorber. These heat pipes spread into a flattened conical shape at the top and bottom of the tank to maximize surface area for efficient heat transfer with adjacent subsystems and are mechanically connected only at the top of the tank to minimize risk of failure due to stresses that occur during thermal cycling. An aluminum-silicon (Al-Si) eutectic alloy is used as a PCM because of its melting temperature, high energy density, high thermal conductivity, and low cost. To protect stainless steel construction materials from corrosion, all surfaces of the storage tank and heat pipes that are exposed to PCM are coated with a ceramic coating that is deposited by a plasma-spray method. The storage tank is insulated using a standard kaowool insulation material. The key to

dispatchability of this system is the ability to control when heat flows from the TES to the Stirling engine.

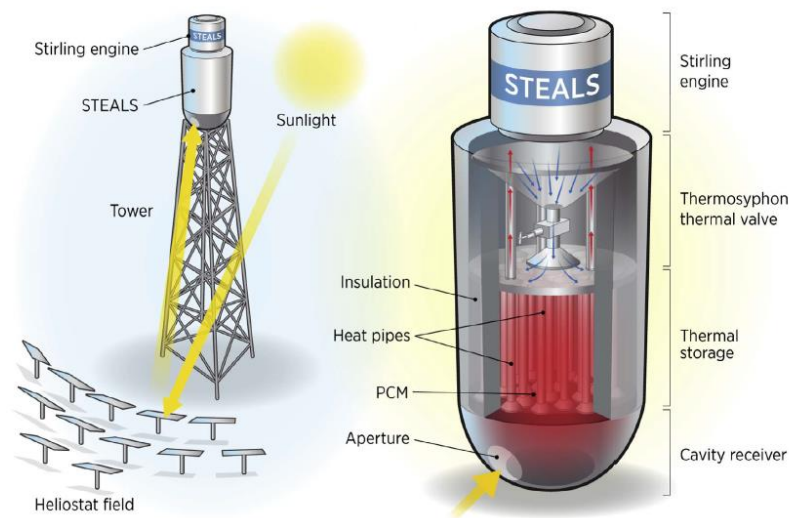


Figure 20 Solar thermal to electricity via advanced latent heat storage (STEALS) plant scheme

Alternatively to pumping a heat transfer fluid through the TES tank, this method of controlling heat flow uses a valved thermosyphon. In the “on” state, a working fluid (liquid sodium) evaporates at the thermosyphon evaporator (which is the same as the top surface of the TES tank). It then travels to the Stirling engine at the top of the thermosyphon because of the pressure difference created by evaporation. At the Stirling engine, the working fluid condenses, as it releases its latent heat, and returns to the evaporator by gravity through a liquid return pipe in the centre of the thermosyphon. In the “off” state, the liquid return is blocked by a shut-off valve, and once all working fluid has collected above this shut-off valve, the working fluid ceases to transfer heat. This thermal valve design is able to transfer high heat fluxes with very small temperature drops in the “on” state and is highly insulating in the “off” state. By tightly integrating system components in the same location on top of the tower, pathways for heat are very short which minimizes exergetic losses (both heat losses and temperature drops) from the solar receiver to the power block. Tower-based storage with passive heat transfer via heat pipes also eliminates the capital and operational costs of piping and pumps that are required in conventional solar power tower designs that locate their energy storage and power block on the ground. The penalty for suspending much of the system on top of the tower in this design is that structural tower cost increases because of the large mass that must be supported. In this analysis, this sets a limit on the relevant scale of this system to 1MW_{el} , based on existing towers built for wind turbines.

The cavity receiver in this design minimizes radiative and convective losses from the solar absorber, and the aperture can be closed to minimize storage losses when not receiving sunlight. Use of Al-Si as a storage material, with a melting temperature of $577\text{ }^{\circ}\text{C}$, allows the use of stainless steel as a structural material, leading to relatively

inexpensive construction. Higher temperature PCMs would give increased Stirling engine efficiency, but would also increase receiver and storage losses, and would potentially result in higher containment material cost. Stirling engines are attractive for this system because they can achieve relatively high efficiency at a small scale.

Results are based on a full system that has a nominal power rating of 200 kW_{el}, a 30% efficient Stirling engine, and 5 hours (3.3MWh) of thermal energy storage. The system operates with a ~30% capacity factor as a complement to PV. One potential market for STEALS is to provide load shifting to complement the growth of PV. Such dispatch control leads to a low capacity factor, which means that the power block is utilized much less than in a baseload plant. This results in higher LCOE, but also provides higher value electricity, because of the added benefit of dispatchability. Total annual energy efficiency of STEALS includes subsystem efficiencies of the heliostat field (71.2%), solar receiver (95.2%), thermal storage (98.6%), and thermal valve (99.6%). This results in an 18.3% annual solar to electric. The main limitation of STEALS is its low power block efficiency, but it is able to improve on heliostat field efficiency by employing a smaller field and improves upon receiver efficiency by using a cavity rather than external receiver. In addition, STEALS nearly eliminates parasitic power requirements for engine start-up, heat rejection, and pumped heat transfer fluids, which consume 8.3% of electricity generated by conventional CSP plants.

The LCOE analysis considers a range of power block efficiencies, power block costs, and system sizes. The impact of Stirling engine efficiency on the LCOE of STEALS is evaluated using efficiencies from 23–35% to provide a range from slightly below current Stirling engine performance to possible future performance with a minor improvement in technology. The lower LCOE data points for STEALS result from a power block cost (including heat rejection) of 1 \$/W, while the upper LCOE data points result from a power block cost of 1.77 \$/W. Over this range of power block efficiency and cost, the LCOE of STEALS is 8.1–12.8 ¢/kWh. The primary effect of improving power block efficiency is a reduction in the thermal power rating of the storage system and heliostat field. This leads to fewer heliostats, less PCM, and less mass held on top of the tower, all of which reduce cost. In this study it is also examined the impact of system size on the LCOE of STEALS. The optimum LCOE of 9.5 ¢/kWh is found at a size of 400 kW_{el}, though it is also observed the LCOE to be nearly independent of system size: there is just a 3% variation in LCOE over the full range of 100 kW_{el} to 1MW_{el}. This is due to the modular nature of the Stirling engine as a power block, and the scalability of the thermal storage system. This study suggests that STEALS has potential to be competitive with natural gas peaking plants and with conventional CSP technology at small scale.

Lindquist et al. (2019) furtherly investigate the concept of a modular tower system with integrated receiver, thermal storage, and power conversion unit. The modularity of these systems enables addressing all types of markets in sizes from around 500 kW up to 100 MW and above with maintained high efficiency, low cost, high-capacity factor,

minimal capital investment and short building times throughout the power output range. The system design consists of a heliostat field and a small tower with the thermal unit mounted on top. The heliostats, which are highly reflective double curved mirrors, reflect the sunlight onto a solar receiver fitted at the bottom of the PCM storage. Each mirror is around 2-3 m² and this small dimension enables high precision optics. The receiver design is a cavity with an aperture that enables the energy from the sunlight to be transferred directly from the solar absorber into the PCM through the thin wall of PCM storage tank. The PCM stainless steel storage tank is coated with a ceramic coating to protect it from corrosion by the Al-Si eutectic PCM alloy.

The stored thermal heat is transferred from the PCM to the Stirling engine by pumped liquid sodium heat transfer fluid, which is stored in a second tank surrounding the PCM tank. The circulation pump is of centrifugal type like those used in larger CSP tower plants, only much smaller. The Stirling engine is modified for optimal performance and power output at the temperatures provided by the selected PCM, which are lower than in the previous solar Stirling-dish application. The modifications include an enlarged expansion cylinder volume and a new tubular Sodium-Hydrogen heat exchanger. The entire power cycle unit is well insulated, and the cavity is equipped with a night-hatch to minimize thermal losses during times of limited or no insolation, such as during the night or bad weather.

The modular concentrated solar power plant is designed for high deployment rates with a rapid realisation of economies of volume in regions with high DNI in the range from 2000 to 2800 kWh/m²/year. However, if market conditions are favourable in terms of electricity prices available, then there would be no limitation to address markets with lower DNI than 2000 kWh/m²/year. Each unit has a rated power of 13 kW, and the targeted size of a park is between 0.1 and 20 MW. Depending on market and application, the mirror area of the solar field varies in size depending on solar conditions between 150 and 220 m². The thermal energy storage is designed to provide the engine with heat for around 13 hours and this configuration reaches a LCOE of 77 €/MWh.

Very few pilot plants have been built to explore the potential of the concept of modular solar tower plants. One of the first examples of demonstration modular CSP tower plant was the Aora Tulip plant located at Kibbutz Samar in the south of Israel and based on gas turbine technology. The plant became operational in 2009 and had a rated power of 100 kW_{el} and could also provide 170 kW as heat. The plant required a surface of 200 m² and comprised 50 heliostats that focused the sun rays into the "bulb" of the tulip made of solar receivers, where pressurized air was heated to nearly 1,000 degrees Celsius. A second plant was built in 2012 in Almeria, Spain. The hybrid operation of the system enabled to continue producing energy even when sunlight was insufficient. More specifically, the system could run on natural gas, diesel, biogas, bio diesel and LPG to ensure that energy supply was uninterrupted in any weather condition. The concept of Aora tulip modular plant did not furtherly expand after the two first

demonstrative plant as more modern concept with thermal energy storage emerged as the leading trend in concentrated solar power [18] [19].

Another pilot plant involving modular CSP tower technology was the Lake Cargelligo solar thermal project. It was built in 2009 and it consisted of graphite solar storage receivers (SSR) mounted on 24m towers, with dedicated dual axis tracking reflective heliostat fields of approximately 760 m² (Figure 21). SSR comprised a body of graphite housed in a cavity with an aperture that permitted solar energy to be directed through the aperture onto a receiver in contact with the graphite, and a heat exchanger partly embedded within the graphite capable of accepting a heat transfer fluid, in this case water. Each of the SSR's was effectively an on-demand steam generator, which was connected by a steam manifold that delivered the steam to a 3MW_{el} steam turbine generator. Steam was produced at temperatures between 200°C -500°C and various pressures up to 50 bar and had storage capacity to generate 3MW_{el} for 1 hour. The plant was dismantled in 2016 after more than 25,000 hours of operation [20].



Figure 21 Lake Cargelligo power plant

In 2009 eSolar began the construction of a modular solar tower power facility known as Sierra SunTower. This plant started its operation in 2010 and included two modules, for a total of 24,360 heliostats of 1.1-m², divided between four sub-fields, that focused solar radiation onto two tower-mounted receivers (Figure 22). The focused heat converted feedwater piped to the receivers into superheated steam that drove a reconditioned 1947 General Electric turbine generator of 5 MW. Direct steam systems are effective for generating power when the sun is shining but make difficult and expensive to incorporate storage. The plant remained operational until 2014.



Figure 22 Sierra SunTower Facility

One innovative concept for modular plants is the beam down approach applied at Yumen Xinneng 50 MW molten salt tower power plant in China. It is the only pilot project using innovative beam down CSP tower technology and it is also the first large-scale commercial CSP project in the world of this kind. The project is made of 15 modules, each one of 17MW_{th} and one beam-down tower. A single 9-hour molten salt thermal storage system and a 50MW_{el} steam turbine set are also equipped in the project. The first module has been fully completed and commissioned in 2021, while the second module is under construction, with the secondary reflection tower being lifted, and the majority of heliostats installed. The modules from 3 to 10 are undergoing basic civil engineering and steel structure and heliostats installation (Figure 23) [21].



Figure 23 Module 1 of Yumen Xinneng power plant

The last existing solar tower modular plant is Vast Solar Jemalong power facility in Australia. This plant comprises 5 modules using liquid sodium as heat transfer fluid and storage media for a 3h storage capacity and a 1.1 MW steam turbine. The details of this project are furtherly discussed in Section 3.2, Jemalong pilot plant.

2 Modelling

2.1. Overview

In order to investigate modular solar tower systems different tools are employed and developed to model the different subsystems of the plant, as outlined in Figure 24. The first subsystem considered is the solar field. The heliostat geometrical characteristics and optical performances are modelled using the National Renewable Energy Laboratory (NREL) Solar Power Tower Integrated Layout and Optimization Tool (SolarPILOT). This tool allows to design the solar field accounting for solar conditions and field constraints (i.e., land shape, heliostat position, tower height) and to estimate the optical performances for any given sun position throughout the year. The outputs provided by SolarPilot, namely optical efficiency and heat flux map (HFM) of the receiver, are used as inputs for the receiver model coded in Matlab® [22]. Two different receiver models are employed: one billboard receiver model for the solar fields with polar layout, and one external cylindrical receiver model for the solar fields with surrounded layout. The billboard receiver model is modified and improved along with the development of this study and the model robustness to changes in the discretization is analysed.

The results provided by the receiver model (i.e., heat transfer mass flow rate, pressure drop in the receiver) are used as input data for the piping model coded in Matlab®. This code is entirely developed as part of this work and allows detailed analysis of the piping subsystem (i.e., heat losses, pressure losses, costs) while also granting the possibility of a fully flexible field layout design. The obtained results are used for the modelling of the thermal energy storage subsystem and subsequently for the power block. For these two subsystems straightforward models coded in Matlab® are used. All the subsystem models combined allow both the design of the whole considered plants and the annual evaluation of the performances based on an hourly time scale.

For each component of the system many different cost correlations and values are collected and the ones considered most suitable are selected for the estimation of economic parameters (i.e., investment cost, levelized cost of heat, levelized cost of electricity). Due to the difficulty to retrieve reliable and coherent cost correlations for some components the obtained cost results can be subjected to significant uncertainty. Although they can provide a reference for comparison with the power production market prices their scope is primarily the optimization of different plant configurations based on a both technical and economic evaluation. The whole plant

modelling is intended as a tool to reach the aim of the work: the assessment of the possible advantages and issues of the modular approach, in order to identify the best design options to orient future research and decision making when designing CSP plants.

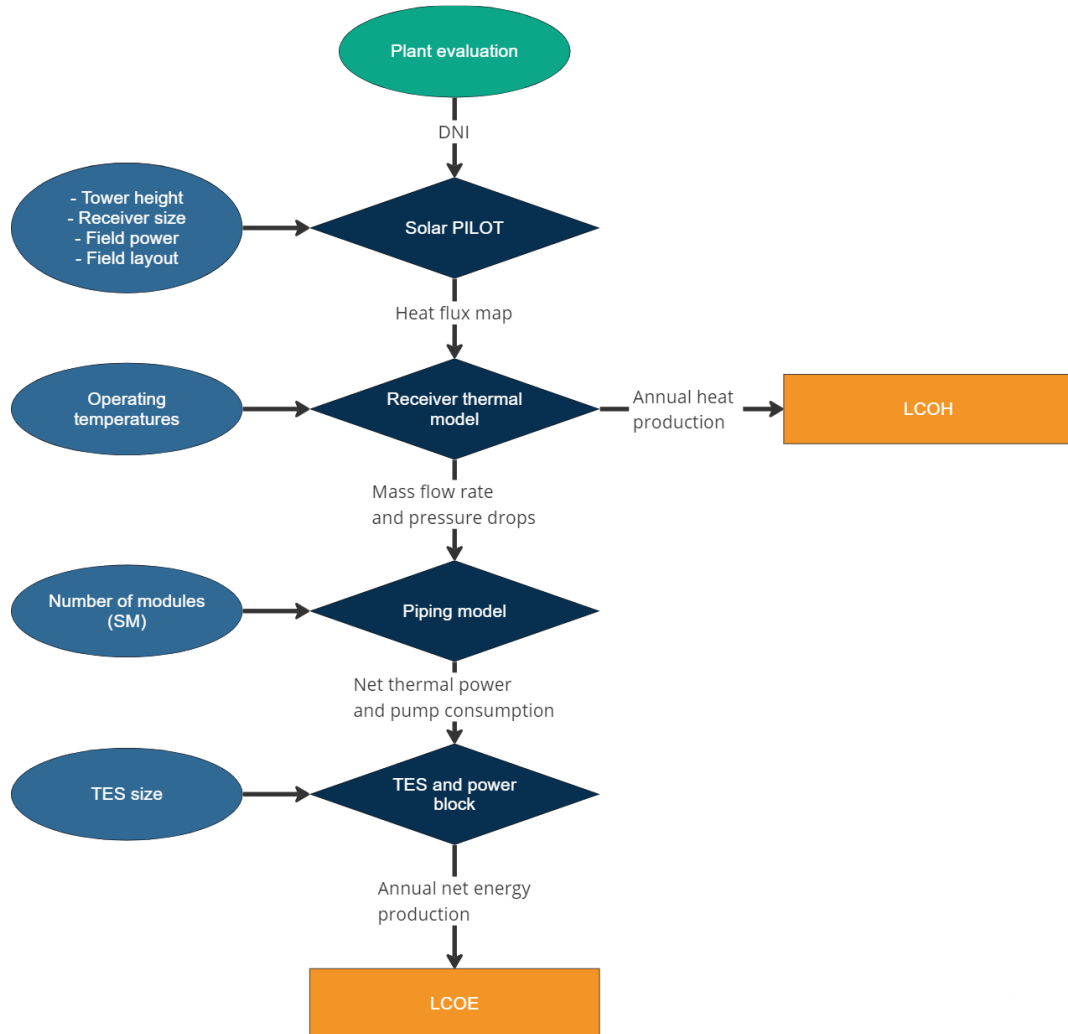


Figure 24 Methodology flow chart

2.2. Solar field

The first step for the system design and performance assessment is the study of the optical efficiency of the concentrating system. For this purpose, the software SolarPILOT is employed. This tool uses a modified Gaussian series expansion to characterize the image generated by each heliostat. Rather than construct the model of the image using a large number of rays that eventually approach a Gaussian-form image via probabilistic modelling, the error distributions are included in the analytical formulation to begin with, allowing an explicit model that solves much more quickly than a probabilistic one [23]. SolarPILOT is also a comprehensive power tower optical-modelling tool that includes the ability to generate field layouts in a variety of patterns

or land constraints, conduct detailed optical performance simulations and conduct parametric analyses.

SolarPILOT presents six different input categories: climate, markets, costs, layout setup, heliostat, and receiver. In this work the markets and costs inputs are not used as economic evaluations are performed independently and outside of SolarPILOT framework. In the climate section plant location, weather and atmospheric conditions, and properties of the sun's flux distribution can be defined. For this work the selected location is Canberra (see Chapter 3, Case Study) which coordinates are 35.30° S and 149.18° E and which is located at an altitude of 577 meters above sea level (m.a.s.l.). The sun shape model selected is the limb-darkened sun model. In this case sun intensity $\phi(\theta)$ is specified as a function of angular distance from the centroid of the sun disc θ , as shown in Equation (1).

$$\phi(\theta) = 1 - 0.5138 \cdot \left(\frac{\theta}{0.00465} \right)^4 \quad (1)$$

The intensity of DNI and other weather values are included in the hourly weather data provided by SolarPILOT for the selected location. The atmospheric attenuation model selected is the DELSOL3 Clear Day. In the selected model the fraction of energy that remains after atmospheric scattering η_{att} is related to slant range r by a single-dimensional polynomial equation, as described by Equation (2).

$$\eta_{att} = 0.002845 \cdot r^3 - 0.017 \cdot r^2 + 0.1046 \cdot r + 0.006789 \quad (2)$$

In the layout section the desired power delivered by the receiver at the reference design point can be selected. The total power delivered by the receiver is equal to the power provided by the solar field minus the heat loss from the receiver and heat loss from tower runner piping. In this work the receiver and tower losses are set to zero as they are accounted for in the models used outside of SolarPILOT framework. Therefore, the desired power delivered by the receiver actually corresponds to the power delivered by the solar field. The design-point DNI value, which represents the solar resource available at the reference design point, and the sun position for the reference design point are considered in order to meet the solar field design power. These values are set to 1000 W/m² for the DNI and to winter solstice for the sun position (see Chapter 3, Case Study).

SolarPILOT provides several options for specifying the region of land where heliostats may be placed. Options include scaled bounds where the land area is a function of tower height, fixed bounds which specifies a minimum and maximum fixed radius centered about the tower where heliostats may be placed, and an option for specifying polygonal shapes that may represent included or excluded land areas. Multiple land boundary methods may be used simultaneously, as in the case of this work. Two different layout methods can be selected: the radial stagger and the cornfield. In the

radial stagger method, heliostat rows are placed alternately along iso-azimuthal lines at constant radii as shown in Figure 25.

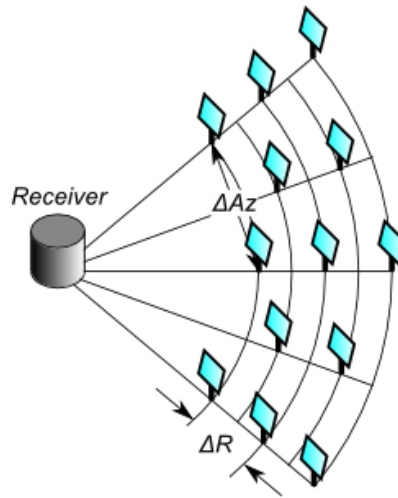


Figure 25 Radial stagger layout method

The "cornfield" layout is also known as a "straight row", "rectangular" or "Cartesian" layout as heliostats are aligned in straight rows, typically along principal Cartesian axes. SolarPILOT includes this layout option and allows specification of spacing in both the principal East-West (X) and North-South (Y) axes. Figure 26 illustrates the cornfield layout concept.

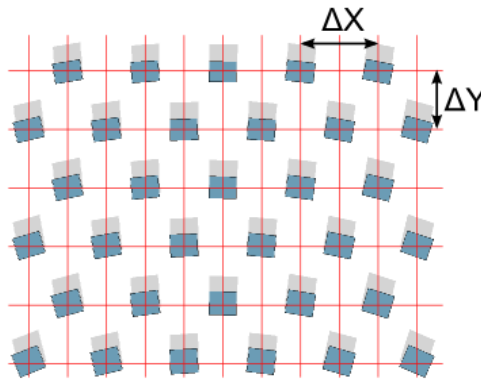


Figure 26 Cornfield layout method

The heliostat geometry and properties can be defined in the heliostat template section. Heliostat geometry includes macroscopic dimensions and parameters to specify heliostat facets. In this work heliostats are considered as only one panel with no facets while the focusing type was considered of "at slant" type which means that the heliostat focal length is equal to the distance between the heliostat pivot point and the receiver centroid. The elevation pointing error and the azimuth pointing error due to heliostat drives are set to zero. Surface slope error in the X and Y directions (σ_{sx} and σ_{sy}), which represent the standard deviation of angular displacement (waviness) of the heliostat surface assuming a normal distribution, are set to 0.00153 rad. The reflected beam error in the X and Y direction (σ_{rx} and σ_{ry}), which represent the standard

deviation of the specular reflection from the surface (specularity) assuming a normal distribution, are set to 0.002 rad. The total error σ_{total} indicating the effective standard deviation of the reflected image from the heliostat including all sources of error is then computed by SolarPILOT.

The remaining mirror parameters are summarized in Table 2. The reflective surface ration is the ratio of active reflective area to total structural area, mirror reflectivity represents base surface reflectivity of the mirror in a pristine or clean state, while the soiling factor represents the fraction of light that is reflected after accounting for surface soiling. These values are kept equal to the standard values provided by SolarPILOT [23].

Property	Value
Reflective surface ratio	0.97
Mirror reflectivity	0.95
Soiling factor	0.95

Table 2 Mirror performance parameters [23]

The receiver geometry and the optical and thermal properties can be defined in the receiver section. In this work only the geometry of the receiver is defined, as optical and thermal properties of the receiver are modelled outside of SolarPILOT. For this reason, the receiver thermal absorptance is set to 1 and all the receiver thermal losses are set to zero. Receiver dimensions can be specified altogether with the receiver type. In the case of flat plate receiver, which corresponds to a billboard receiver, the heat absorbing surface lies within a flat plane with a surface normal vector pointing toward the horizon. The shape of the angular window is selected as rectangular in accordance with the thermal model of the receiver. The receiver orientation elevation is set to -30° , which means the receiver is oriented downwards towards the solar field. The receiver horizontal acceptance angle is restricted to 150° instead of 180° , which is the angular extent in the horizontal direction from the perspective of the receiver from which incident light can be accepted. The angular span is symmetric about the normal vector from the surface of the receiver.

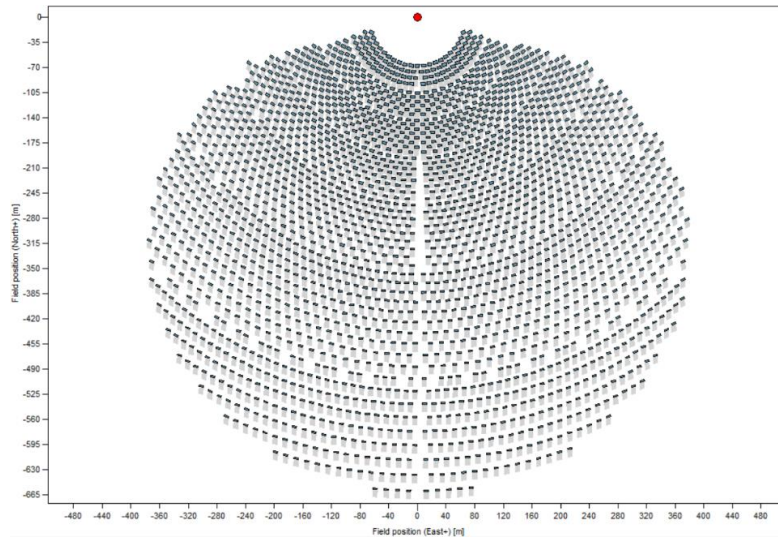


Figure 27 Example of field layout obtained with SolarPILOT

Once the field layout has been defined a simulation can be performed to evaluate the performances of the field for a given sun position. The performance simulation consists of evaluating the current heliostat field layout and receiver geometry for optical and thermal performances. SolarPILOT calculates the optical performance of each heliostat to determine the overall field performance. In this work the selected design point is summer solstice in the austral hemisphere, which corresponds to the 21 of December at noon with a DNI of 1000 W/m^2 . This simulation is used in all the considered configurations to check the correct design of the field and, in particular, to check that the power delivered to the receiver meets the desired value.

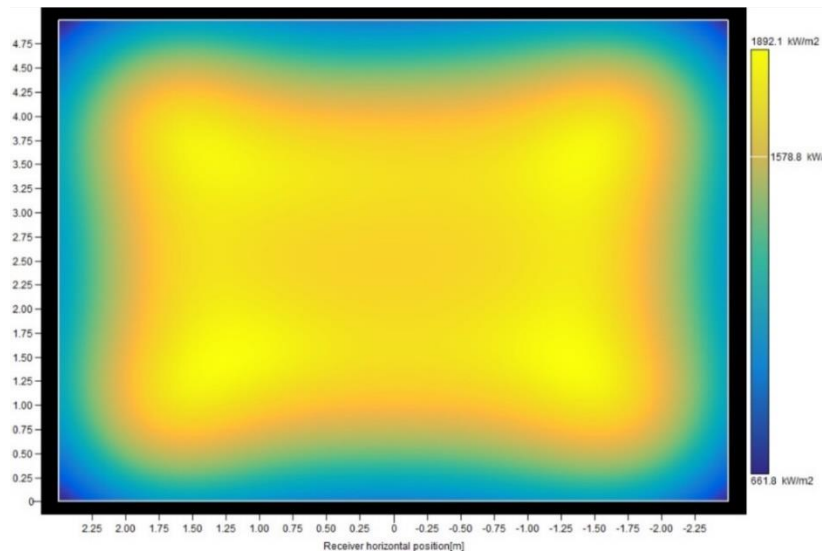


Figure 28 Example of a receiver heat flux map obtained from SolarPILOT

The parametrics section provides options for constructing and executing batch runs of SolarPILOT. Parametric runs allow to lay out and/or characterize a field over a range of parameter values. Parametric runs are used to evaluate the field performances at different sun positions with the aim of mapping the optical efficiency of the field for

any moment of the year. The obtained results are used in the annual performance analysis of the plant as discussed in Section 2.6, Annual simulation.

For any performance simulation SolarPILOT provides a set of results as shown in Figure 29. These include the total heliostat area, the heliostat number, the power incident on the field and the power delivered to the receiver.

	Units	Value	Mean	Minimum	Maximum	Std. dev
Total plant cost	\$	31670607				
Simulated heliostat area	m ²	80072				
Simulated heliostat count	-	2293				
Power incident on field	kW	80072				
Power absorbed by the receiver	kW	20809				
Power absorbed by HTF	kW	20809				
Cloudiness efficiency	%	100.00	100.00	100.00	100.00	0.0000
Shading efficiency	%	82.17	82.17	5.18	100.00	19.4155
Cosine efficiency	%	58.61	61.01	23.67	95.66	19.9747
Reflection efficiency	%	90.25	90.25	90.25	90.25	0.0000
Blocking efficiency	%	97.21	97.62	55.02	100.00	4.5441
Attenuation efficiency	%	95.81	95.91	93.03	98.17	1.3357
Image intercept efficiency	%	64.21	63.90	28.83	82.52	9.2023
Absorption efficiency	%	100.00				
Solar field optical efficiency	%	25.99		3.18	63.97	9.2331
Optical efficiency incl. receiver	%	25.99		3.18	63.97	9.2331
Annualized heliostat efficiency	%	0.00		31.38	77.87	13.7029
Incident flux	kW/m ²	832.37		278.19	1106.81	184.2618

Figure 29 Example of results obtained from SolarPILOT

Shading efficiency η_{shadow} represents the proportion of power lost due to heliostats casting shadows on neighbours, thereby preventing irradiance from reaching a portion of the affected heliostats. Blocking efficiency η_{block} accounts for power loss due to light that is reflected from heliostats onto the back of adjacent heliostats. Cosine efficiency η_{cosine} is calculated by taking the ratio of power incident on the aperture area of the heliostat field divided by the available power after cloudiness and shadowing losses. Cosine loss is evaluated for each heliostat by taking the dot product of the heliostat normal vector and the sun vector. Reflection efficiency η_{refl} captures power loss after cloudiness, shadowing, and cosine efficiency, and includes both mirror soiling and reflectivity efficiency. Attenuation efficiency η_{att} accounts for power loss during transmission of reflected light from the heliostats in the field to the receiver. Image intercept efficiency η_{int} accounts for light that is transmitted from the heliostat field to the position of the receiver but fails to intercept or impinge on the receiver aperture. This loss is also referred to as "spillage." Light that strikes non-absorbing surfaces such as oven boxes, refractory walls, or the tower structure, or light that misses the receiver system entirely is accounted for in this efficiency value. The solar field optical efficiency η_{opt} is equal to the product of all efficiency values, as showed in Equation (3).

$$\eta_{opt} = \eta_{shadow} \cdot \eta_{block} \cdot \eta_{cosine} \cdot \eta_{refl} \cdot \eta_{att} \cdot \eta_{int}$$

(3)

The incident flux indicates the intensity of reflected irradiation that is incident on the receiver after all losses. The number reported in the value column indicates the mean flux intensity across the receiver aperture. The maximum flux value provided by SolarPILOT is used to verify the compliance with the maximum flux threshold due to material limitations in the receiver.

2.3. Receiver

The billboard and cylindrical receiver thermal models are based on the same Matlab® code. This model allows to simulate the steady state behaviour of the receiver accounting for receiver characteristics, HTF type, heat flux distribution, ambient conditions, and for reflective, radiative, and convective thermal losses. Receiver tubes are discretized in control volumes along the circumferential and axial direction. Thermal losses through conduction in the insulated back-side account for a very small percentage of the total heat loss from the tubes and are therefore assumed negligible by treating the rear side of the receiver as adiabatic. The system is solved fixing the inlet and outlet temperatures of the HTF and computing the mass flow rate iteratively, starting from a first guess value computed assuming a thermal efficiency of the receiver of 80%, and proceeding until convergence is obtained on the mass flow rate.

In the first phase of this work the billboard model adopted is a single-pass receiver type. This model is significantly slower with respect to the multi-pass cylindrical receiver model, and it also does not consider heat conduction between adjacent control volumes in the circumferential direction. For these reasons the billboard receiver model is modified to include the multi-pass option and the circumferential heat conduction. Only this last version of the billboard receiver model is discussed together with the cylindrical receiver model. For the billboard receiver a configuration with 2 flow paths with 2 panels aligned one on top of the other for each flow path, is used. For the cylindrical receiver 2 flow paths with 9 panels aligned horizontally along the circumference of the receiver is considered. These two models are almost identical, especially regarding the functions responsible of fluid properties calculation and thermal behaviour modelling, and they will be therefore referred to as only one model in this section.

The receiver model requires a significant number of parameters and input variables. The heat flux distribution on the receiver surface, provided by SolarPILOT, is one of the main inputs. Different HTFs are available, in particular many solar salts with different chemical compositions. In this work liquid sodium is selected as HTF as discussed in Chapter 3, Case Study. A specific function computes the necessary properties for the selected HTF at the given conditions, such as density, heat capacity, dynamic viscosity, thermal conductivity, Prandtl number, enthalpy. The Haynes230 alloy is selected as tube material. This alloy is a nickel-chromium-tungsten-molybdenum alloy that combines excellent high-temperature strength, resistance to

oxidizing environments up to 1149°C for prolonged exposures, resistance to nitriding environments, and long-term thermal stability. It is readily fabricated and formed, and it can be casted [24]. Optical properties of the tubes, insulating walls, and surrounding environment are specified as shown in Table 3 and they are kept fixed for all the simulation considered in this work [22].

Parameter	Value
Tube coating emissivity	0.87
Tube coating absorptivity	0.93
Insulating wall emissivity	0.75
Insulating wall reflectivity	0.30
Ground emissivity	0.955
Sky emissivity	0.895

Table 3 Optical parameters of the receiver model [22]

The main input parameters, that vary among the different configurations analysed, are shown in Table 4. The geometric characteristics of the receiver need to be specified. These include receiver height and width/diameter, the diameter of the tubes and their thickness, and the spacing between tubes. The used tube dimensions correspond to the ANSI (American National Standards Institute)/ASME (American Society for Mechanical Engineers) B36.10M pipe series [25]. Ambient temperature and wind speed at ground level are defined for the evaluation of air properties and radiative and convective thermal losses. The inlet temperature of the heat transfer fluid in the receiver, as well as the outlet temperature, are fundamental for the solution of the model and need to be specified. The discretization is expressed as the number of axial and circumferential control volumes considered: the proper selection of these parameters is critical for an appropriate use of the model as it will be discussed later in this section. The number assigned to the variable corresponding to the circumferential discretization represents the number of control volumes in a quarter of circumference.

Parameter	Values
Tubes diameter	2.38 - 60.3 mm
Tubes thickness	0.405 - 1.65 mm
Tubes spacing	1 mm
Receiver height	0.75 – 16 m

Receiver width/diameter	0.75 – 16 m
Inlet HTF temperature	550 °C
Outlet HTF temperature	730 °C
Ambient temperature	25 °C
Wind speed	10 m/s
Axial control volumes	1 - 5000
Circumferential control volumes (in a quarter of circumference)	1 - 5

Table 4 Input parameters of the receiver model

Once all the input parameters have been provided the model proceeds computing the number of tubes for each panel depending on tube and receiver dimensions, and headers and manifold dimension. When the geometry of the whole receiver has been defined the view factors and the radiative resistance matrix are computed in order to evaluate the radiative thermal losses. The radiative resistance matrix accounts for the mutual resistances involving the considered tube volume, neighbouring tubes, insulating wall and external environment. The equivalent electric circuit representing a system where two circumferential control volumes are considered for each quarter of circumference is shown in Figure 30. Another radiative resistance matrix accounting for radiative interaction between adjacent panels is also computed.

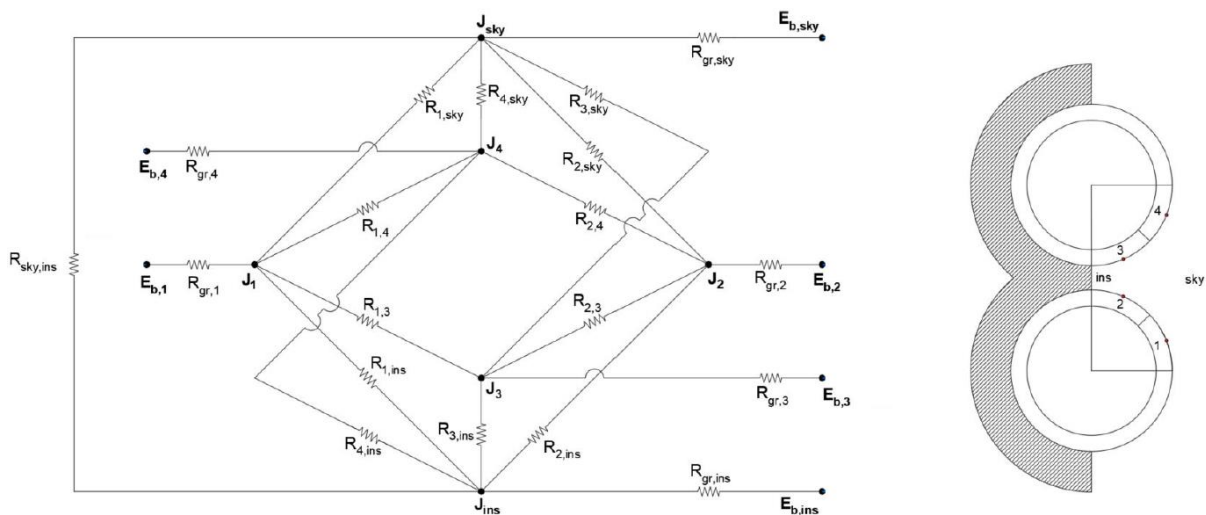


Figure 30 Thermal resistance network in the case of two circumferential control volume for each quarter of circumference [22]

Using all the computed resistances the model begins to solve iteratively the system starting from a first guess value until convergence is reached on the mass flow rate. First the heat flux map (HFM) data are interpolated to match the selected tube

discretization. The thermal power absorbed by the heat transfer fluid in each control volume $Q_{HTF,i}$ is given by Equation (4). It is the difference between the thermal power absorbed by the considered tube volume $Q_{abs,i}$ and the power losses due to radiative $Q_{rad,i}$ and convective heat transfer $Q_{conv,i}$.

$$Q_{HTF,i} = Q_{abs,i} - Q_{rad,i} - Q_{conv,i} \quad (4)$$

The power absorbed by each tube element $Q_{abs,i}$ is given by the sum of two contributes: the flux directly hitting the tube volume and the flux hitting the tube volume after being reflected by the portion of insulating wall between two adjacent tubes. It is null for all the control volumes in the back of the receiver. The computation of radiative $Q_{rad,i}$ and convective $Q_{conv,i}$ losses requires an additional iterative procedure starting from a guess value for the external surface temperature of the tube volume. The radiative thermal power exchange $Q_{rad,i}$ of the tube volumes in the front of the receiver with other tubes, insulating wall, and environment is computed applying the radiosity method. Heat exchange is null for the circumferential elements in the back side of the receiver. A linear system corresponding to the equivalent electric circuit is defined, where the coefficients are given by the radiative resistance matrix, and it is solved using the assumed external tube surface temperature. The obtained radiosities are used to compute the radiative heat fluxes.

Convective losses $Q_{conv,i}$ account for thermal power lost due to forced and natural convection in the front side of the tubes. The heat transfer coefficient that includes the mixed contributes of the two convection mechanisms is computed as function of the forced convection and natural convection heat transfer coefficients. Once both radiative and convective losses have been estimated the power absorbed by the heat transfer fluid $Q_{HTF,i}$ can be evaluated as previously shown in Equation (4). The thermal conductive resistance of the considered tube element is used to compute the internal surface temperature of the tube control volume, starting from the assumed tube external temperature as part of the same iterative procedure as before.

The model then proceeds to estimate the inlet and outlet temperatures of the heat transfer fluid and the internal surface temperature of the tube in each control volume, considering conduction between adjacent circumferential elements and considering the previous axial elements that the fluid has passed through. The external surface temperature is computed from the obtained results and compared with the temperature assumed initially to estimate radiative losses, convective losses, and the HTF temperature. This iterative procedure continues until convergence on the external surface temperature of the considered tube element is reached with a certain tolerance. Once this procedure has been completed for all the control volumes the total heat absorbed by the heat transfer fluid Q_{HTF} and the total losses are computed, and the mass flow rate is calculated. This value of mass flow rate is compared with the initially assumed value and the whole procedure is repeated until convergence with a certain

tolerance. The main results provided by the model are heat losses in the receiver, HTF mass flow rate, receiver thermal efficiency, computed as discussed, and pressure drops in the receiver.

Pressure losses are computed accounting for distributed and concentrated pressure losses. Concentrated pressure losses account for the presence of manifolds, headers, and tube curves and are function of receiver geometry, pipe dimensions, flow rate, HTF temperature. Distributed pressure losses $Dp_{distributed}$ are evaluated as function of Darcy-Weisbach friction factor.

With the results provided by the receiver model it is possible to optimize the receiver tube dimension. Pressure drops and thermal losses are evaluated for different tube diameters and the corresponding thicknesses from the ANSI/ASME B36.10M pipe series as showed in Table 5 [25].

Diameter [mm]	2.38	3.18	3.97	4.76	6.35	10.29	13.7	17.1	21.3	26.7	33.4	42.2	48.3	60.3
Thickness [mm]	0.405	0.815	0.895	0.915	1.222	1.24	1.65	1.65	1.65	1.65	1.65	1.65	1.65	1.65

Table 5 Tube diameters and corresponding thickness considered for the optimization

The optimization is the result of the trade of between power losses due to the pumping of the HTF and thermal power losses. The net thermal power Q_{net} is computed using Equation (5), as the difference between the total thermal power absorbed by the HTF, after heat losses have been considered, and the pump power consumption W_{pump} converted to thermal power using reference efficiencies for the pump $\eta_{pump,ref}$ and the power block $\eta_{PB,ref}$.

$$Q_{net} = Q_{HTF} - \frac{W_{pump}}{\eta_{pump,ref} \cdot \eta_{PB,ref}} = Q_{HTF} - Q_{pump} \quad (5)$$

At low diameters pressure drops are considerably high and significantly affect the system, while at higher diameters the heat losses prevail. In this work for each receiver size and heat flux map this optimization procedure has been performed to assess the optimal receiver tube diameter and the corresponding thickness.

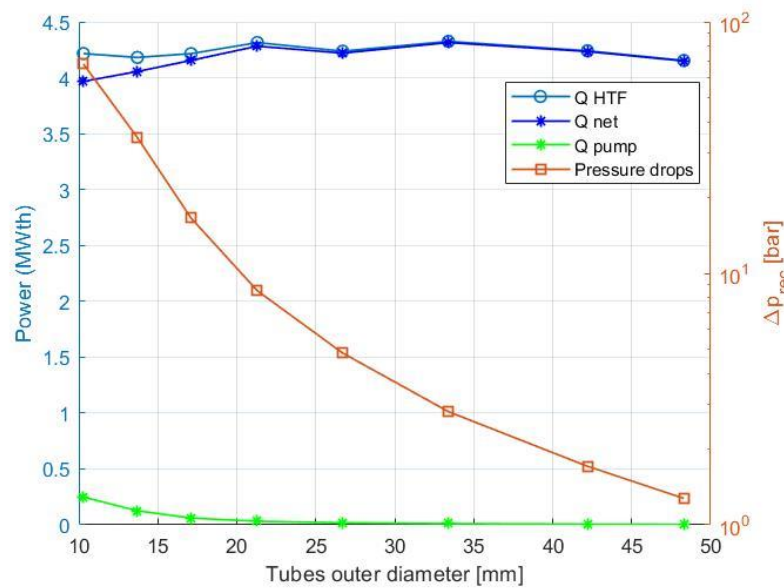


Figure 31 Example of receiver tube diameter optimization for a cylindrical receiver

As previously commented in this section a single pass model for the billboard receiver is used in the first part of the work for the receiver. This model is characterized by very long computational time, mainly for two reasons. The first reason is that conduction between adjacent circumferential volumes is not implemented, and this leads to a significant decrease in the predicted thermal performances of the receiver. To counterbalance this effect a really high discretization is required both in the axial and in the circumferential direction increasing the computational time. The second reason is due to the method used to solve the linear system corresponding to the equivalent electric circuit of the radiative losses. In the single pass receiver only one radiative resistance matrix describes the whole receiver as it is composed only by one panel. For this reason, the resulting matrix has a considerable size which is furtherly increased by the high-density discretization required, leading to a huge matrix and very long computational time. The first improvement implemented is a decomposition method for a faster resolution of the linear system associated to this matrix. This allows a significant reduction of the required computational time and allows an extensive analysis of the effect of receiver discretization on thermal efficiency for the single pass billboard receiver.

The selection of the number of axial (N_{ax}) and circumferential (N_s) control volume significantly affects results and time expense. The specified numbers refer to the absolute number of control volume considered, for example 4 axial elements correspond to 4 elements of 0.25 m length for a receiver of 1 m of height and to 4 elements of 2 m for a receiver of 8 m of height. Therefore, for each receiver dimension the number of control volumes must be correctly defined in order to ensure the correct discretization and the comparability of the results. The discretization analysis for a 4.5 m x 4.5 m receiver is reported in Figure 32. For each run the efficiency is compared to a reference “real” efficiency obtained with extremely high number of axial and

circumferential volumes and computational time. This is shown by the colour of the efficiency results: the red colour indicates that the result obtained with the used discretization is far from the “real” efficiency value. Increasing the number of control volumes the efficiency tends to the “real” value up to the point where furtherly increasing the discretization does not lead to an improvement in the model results. The colour map in the run time table gives a graphic evaluation of the faster and slower runs.

		4.65 m x 4.65 m								4.65 m x 4.65 m						
		Ns								Ns						
		13	15	17	19	21	23			Run time [s]	13	15	17	19	21	23
Nax	11	76.83%	78.45%	79.64%	80.54%	81.23%	81.79%	11	159	203	252	310	372	461		
	13	78.75%	80.06%	81.00%	81.71%	82.26%	82.69%	13	144	190	234	299	361	429		
	15	80.10%	81.17%	81.95%	82.53%	82.97%	83.32%	15	137	177	236	289	353	412		
	17	81.10%	82.00%	82.64%	83.13%	83.50%	83.79%	17	132	183	228	282	335	403		
	19	81.85%	82.62%	83.17%	83.58%	83.89%	84.14%	19	133	173	226	271	324	386		
	21	82.44%	83.10%	83.57%	83.93%	84.20%	84.41%	21	130	167	232	262	317	377		
	23	82.91%	83.49%	83.91%	84.21%	84.45%	84.63%	23	131	169	212	265	308	361		
	25	83.29%	83.81%	84.17%	84.44%	84.65%	84.81%	25	126	167	205	255	303	363		
	27	83.61%	84.07%	84.39%	84.64%	84.82%	84.96%	27	127	164	204	243	591	357		
	29	83.87%	84.29%	84.58%	84.80%	84.96%	85.09%	29	119	167	227	253	299	351		
	31	84.10%	84.48%	84.74%	84.94%	85.09%	85.20%	31	122	159	200	245	288	343		
	33	84.30%	84.64%	84.88%	85.06%	85.19%	85.30%	33	118	157	196	240	285	337		
	35	84.47%	84.78%	85.00%	85.16%	85.28%	85.38%	35	120	152	194	235	279	337		
	37	84.62%	84.91%	85.11%	85.26%	85.37%	85.45%	37	113	148	185	223	267	321		
	39	84.75%	85.02%	85.20%	85.34%	85.44%	85.52%	39	114	146	184	232	266	315		
	41	84.87%	85.11%	85.28%	85.41%	85.50%	85.58%	41	114	144	179	221	259	313		
	43	84.97%	85.20%	85.36%	85.48%	85.56%	85.63%	43	111	145	180	221	254	312		
	45	85.07%	85.28%	85.43%	85.54%	85.62%	85.68%	45	111	141	179	214	268	321		
	47	85.15%	85.35%	85.49%	85.59%	85.66%	85.72%	47	108	137	170	214	244	290		
	49	85.23%	85.42%	85.54%	85.64%	85.71%	85.76%	49	108	141	170	207	246	290		
51	85.30%	85.48%	85.60%	85.68%	85.75%	85.79%	51	110	135	164	199	235	279			
53	85.36%	85.53%	85.64%	85.72%	85.78%	85.83%	53	104	132	164	201	233	280			
55	85.42%	85.58%	85.69%	85.76%	85.82%	85.86%	55	104	130	167	206	244	280			
57	85.48%	85.63%	85.73%	85.80%	85.85%	85.89%	57	107	139	168	200	234	279			
59	85.53%	85.67%	85.76%	85.83%	85.88%	85.91%	59	110	135	161	191	226	274			
61	85.58%	85.71%	85.80%	85.86%	85.90%	85.93%	61	114	136	166	202	234	275			
63	85.62%	85.75%	85.83%	85.89%	85.93%	85.96%	63	109	141	164	205	240	269			
65	85.66%	85.78%	85.86%	85.91%	85.95%	85.98%	65	109	140	165	201	237	272			
67	85.70%	85.81%	85.89%	85.94%	85.97%	86.00%	67	113	160	171	211	262	320			
69	85.74%	85.84%	85.91%	85.96%	85.99%	86.02%	69	126	148	182	219	253	295			
71	85.77%	85.87%	85.94%	85.98%	86.01%	86.03%	71	118	147	182	211	249	293			
73	85.80%	85.90%	85.96%	86.00%	86.03%	86.05%	73	115	138	168	198	236	273			
75	85.83%	85.92%	85.98%	86.02%	86.05%	86.07%	75	113	156	196	232	261	300			
77	85.86%	85.95%	86.00%	86.04%	86.06%	86.08%	77	124	153	186	221	259	297			
79	85.88%	85.97%	86.02%	86.06%	86.08%	86.09%	79	126	152	184	218	273	323			
81	85.91%	85.99%	86.04%	86.07%	86.09%	86.11%	81	134	167	201	240	297	326			

Figure 32 Discretization analysis for a 4.5 m x 4.5 m billboard receiver

This analysis is conducted with different receiver sizes to identify a selection criterium for the axial and circumferential number of control volumes. The results are reported in Figure 33. All the considered receivers have aspect ratio (ratio between height and width) equal to 1 and their tube diameter has been optimized. The reported Ns and Nax correspond to the necessary values to obtain an error inferior to 0.25 % with respect to the “real” value computed with really high discretization numbers. This analysis allows to select the correct discretization for the considered receiver size: increasing the size of the receiver it is necessary to increase almost linearly the number of axial elements, while for the circumferential direction it appears that after a certain threshold of 30-35 it becomes useless to furtherly increase the discretization.

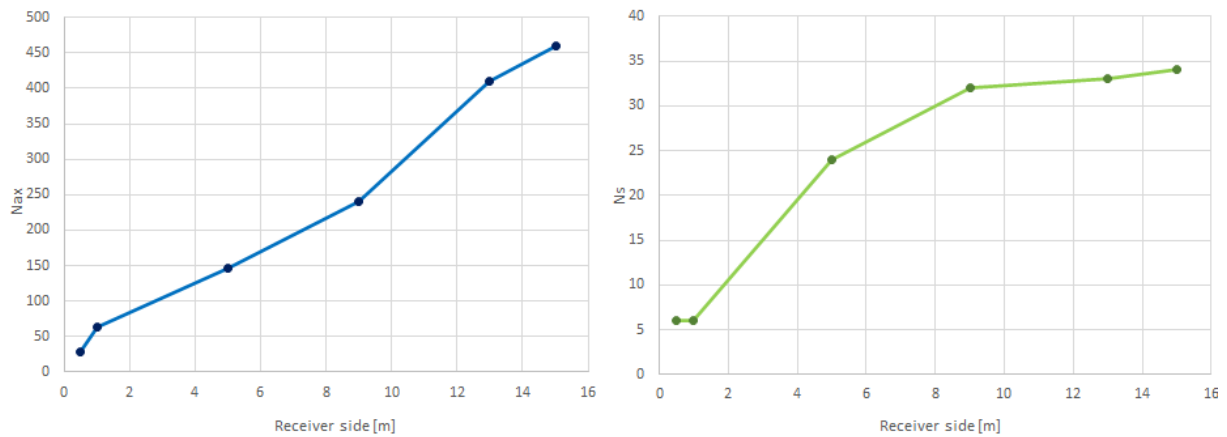


Figure 33 Required number of control volumes for different receiver sizes

The billboard model is furtherly improved by changing it from single pass to multi pass. The receiver is divided in four panels, two for each of the two flow paths, and this contributes to furtherly reduce the size of the radiative resistance matrix. Additionally, conduction between adjacent circumferential control volumes is implemented, improving the model accuracy, and reducing the number of axial and circumferential elements necessary to adequately model the receiver. This model is again studied to evaluate the effect of axial and circumferential discretization on results. Good results are obtained with lower number of axial and circumferential volumes and most importantly accurate results are obtained even with very low discretization values, as shown in Figure 34. Efficiency increases with the number of axial control volumes, while it remains almost constant for a number of circumferential elements higher than 3 (The number specified by N_s is always to be intended as the number of control volumes in a quarter of circumference, the actual number of elements is 4 times N_s). The maximum absolute error always remains below 0.5 %.

In this model there is a limit to the number of control volumes that can be specified and once this threshold is overcome the model is incapable of solving the system. This model proves to be more robust, and the smaller radiative resistance matrix reduces the computational time required. For these reasons this final version multi-pass model, once it is implemented, is preferred to the single-pass model used in the first part of the work. The discretization for the considered configurations and different receivers is selected according to the results obtained with this analysis, to guarantee the best utilization of the model and accuracy of the results.

1m x 1m						4m x 4m							
η [%]	Ns					η [%]	Ns						
	1	2	3	4	5		1	2	3	4	5		
Nax	1	84.01%	83.89%	84.01%	84.02%	84.01%	Nax	1	86.52%	86.28%	86.39%	86.41%	86.40%
	10	83.97%	83.89%	84.02%	84.04%	84.04%		10	86.51%	86.27%	86.39%	86.41%	86.40%
	50	84.02%	84.06%	84.22%	84.26%	LIMIT		50	86.52%	86.33%	86.46%	86.48%	86.48%
	200	84.11%	84.26%	LIMIT	LIMIT			200	86.55%	86.49%	86.65%	86.68%	86.68%
	1000	84.19%	LIMIT					1000	86.71%	86.80%	LIMIT	LIMIT	LIMIT
	5000	LIMIT						5000	86.90%	LIMIT			
7m x 7m						10m x 10m							
η [%]	Ns					η [%]	Ns						
	1	2	3	4	5		1	2	3	4	5		
Nax	1	87.25%	86.87%	86.97%	86.97%	86.96%	Nax	1	86.35%	86.11%	86.24%	86.25%	86.24%
	10	87.22%	86.84%	86.94%	86.95%	86.93%		10	86.33%	86.09%	86.22%	86.23%	86.22%
	50	87.22%	86.86%	86.98%	86.99%	86.98%		50	86.33%	86.12%	86.25%	86.27%	86.26%
	200	87.22%	86.96%	87.09%	87.11%	87.11%		200	86.35%	86.20%	86.35%	86.38%	86.38%
	1000	87.31%	87.25%	87.43%	LIMIT	LIMIT		1000	86.44%	86.46%	86.64%	LIMIT	LIMIT
	5000	87.63%	LIMIT	LIMIT				5000	86.65%	LIMIT	LIMIT		
13m x 13m						16m x 16m							
η [%]	Ns					η [%]	Ns						
	1	2	3	4	5		1	2	3	4	5		
Nax	1	87.32%	86.94%	87.05%	87.05%	87.04%	Nax	1	87.34%	86.79%	86.88%	86.87%	86.85%
	10	87.30%	86.92%	87.02%	87.03%	87.01%		10	87.30%	86.75%	86.83%	86.83%	86.80%
	50	87.29%	86.92%	87.04%	87.04%	87.03%		50	87.30%	86.75%	86.84%	86.84%	86.82%
	200	87.29%	86.98%	87.11%	87.12%	87.11%		200	87.29%	86.79%	86.89%	86.89%	86.87%
	1000	87.33%	87.19%	LIMIT	LIMIT	LIMIT		1000	87.27%	86.95%	87.10%	87.11%	LIMIT
	5000	87.57%	87.60%					5000	87.52%	87.43%	87.60%	LIMIT	

Figure 34 Discretization analysis of the multi-pass receiver model for different receiver sizes

2.4. Piping

In the case of modular solar tower plants the piping between the storage tanks and solar towers must be carefully addressed as the system requires an extended and considerably long piping network. For the design and performance evaluation of the piping subsystem a new model is developed in Matlab® as part of this thesis work. The model is able to determine the dimensions of the whole piping system and to evaluate thermal and pressure losses and to estimate the costs, thus providing a complete and extensive characterization of the piping subsystem. This model can be used for systems with any number of modules, any module size and layout (surrounded field, south or north polar field) as long as it is considered included in a rectangle, and with solar salts or liquid sodium as heat transfer fluid. All the modules are assumed to have the same geometric characteristics, such as solar field size, tower height, receiver dimension; and the same thermal characteristics, such as power absorbed by the HTF in the receiver, receiver inlet and outlet HTF temperature, and pressure drops. Storage and power block subsystems are assumed to be in a rectangular region at the centre of the plant with size equivalent to the size of one module as shown in Figure 35. It is assumed that all the modules always operate in the same conditions and with the same mass flow rate.

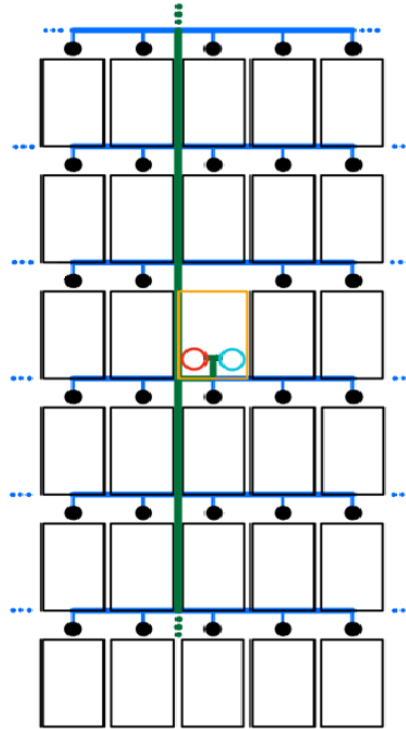


Figure 35 Modular field modelled layout

Each line depicted in Figure 35 actually represents two pipes: one pipe responsible for delivering the cold HTF and one pipe for the return of the hot HTF to the storage. In the cold network the pipes divide into smaller ones as the fluid is delivered to the furthest modules, while in the hot network the pipes merge as the fluid is recollected and returned to the storage system. To design the piping system many input parameters are required. The first important parameter is the matrix that describes the number of modules in the plant and their position. This is a square matrix with odd number of rows/columns, a 2 in the middle of the matrix representing the storage and power block position, ones in the positions occupied by modules and zeros in the remaining positions and at the borders of the matrix (Figure 36).

0	0	0	0	0	0	0
0	0	1	1	1	0	0
0	1	1	2	1	1	0
0	1	1	1	1	1	0
0	0	0	0	0	0	0

Figure 36 Input matrix for a possible 12 modules plant layout

The complete geometry of the modules must be defined: module width, module height, horizontal and vertical spacing between modules, distance between the tower and the module, tower height. Ambient temperature T_{amb} and relative humidity RH need to be specified to estimate the necessary ambient conditions. Dew point temperature T_{dp} is computed with Magnus-Tetens [26] approximation as described in Equation (6).

$$T_{dp} = \frac{237.7 \cdot \left(\frac{17.27 \cdot T_{amb}}{237.7 + T_{amb}} + \log RH \right)}{17.27 - \left(\frac{17.27 \cdot T_{amb}}{237.7 + T_{amb}} + \log RH \right)} \quad (6)$$

Clear sky emissivity ε_{sky} is estimated with Equation (7) from the dew point temperature, while sky temperature T_{sky} is evaluated from ambient temperature with Swinbank's formula [27] as shown in Equation (8).

$$\varepsilon_{sky} = 0.73223 + 0.006349 \cdot T_{dp} \quad (7)$$

$$T_{sky} = 0.00552 \cdot T_{amb}^{1.5} \quad (8)$$

The temperature of the whole surrounding environment is computed from sky and ground properties as shown in Equation (9), assuming a ground emissivity ε_{ground} of 0.95.

$$T_{surr} = \left(\frac{\varepsilon_{sky} \cdot T_{sky}^4 + \varepsilon_{ground} \cdot T_{amb}^4}{\varepsilon_{sky} + \varepsilon_{ground}} \right)^{\frac{1}{4}} \quad (9)$$

One important design parameter is the heat transfer fluid speed in the piping system: HTF speed influences piping diameters, heat losses and pressure losses and for the proper selection of this parameter an optimization procedure is used, as it will be discussed later in this section. Another important design parameter is the allowed maximum external temperature of the pipes, as it determines the thickness of the insulants that envelop the pipes. In this work the allowed maximum external temperature is considered equal to 40 °C. In the case of sodium as heat transfer fluid three different insulant materials are used, AISI 316L stainless steel is used as material for the pipes, and an external aluminium foil cladding is applied to reduce the emissivity. The considered insulant materials are ceramic fibre and two types of mineral fibre with different maximum operating temperatures and different costs (Table 6). Ceramic fibre is used as first insulant layer where temperatures are higher than 700 °C, while for more external layers at lower temperatures mineral fibres are used. The material thermal conductivity k is evaluated as function of material temperature T as shown in Equation (10).

$$k = \alpha \cdot T^2 + \beta \cdot T + \gamma \quad (10)$$

The properties of stainless steel and insulant materials are reported in Table 6 [28].

Material	α	β	γ	T_{\max} [°C]
Stainless steel 316L	$2.86 \cdot 10^{-6}$	$1.09 \cdot 10^{-2}$	13.76	-
Ceramic fibre	$1.88 \cdot 10^{-7}$	$2.75 \cdot 10^{-5}$	$3.75 \cdot 10^{-2}$	1100
Mineral fibre 1	$3.61 \cdot 10^{-7}$	$7.55 \cdot 10^{-5}$	$3.70 \cdot 10^{-2}$	640
Mineral fibre 2	$8.33 \cdot 10^{-7}$	$6.83 \cdot 10^{-5}$	$3.78 \cdot 10^{-2}$	350

Table 6 Thermal properties of piping materials [28]

Once all the input parameters have been defined the model computes the mass flow rate for each module/tower using Equation (11). It is estimated from the defined thermal power absorbed by the receiver Q_{mod} and the inlet $T_{in,rec}$ and outlet $T_{out,rec}$ temperature of the HTF in the receiver. Heat capacity cp is evaluated as function of temperature and HTF fluid type.

$$m_{mod} = \frac{Q_{mod}}{cp_{out} \cdot T_{out,rec} - cp_{in} \cdot T_{in,rec}} \quad (11)$$

The system is solved dividing the rows of the piping system, which connect horizontally the modules, in six sectors (R1, R2, ..., R6) while the vertical pipes connecting different rows of the system are divided into four sections (C1, C2, C3, C4). These sections are then divided into smaller subsections each time the mass flow changes due to an intersection and the length of each of this piping subsections is computed from the parameters that define the module geometry and spacing. The design of the piping system is based on two iterative procedures:

1. A first guess value is assumed for the maximum internal pressure P_{max} of the HTF.
2. Adopting a conservative approach this maximum value is used for the evaluation of the piping thickness in the whole system.
3. A first guess value for the outlet temperature is assumed in each subsection of the piping system while the inlet temperature is given by the previously solved subsections.
4. Thermal losses are computed and the outlet temperature in the subsection of piping is re-evaluated and compared with the assumed value.
5. This iterative procedure continues until convergence is reached on the outlet temperature of the subsection with a tolerance of 0.01 °C.
6. This procedure is initially applied to the cold branches of the piping system which come from the cold storage tank and connect all the modules in the plant.
7. The same procedure is then applied for the hot branches of the piping system which connect the towers with the hot storage tank.

8. When inlet and outlet temperature for each subsection of the cold and hot branches have been defined the model computes the pressure losses in the system
9. The maximum HTF pressure needed in the system is evaluated and compared with the initially assumed value.
10. The procedure is repeated until convergence on the maximum pressure is reached with a tolerance of 1 Pa.

The first thing evaluated by the model is the cold part of the piping system, responsible for delivering the HTF to the tower of each module. The model solves the system following the flow of the heat transfer fluid: the vertical piping sections that connect the cold storage tank to the different row sections are solved first and then each row section is solved. The riser and downcomer piping subsections inside the towers are considered adiabatic. The internal diameters D_{int} of the pipes are determined using Equation (12), where mass flow rate m_f is calculated from the number of modules connected to the considered pipe and from the HTF speed v_{HTF} . The HTF density ρ_{HTF} is computed as function of the heat transfer fluid type and the average temperature between inlet and outlet \bar{T}_{HTF} in the considered subsection.

$$D_{int} = \sqrt{\frac{4 \cdot m_f}{\pi \cdot \rho_{HTF} \cdot v_{HTF}}} \quad (12)$$

The thickness of the considered pipe subsection is computed as depicted in Equation (13) to resist the mechanical stresses. The admissible normal stress σ_{adm} is scaled with a security factor F equal to 1.5.

$$t = \frac{(P_{max} - P_{amb}) \cdot D_{int}}{2 \cdot \frac{\sigma_{adm}}{F} + (P_{max} - P_{amb})} \quad (13)$$

The internal heat transfer coefficient h_{int} is evaluated from the Nusselt number as shown in Equation (14). The Nusselt number is evaluated, in the case of sodium as heat transfer fluid, using Subbotin correlation [29], as described in Equation (15).

$$h_{int} = \frac{Nu \cdot k_{HTF}}{D_{int}} \quad (14)$$

$$Nu = 5 + 0.025 \cdot Pe^{0.8} \quad (15)$$

The internal convection thermal resistance R_{int} and the thermal resistance associated with the steel pipe thickness R_{steel} are computed using Equation (16) and (17)

respectively. The steel thermal conductivity k_{steel} is computed from the average temperature of the HTF \bar{T}_{HTF} in the considered piping subsection using Equation (10).

$$R_{int} = \frac{1}{\pi \cdot D_{int} \cdot h_{int}} \quad (16)$$

$$R_{steel} = \frac{\log \frac{D_{out}}{D_{int}}}{2 \cdot \pi \cdot k_{steel}} \quad (17)$$

The following steps are aimed at the evaluation of the necessary layers and thicknesses of the different insulant materials. If the inlet temperature of the HTF is higher than 600 °C a first layer of ceramic fibre is applied. The thickness of this layer is increased until the average temperature on the outer surface of the insulant reaches 600 °C and then a more economical mineral fibre insulant layer can be used. To evaluate the average outer surface temperature of the ceramic fibre insulant $\bar{T}_{out,cf}$ thermal power losses Q_{loss} are computed as shown in Equation (18), as function of temperature difference between the ambient and the HTF, piping subsection length L , and total thermal resistance R_{tot} between the ambient and the heat transfer fluid.

$$Q_{loss} = \frac{(\bar{T}_{HTF} - T_{amb}) \cdot L}{R_{tot}} \quad (18)$$

The total thermal resistance is evaluated using Equation (19), as the sum of internal convection thermal resistance, steel thermal resistance, insulant thermal resistance $R_{insulant}$, and external convection thermal resistance R_{ext} .

$$R_{tot} = R_{int} + R_{steel} + R_{insulant} + R_{ext} \quad (19)$$

In the first step the insulant resistance is given only by the ceramic fibre layer and is computed with Equation (20), as function of internal $D_{int,cf}$ and external $D_{out,cf}$ diameter of the layer, and ceramic fibre thermal conductivity k_{cf} evaluated at the average HTF temperature using Equation (10).

$$R_{insulant} = \frac{\log \frac{D_{out,cf}}{D_{int,cf}}}{2 \cdot \pi \cdot k_{cf}} \quad (20)$$

The external convection thermal resistance is evaluated as shown in Equation (21) as function of external heat transfer coefficient h_{ext} . This heat transfer coefficient is given by the sum of an external heat transfer convective coefficient, considered constant and equal to 10 W/m²K, and a radiative heat transfer coefficient (Equation (22)). The

radiative heat transfer coefficient is computed using Equation (23), as function of the aluminium foil cladding emissivity ε_{Al} , Stefan–Boltzmann constant σ_{SB} , the maximum allowed external temperature of the pipes $T_{ext,max}$, and the surroundings temperature T_{surr} obtained with Equation (9).

$$R_{ext} = \frac{1}{\pi \cdot D_{out,cf} \cdot h_{ext}} \quad (21)$$

$$h_{ext} = h_{conv} + h_{rad} \quad (22)$$

$$h_{rad} = \varepsilon_{Al} \cdot \sigma_{SB} \cdot (T_{ext,max}^2 + T_{surr}^2) \cdot (T_{ext,max} + T_{surr}) \quad (23)$$

Finally, the average outer surface temperature of the insulant ceramic fibre $\bar{T}_{out,cf}$ can be estimated as shown in Equation (24).

$$\bar{T}_{out,cf} = T_{amb} + \frac{Q_{loss} \cdot R_{ext}}{L} \quad (24)$$

This is not the real temperature at the outer surface of the ceramic fibre layer, but it serves as parameter to design the thickness of this layer. Once the average outer surface temperature of the ceramic fibre insulant computed in this way reaches a temperature below 600 °C mineral fibre 1 is used as next insulation layer as it has a lower cost with respect to ceramic fibre. The same procedure used for the evaluation of the ceramic fibre layer thickness is used for the mineral fibre 1 layer, considering in $R_{insulant}$ the additional insulant layer. In this case the thickness of the layer is increased until the average outer surface temperature of the mineral fibre 1 insulant reaches a temperature below 300 °C. At this point the more economical insulant ceramic fibre 2 is used. The thickness of this last layer is increased until the average outer surface temperature is below the set external maximum temperature $T_{ext,max}$. When the insulant layers have been designed the actual thermal power losses are computed and used to check that the temperatures of the different insulating layers really match the material temperature limits, and the outlet temperature of the heat transfer fluid from the considered piping subsection is evaluated. This computed outlet temperature is compared with the initially assumed one as part of the iterative procedure until convergence is reached.

The same procedure is applied to the hot branch of the piping system, responsible for collecting the heat transfer fluid from the towers and delivering it to the hot storage tank. In this case the piping system is solved in the opposite direction, starting from the row sections and, following the flow, reaching the vertical piping sections. When two pipes recollecting the hot HTF merge Equation (25) is used to determine the resulting temperature. The resulting temperature represents the inlet temperature for

the merged pipe $T_{in,merged}$ and is given by the weighted average of the outlet temperatures of the merging pipes $T_{out,i}$, proportionally to their mass flow rates $m_{f,i}$.

$$T_{in,merged} = \frac{\sum m_{f,i} \cdot T_{out,i}}{\sum m_{f,i}} \quad (25)$$

Additionally, both in the cold and in the hot subsystem the presence of expansion loops is considered. These loops are placed each 30 m of pipe length to reduce the generated expansion stress and displacement caused by thermal expansion or contraction. The length of this expansion loops must be defined to guarantee enough flexibility, but as small as possible to reduce support feasibility, vibration tendency and costs.

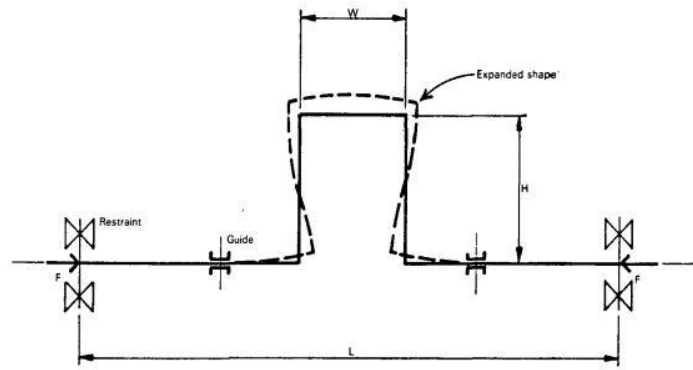


Figure 37 Expansion loop

The width of the loop was estimated for each piping subsection using Equation (26) [30], as a function of expansion coefficient of SS316L α_{exp} , difference between the inlet HTF temperature $T_{in,HTF}$ and ambient temperature, internal diameter of the pipe, total length of the considered pipe subsection L , and number of loops in the subsection N_{loops} . The total length of the loop is given by the sum of the width W and the length of the two perpendicular legs H , considered of the same length as W .

$$W = 15 \cdot \left(\alpha_{exp} \cdot (T_{in,HTF} - T_{amb}) \cdot D_{int} \cdot \frac{L}{N_{loops}} \right)^{0.5} \quad (26)$$

This whole procedure allows to completely define the geometry and thermal behaviour of each piping subsection, both for the cold and hot branches of the system: pipes length, tube diameters and insulant thicknesses are defined, and temperatures, and thermal losses are evaluated. With these results the model can start the evaluation of pressure losses in the piping system. Pressure losses are divided into distributed and concentrated pressure losses. Distributed pressure losses are evaluated using Equation (27), as function of friction factor f , pipe length L , internal diameter, heat transfer fluid density ρ_{HTF} , evaluated as function of temperature, and HTF speed.

$$Dp_{distributed} = 0.5 \cdot f \cdot \frac{L}{D_{int} \cdot \rho_{HTF}} \cdot v_{HTF}^2 \quad (27)$$

The friction factor is computed as function of Reynolds number and iteratively using Colebrook-White equation as shown in Equation (28), where ε is the pipe effective roughness.


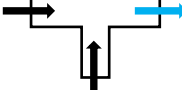
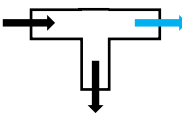
$$f = \frac{64}{Re}, \quad Re \leq 2000$$

$$\frac{1}{\sqrt{f}} = -2 \log_{10} \left(\frac{\varepsilon}{3.72 \cdot D_{int}} + \frac{2.51}{Re \cdot \sqrt{f}} \right), \quad Re > 2000 \quad (28)$$

Concentrated pressure losses are evaluated for each piping subsection using Equation (29) as function of a concentrated loss coefficient k . This coefficient accounts for the presence of specific components located at the beginning of the considered pipe and for the presence of elbows due to the expansion loops.

$$Dp_{concentrated} = 0.5 \cdot k \cdot \rho_{HTF} \cdot v_{HTF}^2 \quad (29)$$

The concentrated loss coefficient is determined by the presence of one of three different components at the beginning of the pipe: elbows, tee junctions, and cross junctions. Tee and cross junctions are furtherly divided in two categories: diverging junctions if flow divides and converging junctions if flows merge. Diverging junctions are again divided into two categories: straight diverging junction if the flow in the considered pipe follows the same direction of the inlet flow, side branch diverging junction if the flow curves towards left or right with respect to the inlet flow. The considered elements and their types are reported in Table 7. For each piping subsection the type of the concentrated loss element is defined by the presence of modules and the corresponding necessary connecting pipes.

Loss element	Type	Direction	Scheme
Elbow	-	-	
Tee	Converging	-	
	Diverging	Straight	

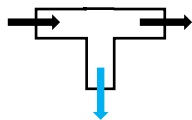
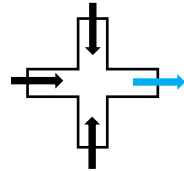
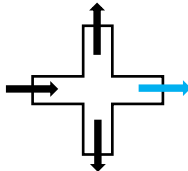
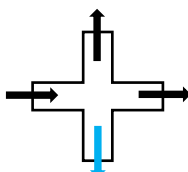
		Side branch	
Cross	Converging	-	
	Diverging	Straight	
		Side branch	

Table 7 Concentrated loss elements and types

In the case of elbows, the concentrated loss factor is evaluated as shown in Equation (30) as function of Reynolds number [31]. This equation is also used for the computation of concentrated pressure losses due to the four elbows of each expansion loop that is present in the considered pipe subsection.

$$k = 1.49 \cdot Re^{-0.145} \quad (30)$$

For converging tees, the concentrated loss factor $k_{tee,conv}$ is given by the sum of two contributions: one due to the entering straight flow and one due the entering side branch flow, as shown in Equation (31). The coefficients $\xi_{c,st}$ and $\xi_{c,s}$ are interpolated from tables as function of the flow rate ratio $\frac{W_s}{W_c}$, and as function of pipe section ratio $\frac{F_c}{F_s}$, as represented in Figure 38 [32].

$$k_{tee,conv} = \frac{\xi_{c,st}}{\left(1 - \frac{W_s}{W_c}\right) \cdot \left(\frac{F_c}{F_s}\right)^2} + \frac{\xi_{c,s}}{\left(\frac{W_s}{W_c} \cdot \frac{F_c}{F_s}\right)^2} \quad (31)$$

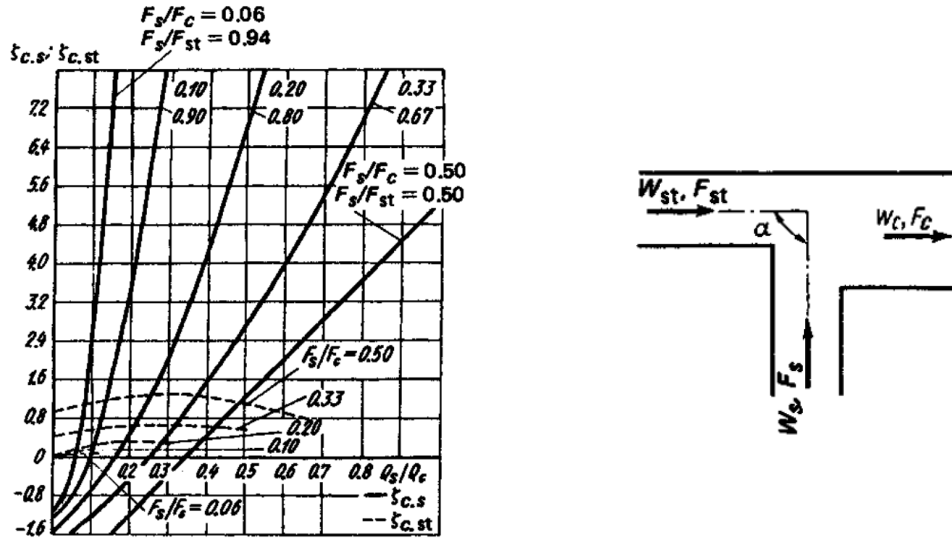


Figure 38 Loss coefficients $\xi_{c,st}$ and $\xi_{c,s}$ as function of flow rates and pipe sections and converging tee scheme [32]

In the case of diverging tees, for the straight line flow the concentrated loss factor $k_{tee,div,st}$ is evaluated using Equation (32), as function of the straight-line pipe diameter D_{st} . The coefficients a, b, c, d, e are also evaluated as function of D_{st} [32].

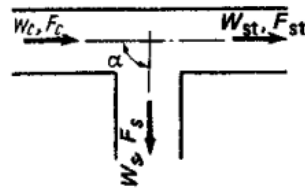


Figure 39 Diverging tee scheme

$$k_{tee,div,straight} = a \cdot \frac{(b \cdot 0.0254 - D_{st})}{c \cdot 0.0254} + d \cdot \frac{(D_{st} - e \cdot 0.0254)}{c \cdot 0.0254} \tag{32}$$

For the side branch flow in diverging tees the concentrated loss factor is computed as shown in Equation (33), as function of the side branch pipe diameter D_s . The coefficients a, b, c, d, e are also evaluated as function of D_s [32].

$$k_{tee,div,side} = a \cdot \frac{(b \cdot 0.0254 - D_s)}{c \cdot 0.0254} + d \cdot \frac{(D_s - e \cdot 0.0254)}{c \cdot 0.0254} \tag{33}$$

Converging cross junctions were modelled using the same equations from converging tee junctions, considering two side branches instead of one. The loss coefficient $k_{cross,conv}$ was computed as shown in Equation (34). The coefficients $\xi_{c,st}$, $\xi_{c,s1}$ and $\xi_{c,s2}$ are interpolated from the same tables as in the case of converging tee junctions, as

function of the flow rate ratios $\frac{W_{s1}}{W_c}$ and $\frac{W_{s2}}{W_c}$, and as function of pipe section ratios $\frac{F_c}{F_{s1}}$ and $\frac{F_c}{F_{s2}}$.

$$k_{cross,conv} = \frac{\xi_{c,st}}{\left(1 - \frac{W_{s1}}{W_c} - \frac{W_{s2}}{W_c}\right) \cdot \left(\frac{F_c}{F_s}\right)^2} + \frac{\xi_{c,s1}}{\left(\frac{W_{s1}}{W_c} \cdot \frac{F_c}{F_{s1}}\right)^2} + \frac{\xi_{c,s2}}{\left(\frac{W_{s2}}{W_c} \cdot \frac{F_c}{F_{s2}}\right)^2} \quad (34)$$

In the case of diverging cross junctions the same equations (Equation (32) and Equation (33)) from diverging tee junctions, with different coefficients, were used both for straight line $k_{cross,div,straight}$ and side branch $k_{cross,div,side}$ concentrated loss factor.

Once concentrated and distributed pressure losses have been computed for all the piping subsections the total pressure losses for the flow path connecting the storage system to each one of the towers is evaluated, accounting for both the cold and the hot path. In this way the maximum pressure loss due to the worst flow path is identified. In the case that solar salts are selected as HTF a direct storage configuration is considered and therefore pressure losses due to the geodetical head in the riser in the towers are added to the piping pressure losses. In the case of sodium as HTF an indirect storage configuration is considered and therefore the geodetic term is not considered in the pressure losses as it is recovered in the downcomer of the solar tower. Finally, the pressure losses due to the receiver, provided by the receiver thermal model, are added to evaluate the maximum pressure needed in the whole piping system. This pressure value is compared with the initially assumed value to proceed with the iterative procedure that includes the whole model, starting again from the evaluation of diameters and thermal losses. When convergence is obtained the pump electric power consumption W_{pump} is evaluated as shown in Equation (35). It is function of the total mass flow rate in the piping system $m_{f,tot}$, the maximum pressure drops Dp_{max} , HTF density ρ_{HTF} , the design hydraulic efficiency η_{hydr} , and the electro-mechanic efficiency η_{el} .

$$W_{pump} = \frac{m_{f,tot} \cdot Dp_{max}}{\rho_{HTF} \cdot \eta_{hydr} \cdot \eta_{el}} \quad (35)$$

Regulation valves are necessary at the base of each tower to ensure isobaric mixing. Additionally, two constraints on pressures are set: the pressure at the receiver outlet should not be lower than the ambient pressure to avoid the HTF evaporation, and the pressure in the hot storage tanks should not be lower than the ambient one. Also, supports for the piping structure are assumed each 15 m and for each expansion loop. In this way the whole piping system has been designed. The main results provided by the model are:

- Piping diameters and insulant thicknesses
- Thermal losses for each pipe subsection and for the whole system.

- Piping system thermal efficiency.
- HTF temperature difference between cold storage tank and receivers.
- HTF temperature difference between receivers and hot storage tank.
- Volume of HTF required.
- Pressure difference needed from the pump.
- Pump electric consumption.

As previously mentioned, the design of the piping system significantly depends on the chosen value of HTF velocity. For this reason, the selection of this parameter is always the result of an optimization procedure. Pump electric power consumption W_{pump} and thermal power losses $Q_{loss,th}$ are evaluated for a range of HTF velocities. Heat losses tend to decrease at higher HTF speed while pressure losses tend to increase, as depicted in Figure 40. The total power losses $Q_{loss,tot}$ are computed as shown in Equation (36), where the pump power consumption is converted with a reference power block efficiency $\eta_{PB,ref}$ equal to 0.44. The HTF velocity is selected to minimize the total losses computed in this way.

$$Q_{loss,tot} = Q_{loss,th} + \frac{W_{pump}}{\eta_{PB,ref}} = Q_{loss,th} + Q_{loss,pump}$$

(36)

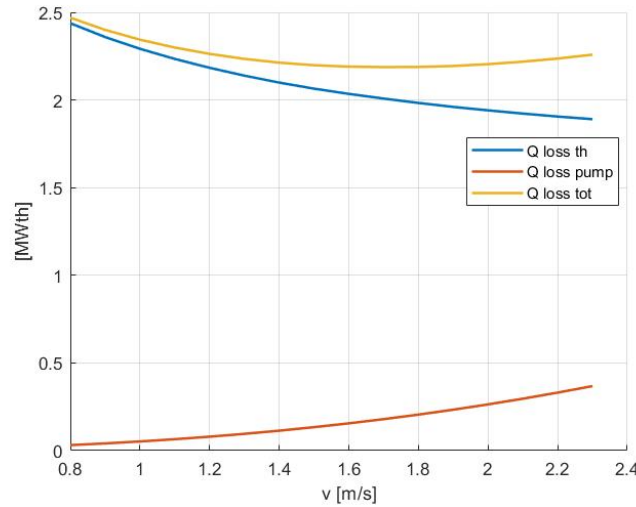


Figure 40 Piping system losses as function of HTF velocity

Once the optimal HTF velocity is identified the obtained design (piping diameters and insulant thicknesses) can be used to perform off-design analysis and evaluate losses at any given condition, as discussed in Section 2.6, Annual simulation. In particular, the effect of ambient temperature on system performances is analysed. The results show that ambient temperature has very limited effect on the thermal efficiency of the system: lower ambient temperatures lead to a reduction of the thermal conductivity of the external mineral fibre insulant layer and to a reduction of the external surface temperature of the pipes, minimizing the change in temperature differences between surface and ambient, and consequently the change in thermal power losses.

2.5. TES and PB

The main focus of this work is the modelling of the solar field, the receiver, and the piping subsystems for their importance in the modularization of solar tower plants. The thermal energy storage and the power block subsystem instead are the same between the considered modular plants and the single field tower plant, making them of secondary importance when comparing the two configurations. Additionally, the design and the off-design evaluation of solar field, receiver and piping is already complex and time consuming due to the very detailed modelling. For these reasons the TES and the power block are approached in much simpler way.

The considered TES storage system uses solar salts as storage medium (NaCl – MgCl₂). A simple control strategy is applied given the thermal storage capacity: the system stores thermal power when it is provided in excess from the solar fields and provides thermal power to the power block when the power collected by the solar fields is insufficient. The storage system is considered as an ideal system with no thermal losses. The power block is based on a supercritical CO₂ Brayton cycle and operates with constant efficiency as long as the ambient temperature remains below the threshold of 30 °C. The modelling of these two subsystems is implemented in Matlab®. Once the rated electric power of the power block $P_{el,design}$ and its design efficiency $\eta_{PB,design}$ are defined, the solar multiple, which represents how over-dimensioned is the solar field with respect to the power block, and therefore the amount of excess energy that can be stored, can be evaluated as shown in Equation (37). The solar multiple is computed at design conditions as function of design direct normal irradiance DNI_{design} , heliostat area of each module A_{SF} , design optical efficiency $\eta_{opt,design}$, receiver design thermal efficiency $\eta_{th,design}$, number of modules in the plant N_{mod} , and piping design thermal efficiency $\eta_{piping,design}$.

$$SM = \frac{DNI_{design} \cdot A_{SF} \cdot \eta_{opt,design} \cdot \eta_{th,design} \cdot N_{mod} \cdot \eta_{piping,design}}{\frac{P_{el,design}}{\eta_{PB,design}}} \quad (37)$$

The auxiliaries design efficiency $\eta_{aux,design}$ is evaluated using Equation (38), from the HTF pump electric consumption at design conditions $W_{pump,design}$.

$$\eta_{aux,design} = \frac{P_{el,design} - W_{pump,design}}{P_{el,design}} = \frac{P_{el,net,design}}{P_{el,design}} \quad (38)$$

The design solar to electric efficiency $\eta_{STE,design}$ is computed with Equation (39), as function of the design efficiencies of the plant subsystems.

$$\eta_{STE,design} = \eta_{opt,design} \cdot \eta_{th,design} \cdot \eta_{piping,design} \cdot \eta_{PB,design} \cdot \eta_{aux,design} \quad (39)$$

2.6. Annual simulation

When the whole plant has been defined in all its subsystems (solar field, receiver, piping, TES, power block) the off-design behaviour of each of these subsystems must be assessed to estimate the annual energy production of the plant. The hourly energy production is then estimated from the DNI data for each hour of the year in the chosen location.

The azimuth and elevation angles for each hour of the year are computed for the given location coordinates. The solar field optical efficiency is evaluated with a parametric analysis in SolarPILOT (Section 2.2, Solar field). Optical efficiency is computed for different sun positions given by the combination of different azimuth γ_s and elevation α_s angles. The azimuth angle is varied from -140° to 140° with intervals of 20° , while the elevation angle is varied from 0° to 80° with intervals of 10° . The result of the performance analysis is a table with the values of optical efficiency for 135 different sun position. This table is interpolated for the required values of elevation and azimuth to evaluate optical efficiency $\eta_{opt,i}$ for any sun position and can be represented as shown in Figure 41.

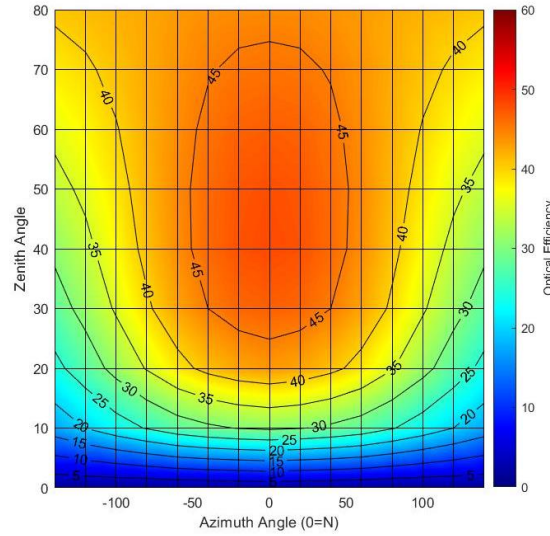


Figure 41 Example of optical efficiency map as function of azimuth and elevation angles

The receiver thermal power input $Q_{in,rec,i}$ for each hour i of the year is computed as shown in Equation (40), as function of DNI_i , solar field heliostat area A_{SF} , and optical efficiency evaluated from $\gamma_{s,i}$ and $\alpha_{s,i}$. The solar field annual optical efficiency is computed using Equation (41).

$$Q_{in,rec,i} = DNI_i \cdot A_{SF} \cdot \eta_{opt,i} \quad (40)$$

$$\eta_{opt,year} = \frac{\sum_{i=1}^{8760} Q_{in,rec,i}}{\sum_{i=1}^{8760} DNI_i \cdot A_{SF}} = \frac{Q_{in,rec,year}}{Q_{sun,year}} \quad (41)$$

The receiver off-design thermal efficiency is evaluated by simply scaling the values of the design heat flux map obtained from SolarPILOT from 20% to 120%. This approximation is possible because it has been proven in previous works [33] that the thermal efficiency of the receiver is only weakly influenced by the heat flux distribution. The main dependency is only on the overall receiver thermal input. Four off-design heat flux maps are obtained by scaling with a factor of 0.2, 0.4, 0.7 and 1.2 the design heat flux map. These obtained heat flux maps are used as inputs for the receiver thermal model described in Section 2.3, Receiver, to obtain the receiver thermal efficiency and the pressure losses. The inlet and outlet temperature of the heat transfer fluid in the receiver are kept constant and equal to the design temperatures. When the receiver thermal input is lower than 20% of the design value the defocusing of the heliostats and the shutdown of the HTF pump are assumed. The obtained thermal efficiencies and pressure drops are then interpolated for any needed receiver thermal input ratio, as shown in Figure 42.

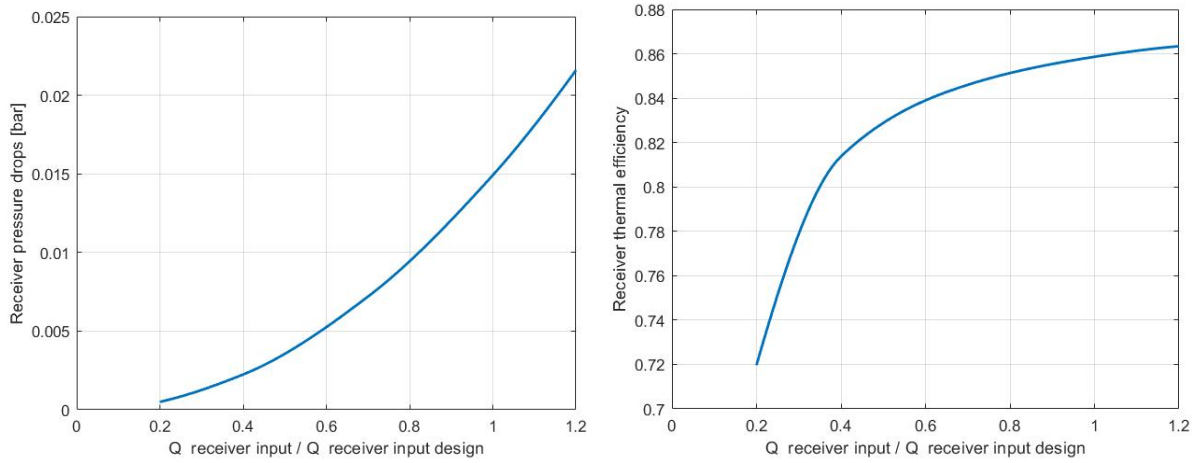


Figure 42 Receiver pressure drops and thermal efficiency as function of receiver thermal power input

The thermal power absorbed by the HTF in the receivers $Q_{HTF,i}$ for each hour of the year is evaluated using Equation (42), as a function of the receiver thermal power input, the receiver thermal efficiency $\eta_{th,i}$, evaluated from the ratio $\frac{Q_{in,rec,i}}{Q_{in,rec,design}}$, and the number of modules in the plant N_{mod} . The receiver annual thermal efficiency $\eta_{th,year}$ is computed as shown in Equation (43). The energy absorbed by the HTF in the receiver in a year is one of the key parameters for the technical evaluation of the performances of the solar field and it is used to compute the levelized cost of heat (LCOH).

$$Q_{HTF,i} = Q_{in,rec,i} \cdot \eta_{th,i} \cdot N_{mod} \quad (42)$$

$$\eta_{th,year} = \frac{\sum_{i=1}^{8760} Q_{HTF,i}}{\sum_{i=1}^{8760} Q_{in,rec,i}} = \frac{Q_{HTF,year}}{Q_{in,rec,year}} \quad (43)$$

The piping off-design thermal efficiency and pump electric consumption are evaluated from the off-design values provided by the receiver model for the thermal power absorbed by the HTF in the receiver and the pressure losses in off-design conditions. The model (Section 2.4, Piping) evaluates the piping system behaviour keeping the geometry defined in the design phase and computing the HTF speed v_{HTF} for each piping subsection using Equation (44), as a function of mass flow rate m_f , pipe internal diameter D_{int} and HTF density ρ_{HTF} .

$$v_{HTF} = \frac{4 \cdot m_f}{\rho_{HTF} \cdot \pi \cdot D_{int}^2} \quad (44)$$

The results obtained are then interpolated to obtain the piping thermal efficiency and the HTF pump electric power consumption W_{pump} for any needed value of thermal power input in the receiver, as shown in Figure 43.

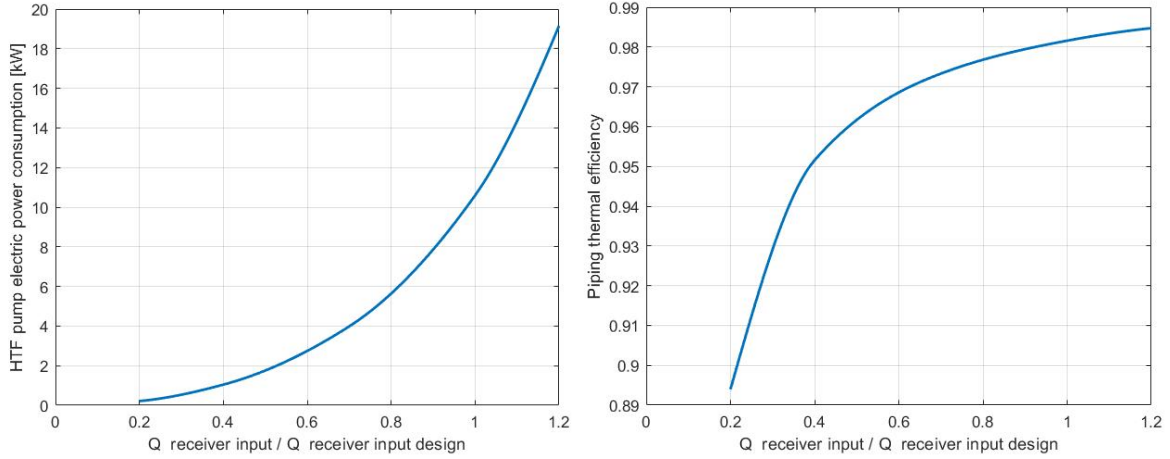


Figure 43 HTF pump electric consumption and piping thermal efficiency as function of receiver thermal power input

The net power delivered from the piping system to the storage system $Q_{HTF,net,i}$ for each hour of the year is evaluated using Equation (45), as a function of thermal power absorbed by the HTF in the receivers $Q_{HTF,i}$, and piping thermal efficiency $\eta_{piping,i}$, evaluated from the ratio $\frac{Q_{in,rec,i}}{Q_{in,rec,design}}$. The annual piping thermal efficiency $\eta_{piping,year}$ is computed with Equation (46).

$$Q_{HTF,net,i} = Q_{HTF,i} \cdot \eta_{piping,i} \quad (45)$$

$$\eta_{piping,year} = \frac{\sum_{i=1}^{8760} Q_{HTF,net,i}}{\sum_{i=1}^{8760} Q_{HTF,i}} = \frac{Q_{HTF,net,year}}{Q_{HTF,year}} \quad (46)$$

The net thermal power provided by the piping system enters the storage system and is used to operate the power block. The excess is stored and used when the power

provided by the solar field is insufficient to operate the power block at rated capacity. In the considered model the storage system is an ideal system with no thermal losses: all the thermal power that reaches the storage is eventually converted into electricity. When the storage system reaches its full capacity heliostats are defocused and only the power necessary to run the power block is collected while the excess power $Q_{excess,i}$ is lost. The power block efficiency $\eta_{PB,i}$ is considered constant for any load as previously mentioned in Section 2.5, TES and PB. The electric power production for each hour of the year $P_{el,i}$ is evaluated using Equation (47), where the thermal power input in the power block $Q_{in,PB,i}$ is given by the available net thermal power provided by the piping system and by the available stored energy in the TES system. The net electric power production $P_{el,net,i}$ is computed accounting for the HTF pump consumption $W_{pump,i}$ as showed in Equation (48).

$$P_{el,i} = Q_{in,PB,i} \cdot \eta_{PB,i} \quad (47)$$

$$P_{el,net,i} = P_{el,i} - W_{pump,i} \quad (48)$$

The annual auxiliaries efficiency $\eta_{aux,year}$ and the annual energy production AEP are evaluated as shown in Equation (49). The annual energy production is one of the key parameters for the technical evaluation of the performances of the plant and is used for the computation of the levelized cost of electricity (LCOE).

$$\eta_{aux,year} = \frac{\sum_{i=1}^{8760} P_{el,net,i}}{\sum_{i=1}^{8760} P_{el,i}} = \frac{AEP}{P_{el,year}} \quad (49)$$

The annual solar to electric efficiency $\eta_{STE,year}$ is computed as shown in Equation (50) as function of the annual efficiency of all the subsystems of the plant.

$$\eta_{STE,year} = \eta_{opt,year} \cdot \eta_{th,year} \cdot \eta_{piping,year} \cdot \eta_{PB,year} \cdot \eta_{aux,year} \quad (50)$$

During the year heliostat defocusing is considered when the storage system has reached full capacity and the power block is operating at full load. It is estimated using an equivalent number of hours computed using Equation (51), as a function of the power that is lost and not collected by the system $Q_{excess,i}$ due to the defocusing.

$$h_{eq,def} = \frac{\sum_{i=1}^{8760} Q_{excess,i}}{\frac{P_{el,design}}{\eta_{PB,design}}} \quad (51)$$

Finally, the capacity factor CF of the plant is evaluated as shown in Equation (52).

$$CF = \frac{AEP}{8760 \cdot P_{el,design}} \quad (52)$$

2.7. Economic parameters

The techno-economic optimization of the different configurations analysed in this work requires many economic assumptions to compute important parameters as the levelized cost of heat (LCOH) and the levelized cost of electricity (LCOE). The optimization of parameters as tower height or receiver size requires cost correlation as function of these parameters. Finding reliable and updated cost correlations in literature is sometimes difficult. In this section a resume of the found costs and costs correlations for the main components of the plant are reported. The cost values considered most suitable are used for the economic evaluation of the plant configurations investigated in this work.

For the solar field three cost items are considered: land purchase, site improvement, and heliostat costs. For the selection of the appropriate cost estimates a series of values is analysed from different sources as reported in Table 17, Table 18 and Table 19 (Appendix A). For the tower cost different correlations are found depending on the type of the structure and on the used material as reported in Table 20. For the receiver cost different values and correlations are found in literature as shown in Table 21. Receiver cost is usually expressed as function of the thermal power input or as function of the receiver area. For the piping materials and components, the costs reported in Table 8 are used. The HTF pump cost is considered negligible with respect to the total piping system cost.

Piping				
Type	Value	Unit	Year	Reference
Stainless Steel SS 316L	52.8	k\$/m ³	2018	Bonanos 2019 [28]
Ceramic fiber	770	\$/m ³		
Mineral fiber 1	121	\$/m ³		
Mineral fiber 2	66	\$/m ³		
Valves	500	\$/unit	2021	Sarvghad 2022 [34]
Supports	$630 \cdot \log(D[m] \cdot 39.4) - 482$	\$/unit	2016	Stewart (2016) [35]

Sodium	2	\$/kg	2018	Conroy 2018 [36]
--------	---	-------	------	---------------------

Table 8 Piping costs

For the thermal energy storage system different cost values are found, as reported in Table 22. In this work NaCl-MgCl₂ is considered as storage media. For the supercritical CO₂ power block different costs are found for different cycle configurations and turbine inlet temperature (TIT), as shown in Table 23. The recompressed cycle configuration is used in this work. For the operation and maintenance (O&M) cost different values are found, expressed as fixed, variable, or as percentage of capital expenditure (CAPEX) (Table 24). For indirect cost the found values are reported in Table 25 divided by category. The main cost assumptions are reported together in Table 9.

Cost item	Value
Land purchase	2 \$/m ²
Heliostats and site improvements	140 \$/m ² _{heliostat}
Tower (steel lattice) H < 45 m	$\frac{H[m]}{1000}$ M\$
Tower (steel monopole) H > 45 m	$1.50227 - 0.00879597 \cdot H[m] + 0.000189709 \cdot H^2$ M\$
Receiver (1)	135 \$/kW _{th}
Receiver (2)	$52.0685 \cdot \frac{A_{rec} [m^2]}{560.77}$
Piping	See Table 8
TES (430-580 °C)	$(10.74 + 10.74 + 9.75) \cdot \left(\frac{V[m^3]}{15650}\right)^{0.8}$ M\$
TES (550-730 °C)	$(10.74 + 19.34 + 9.75) \cdot \left(\frac{V[m^3]}{15650}\right)^{0.8}$ M\$
Power block (TIT 550 °C)	2493 \$/kW _{el}
Power block (TIT 700 °C)	2543 \$/kW _{el}
O&M fixed	65 \$/kW _{el} /y
O&M variable	3.5 \$/MWh _{el}

Indirect costs	20% of CAPEX
Plant lifetime	30 y
Discount rate	8%

Table 9 Cost assumptions for the comparison of the plants

With the defined cost items and cost values the capital expenditure can be estimated for each subsystem: solar field, tower, receiver, piping, TES, and power block. The total capital expenditure can be evaluated as shown in Equation (53), as the sum of the cost of each subsystem.

$$CAPEX = Cost_{SF} + Cost_{tower} + Cost_{receiver} + Cost_{piping} + Cost_{TES} + Cost_{PB} \quad (53)$$

The levelized cost of heat (LCOH) and the levelized cost of electricity (LCOE) are computed with a simplified approach using a capital recovery factor CRF as shown in Equation (54) and Equation (55).

$$LCOH = CRF \cdot \frac{Cost_{SF} + Cost_{tower} + Cost_{receiver}}{Q_{HTF,year}} \quad (54)$$

$$LCOE = \frac{CRF \cdot (CAPEX + CAPEX_{indirect}) + O\&M_{fixed}}{AEP} + O\&M_{variable} \quad (55)$$

The capital recovery factor is evaluated using Equation (56), assuming a discount rate d equal to 8% and a plant lifetime L equal to 30 years.

$$CRF = \frac{d \cdot (1 + d)^L}{(1 + d)^L - 1} \quad (56)$$

3 Case Study

3.1. Overview

The case study for this work is initially based on Jemalong CSP pilot plant in Australia. This plant by Vast Solar is the only existing modular solar tower project in the world currently operating and it consists of five solar field modules and a $1.1 \text{ MW}_{\text{el}}$ power block. The present case study focuses on a 5 MW_{el} plant where the solar field layout and the receiver geometry are initially developed starting from Vast Solar $1.2 \text{ MW}_{\text{th}}$ modules. The operating temperatures, the storage system, and the power block are defined following different considerations and differ from the ones used in Vast Solar pilot plant.

The first part of the analysis (Section 3.3) investigates the optical performances of a cornfield module similar to the one used by Vast Solar and some variations in the heliostat disposition. A plant with 29 modules is then evaluated with two different operating temperatures and compared with the corresponding single field plant. The solar multiple and the TES size are then optimized as function of the LCOE for both the single field and the modular configurations, and the optimal number of modules is identified. In the next step the receiver size and tower height are changed with respect to the ones used at Jemalong pilot plant, and they are optimized as function of LCOH. Finally, SM and TES size are optimized again as function of LCOE. The diameter of the tubes of the receiver and the HTF speed in the piping system are always optimized as described in Section 2.3, Receiver, and Section 2.4, Piping.

In the second part (Section 3.4) to furtherly increase the modular plant performances module configurations different from the one used by Vast Solar are investigated: a rectangular shape module with radial layout of the heliostats, and a polar solar field with no shape limitations. From the obtained results it is decided to discard the cornfield module. A surrounded module layout is instead added for the next analysis. The module power rating is investigated to evaluate possible benefits of a different power scale: modules from 1 MW_{th} to $10 \text{ MW}_{\text{th}}$ are considered for each of the three different module layouts. The same parameters are always optimized as function of LCOH (tower height, receiver size) and LCOE (solar multiple, TES size). To summarize, in the conducted analysis the following parameters are investigated and optimized:

- Tower height

- Receiver size
- Operating temperature range
- Diameter of the receiver tubes
- HTF speed in the piping system
- Solar multiple (number of modules)
- TES size
- Module size
- Heliostat layout configuration

The working schemes of the two parts of the case study are reported in Figure 44.

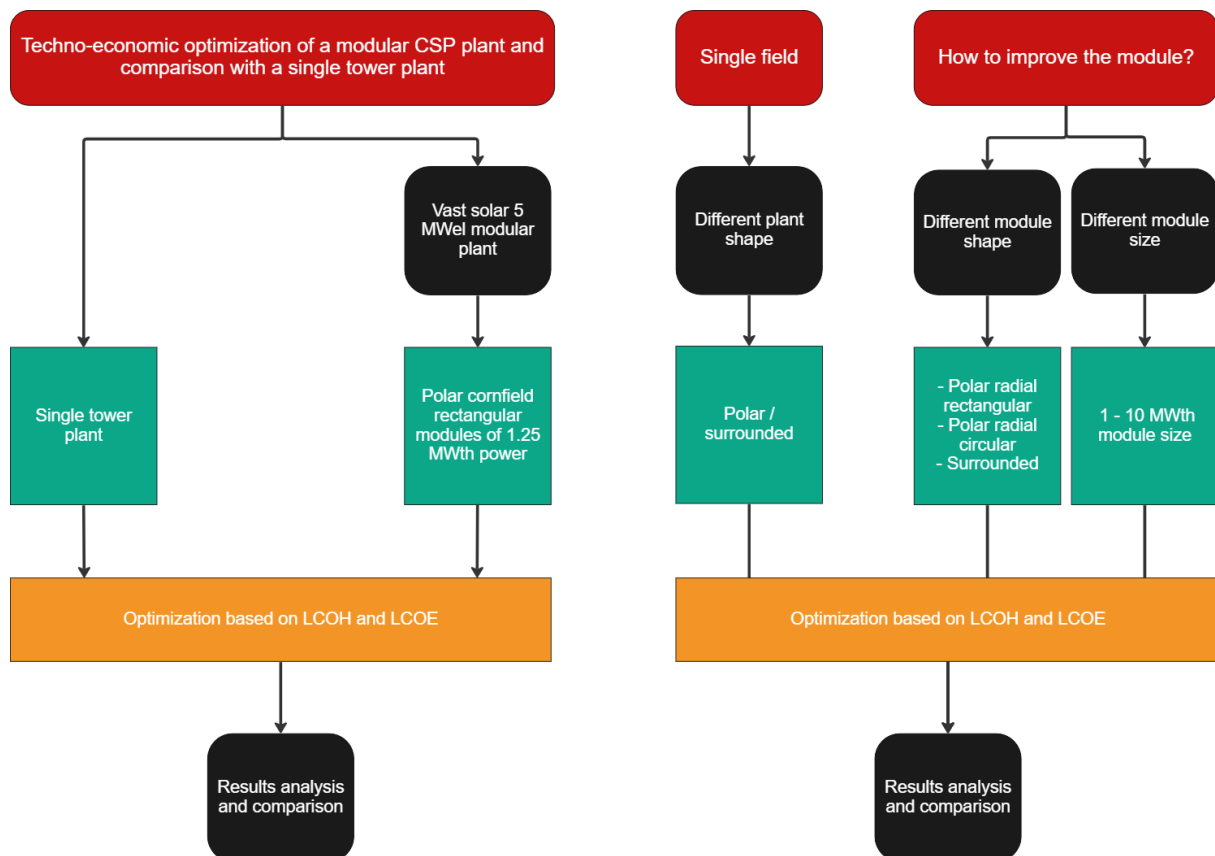


Figure 44 Work flow scheme of the first part of the case study (Section 3.3), on the left, and of the second part of the case study (Section 3.4), on the right

3.2. Jemalong pilot plant



Figure 45 Aerial picture of Jemalong power plant

Jemalong CSP modular plant consists of five identical modules, a HTF loop, a thermal storage system and a 1.1 MW_{el} power block, as showed in Figure 45. Each module comprises 700 heliostats of 3.6 m² of area, a tower of 27 m of height, and a 2.5 m² receiver. Liquid sodium is used as both heat transfer fluid and storage medium. The sodium thermal storage has a capacity of 3 hours and superheated steam is generated through a sodium to water heat exchanger. The turbine is a single-stage radial turbine with low efficiency, as the main purpose was to demonstrate the functionality of the CSP system. The heat sink is provided by an air-cooled condenser (Figure 46). Electrical energy was first sent to the grid via the West Jemalong sub-station in early 2017 and the plant completed commissioning in 2018.

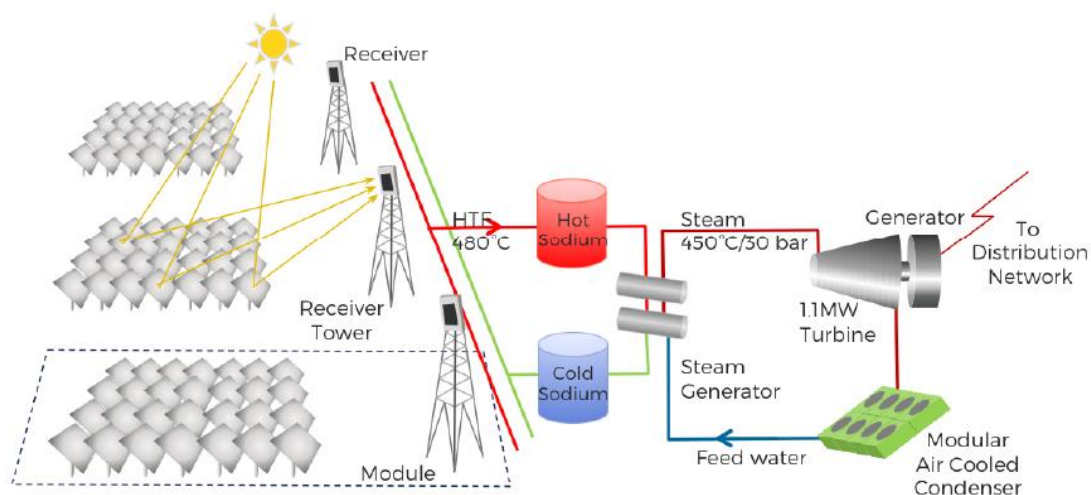


Figure 46 Jemalong plant scheme [37]

The Pilot Plant has met all three of its technical aims and objectives (multi-array control, steam generation and electricity production). The use of sodium necessitates the implementation of sophisticated safety systems and operational procedures.

Extensive operational experience at the pilot plant has proven the feasibility of the system, in particular with respect to vessel design, pump requirements, sodium purification, sodium handling and safe management in the event of a leak [38].

Vast Solar's modular, polar solar array provides a 17% improvement in coefficient of performance (a measure of the geometric efficiency of the solar array incorporating cosine, block and shading, etc.), delivering more energy per square meter of reflector than an equivalent single tower CSP plant. The higher efficiency solar array provides lower capital cost, lower operating costs, more mutual wind shielding, reduced glint and glare risks for aviation and neighboring properties [38].

The modular array design also enables localized control with smaller thermal inertia which generates faster, more precise responses than single receiver designs. Vast Solar's HTF flow is actively controlled with a high degree of accuracy by optical instrumentation for each receiver to provide a direct quantitative measurement of the radiation flux. This measured flux actively controls the HTF flow to provide the highest possible constant receiver outlet temperature which maximizes the exergy in the system and achieves the highest possible thermodynamic efficiency. Figure 47 shows data from operational tests whereby the plant is staged through different temperature control setpoints and despite significant solar transients the temperatures are adequately maintained. The system is extremely responsive to both planned (as can be seen by the orange line quickly converging with the blue line after each set point change) and unplanned changes such as transients, as can be seen by the insignificant change in outlet temperature when cloud transients reduce incident flux by 30 to 40% at 9:50am and 10:35am. Furthermore, the reduced temperature ramp rates are mixed in the network and are all but eliminated by the time they reach the power block [38].

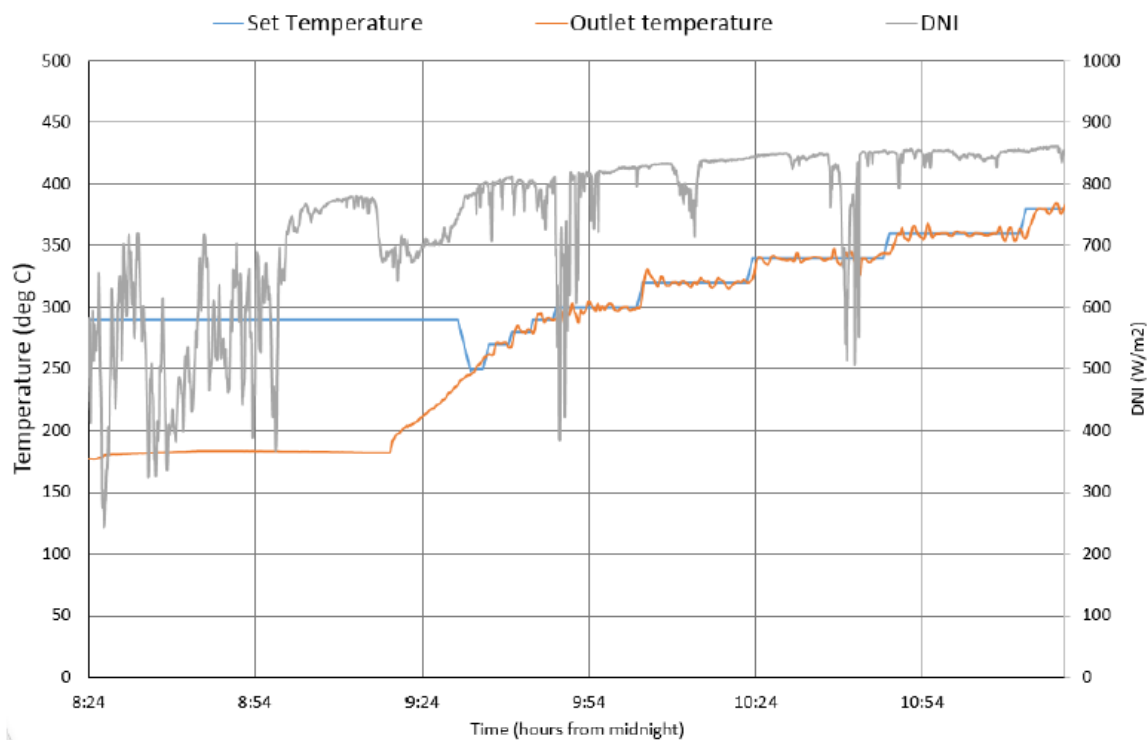


Figure 47 Time series of transient DNI and receiver outlet temperature, 13 May 2019 [38]

3.3. Part I - Cornfield module

Starting from the promising results claimed by Vast Solar the first considered solar field is modelled using SolarPILOT (Section 2.2) to represent as accurately as possible the solar field used at the Jemalong power station. The modelled solar field consists of 619 heliostats placed using a cornfield layout where the rows are progressively more distanced one from the other as the distance from the tower increases. This layout is compared with other two alternative layouts with no increased distance between rows: one with the same number of heliostats, and one with the same area (Figure 48). In all the configurations squared heliostats of 3.6 m^2 of area are considered. The same tower height of 27 m and receiver size of $0.9 \times 0.9 \text{ m}$ is used for the three layouts. In the whole case study, the location considered for the plant is Jemalong, Australia, and the considered design point is summer solstice (21st of December at noon in the austral hemisphere) with a DNI of 1000 W/m^2 .

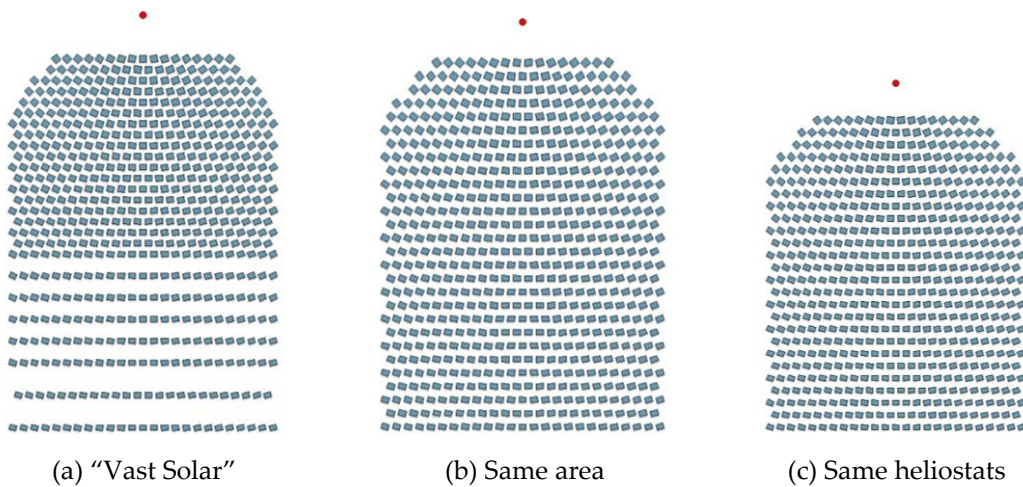


Figure 48 Alternative solar field layouts considered

The three layout configurations are evaluated from the optical performances point of view and from an economic perspective assuming the cost reported in Table 9. The "Vast Solar" module layout shows considerably higher annual optical performances with respect to the other two layout configurations and is therefore selected for the next step of the case study.

In the next step a whole plant is designed and studied. The plant is based on a 5 MW_{el} recompressed sCO₂ power block. As discussed in Section 1.3 the closed loop sCO₂ cycle offers the potential of higher cycle efficiency versus superheated or supercritical steam cycles at temperatures relevant for CSP applications. Brayton-cycle systems using sCO₂ have a smaller weight and volume, lower thermal mass, and less complex power blocks versus Rankine cycles due to the higher density of the fluid and simpler cycle design. The simpler machinery and compact size of the sCO₂ process may also reduce the installation, maintenance, and operation cost of the system. For these reasons the sCO₂ cycle technology is the leading candidate for the future of CSP power cycles and it is selected for the power block of this case study.

Liquid sodium is employed as heat transfer fluid. Vast Solar technology has proven the feasibility of modular CSP tower systems using liquid sodium HTF. This allows to significantly increase the operating temperature of CSP systems to more than 700 °C and replace the steam Rankine cycle with the high efficiency supercritical CO₂ Brayton cycle [39]. Sodium has been considered as a working fluid for tubular receivers since the very early days of CSP. Its performance benefits in comparison to other working fluids have been clearly established, both via generalised figures of merit as well as hydrodynamic receiver models. The main advantages of liquid sodium are: low melting point (97.5 °C) and high boiling point (883 °C), leading to a wide range of operating temperatures and reduced freezing risks, high heat capacity (1.27 kJ/kg at 500 °C) and high thermal conductivity (68.8 W/m K at 500 °C), leading to very high heat transfer rates, low density (845 kg/m³ at 500 °C), low cost (2–3.5 \$/kg) and good

compatibility with structural alloys at elevated temperatures [34]. Sodium can be a dangerous substance as it reacts exothermically with oxygen and can cause explosions in presence of water. Despite the potential risks, a range of safety measures and equipment can be applied to achieve very stringent control of oxygen content in the fluid, exclude water from the installations and minimise materials corrosion and interaction [40].

The use of sodium as HTF allows higher maximum flux density on the receiver surface with respect to solar salts. With the selected Haynes230 alloy and a maximum HTF operating temperature of 730 °C the allowed maximum flux is considered around 1.9 MW/m² [41]. To exploit this characteristic of sodium-based receivers the maximum flux density is pushed close to this threshold during the receiver design, obtaining a smaller receiver (0.9 x 0.9 m) with respect to the one used at the Jemalong power station (1.6 x 1.6 m). The aspect ratio of the receiver (ratio between receiver height and width) is kept equal to 1 and the receiver is considered oriented with a 20° angle downward towards the solar field, as in the case of Vast Solar receiver. The modelled “Vast Solar” module, in summary, keeps the solar field layout method, the tower height, and the receiver orientation and aspect ratio of the original Vast Solar module, but has a different number of heliostats and a different receiver size.

The first analysed configuration consists of 29 “Vast Solar” modules. At the design point each module delivers 1.25 MW_{th} to the receiver, which in turn corresponds to a solar multiple equal to 2.6. The piping system connects each module to the storage tanks: an indirect storage system using molten salts as storage media is preferred to a direct liquid sodium storage system due to the safety risks associated to liquid sodium tanks and the high related cost [42]. Nevertheless, advanced molten salts are required to meet the temperature necessary to operate the sCO₂ cycle, therefore molten salts based on NaCl (48% mol) and MgCl₂ (52% mol) are selected as storage media [43]. Two systems with different operating temperature ranges are initially investigated: a system with a turbine inlet temperature (TIT) of 550 °C and a design cycle efficiency of 37.5%, and a system with a TIT of 700 °C and design cycle efficiency of 44%. In the first case the storage tanks and the receivers operate in the temperature range 430-580 °C to account for the heat exchangers between piping, TES, and power block, while in the second case they operate in the range 550-730 °C. The thermal storage size is assumed equal to 11 h. These two modular systems are compared from a techno-economic perspective with their corresponding single tower system designed with the same solar multiple and TES size. For the single field plant squared heliostats of 25 m² are used and a tower height of 75 m is selected. The main cost assumptions are reported in Table 9.

In the next step the solar multiple and the TES size of the modular and single field plants for both ranges of temperature are optimized. In the case of the modular systems the solar multiple is adjusted by changing the number of modules in the system and evaluating the piping performances. In the case of the single field systems

the solar multiple is changed by modelling solar fields of different sizes in SolarPILOT, keeping the same tower height and heliostat size, and adjusting the receiver size to achieve the maximum allowed flux on the receiver surface. The results of this first analysis are discussed in detail in Section 4.1 and show that the systems with higher TIT and cycle efficiency provide lower LCOE. The systems operating in the range 430-580 °C show higher LCOE, mainly due to the significantly lower power block efficiency, and therefore only the 550-730 °C systems are further investigated.

The next step in the case study consists in the optimization of two additional parameters regarding the solar field geometry: the tower height and the receiver size. The solar field geometry is optimized both for the modular and single field systems by evaluating the LCOH for different tower heights and receiver sizes. This means that for each different combination of the two parameter the field is modelled in SolarPILOT, and its optical performances are assessed. By doing so the obtained modules only keep the cornfield layout form the original Vast Solar module, while tower height and receiver size are changed. Then the receiver model provides the thermal evaluation of the receiver efficiency and the annual heat absorbed by the HTF in the receiver is computed. This allows the computation of the LCOH for each configuration. The cost assumptions are the same as in the first part, as reported in Table 9, except for the receiver cost where the correlation as function of the receiver area is used.

With the defined optimal tower height and receiver size the solar multiple and TES size are again optimized computing the LCOE. In the case of the single field system the tower height and receiver size are optimized assuming the optimal solar multiple from the values obtained from the previous analysis and then optimizing only the TES size. It is important to remind that also the receiver tube diameter and the HTF speed in the piping system are always optimized in each considered configuration.

With the obtained results the best modular configuration and the best single field configuration are identified. The results show that the single field system reaches lower LCOE with respect to the modular system. This aspect and the other results are the base for the next part of the work, where the module shape and size are changed to try to improve the performances and reduce the costs, to better exploit the possibilities of modular configurations and make them more competitive with respect to their single field counterparts.

3.4. Part II - Module optimization

In this second part of the case study the cornfield solar field layout, based on the one used at Jemalong power plant and optimized in the previous section, is compared with other possible module layouts, as shown in Figure 49. The radial rectangular configuration is defined keeping the same occupied area as the cornfield layout, while the radial circular configuration is defined keeping the same power delivered to the

receiver ($1.5 \text{ MW}_{\text{th}}$). For each new layout the tower height and the receiver size are optimized computing the LCOH.

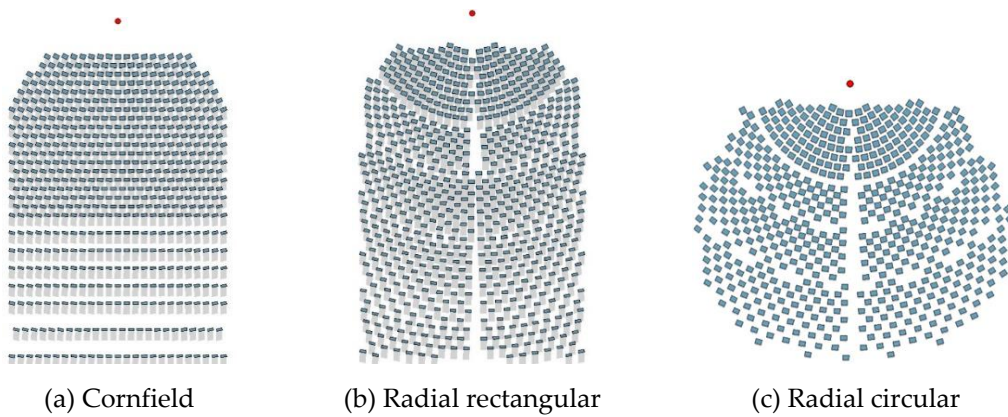


Figure 49 Layout configurations initially considered

The results, discussed in detail in Section 4.2, show that both the radial rectangular and the radial circular layout perform better than the cornfield layout, reaching lower LCOH. For this reason, the cornfield layout is discarded and substituted with a surrounded field layout to proceed with the case study, as shown in Figure 50.

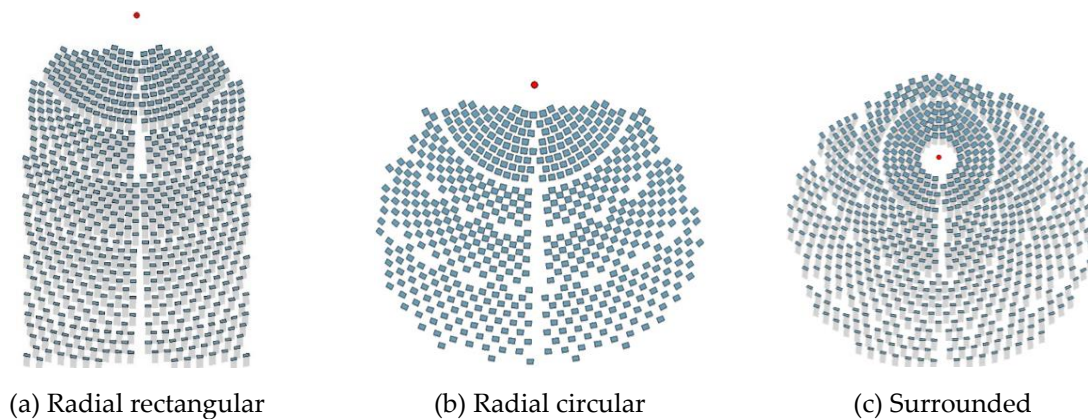


Figure 50 Layout configurations considered after the cornfield layout is discarded

To further improve the modular plant performances the size of the modules is investigated. For each one of the three layout the power delivered to the receiver is varied from 1 MW_{th} to $10 \text{ MW}_{\text{th}}$ with a step increase of 1 MW_{th} . The radial rectangular solar field for each power rating is obtained by scaling accordingly the rectangular field boundaries until the necessary power is reached. For each layout and rated power, the tower height and the receiver size are optimized computing the LCOH. The tower height is varied with intervals of 4 m, while the receiver height/width is varied with intervals of 0.25 m^2 . The heliostat size is not a parameter of optimization: it is assumed linearly increasing from 3.6 m^2 for the 1 MW_{th} modules to 12.5 m^2 for the $10 \text{ MW}_{\text{th}}$ modules. The optimization of the heliostat size would increase unnecessarily the complexity of the analysis. It would introduce for each module power and layout, and

for each tower height and receiver size an additional degree of freedom to the design of the system, requiring for each combination the modelling of different heliostat sizes in SolarPILOT and their performance assessment. The same considerations are applied to the receiver aspect ratio that is therefore kept equal to 1.

When the best solar module geometry is identified for each combination of layout and size the solar multiple and the TES size are optimized computing the LCOE. The maximum allowed number of modules is fixed at 50, to avoid an excessively extended piping network. This procedure provides for each combination the best modular plant. These plants are compared with two single field plant: a polar field plant, as in the first part of the case study, and a surrounded field plant. The results and the related considerations are discussed in detail in the next chapter (Chapter 4).

4 Results

4.1. Part I – Cornfield module

As discussed in Section 3.3 the “Vast Solar” module, with rows progressively more distanced one from the other, is initially compared with two other solar field layouts. The three configurations have the same tower height and receiver size, but different heliostat disposition and number. The results reported in Table 10 show that the “Vast Solar” layout has better blocking efficiency than the other two options, leading to an overall higher optical efficiency at design conditions. This allows the module with the distanced rows to deliver the same power but at lower cost with respect to the module with the same area, and more power at almost the same cost with respect to the module with the same number of heliostats. Although the differences among the three layouts are very small the “Vast Solar” configuration is selected as the best option and is used in the next step of the analysis.

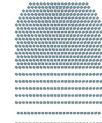

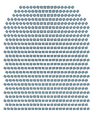
Layout	 “Vast Solar”	 Same area	 Same heliostats
Number of heliostats	618	666	618
Design blocking efficiency	0.95	0.90	0.91
Design image intercept efficiency	0.76	0.75	0.77
Design optical efficiency	0.58	0.54	0.56
Design power incident on the receiver	1.26 MW _{th}	1.26 MW _{th}	1.20 MW _{th}
Solar field cost	334 k\$	359 k\$	332 k\$

Table 10 Considered heliostat layouts and their design optical performances

Using the selected module layout two different plants, operating at different temperature ranges, are investigated, as described in Section 3.3. One plant operates in the range 430-580 °C (TIT 550°C and power block efficiency 0.375) while the other in range 550-730 °C (TIT 700 °C and power block efficiency 0.44). For the single tower plant design squared heliostats of 5x5 m are used and the receiver is designed by reaching the maximum flux allowed on the receiver surface, thus leading to a rather small receiver. In the case 430-580 °C it is obtained a receiver size of 5.1 x 5.1 m while in the case 550-730 °C the receiver is 4.85 x 4.85 m. The tower height is assumed equal

to 75 m. In all the configurations considered the diameter of the receiver tubes is optimized as described in Section 2.3 and the HTF speed in the piping system is optimized as described in Section 2.4. The solar multiple is optimized by changing the number of modules in the case of the modular configurations, and by changing the field size in the case of the single field configurations. In Figure 51 the results for the case 430-580°C are reported. The identified optimal modular configuration presents solar multiple equal to 3.4, which corresponds to 43 modules, and TES size of 14 hours. The optimal single field configuration presents solar multiple equal to 2.75, and TES size of 12 h.

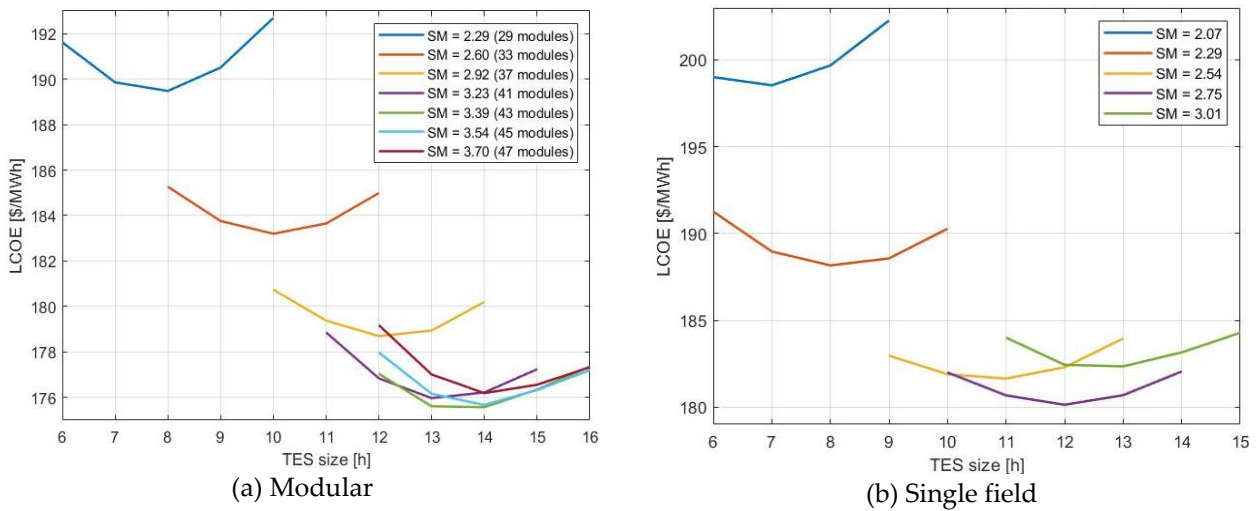


Figure 51 Solar multiple and TES size optimization as function of LCOE for the temperature range 430-580 °C

In Figure 52 the results for the case 550-730 °C are reported. The identified optimal modular configuration presents solar multiple equal to 3.5, which corresponds to 39 modules, and TES size of 14 hours. The optimal single field configuration presents solar multiple equal to 2.85, and TES size of 13 h.

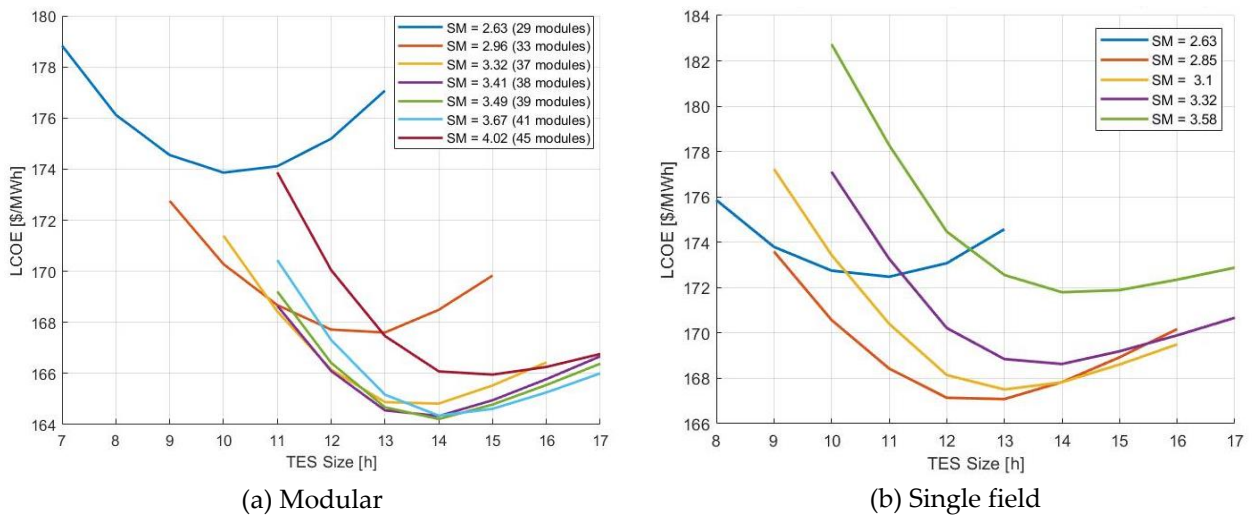


Figure 52 Solar multiple and TES size optimization as function of LCOE for the temperature range 550-730 °C

The lower optimal solar multiple for the single field configurations is due to the increasing size of the solar field as the SM increases. This leads to progressively lower annual optical efficiency and higher costs (more heliostats, bigger receiver) as shown in Figure 53. On the other hand, for the modular configuration the increase of solar multiple only leads to a slight decrease of the annual piping performances, as more modules are added, while the annual optical and thermal performances remain unchanged, and the overall solar to electric efficiency remains almost constant. The lower optimal solar multiple for the single field configurations leads to lower optimal TES size, as less excess of thermal power is available for the storage. The same considerations are valid for both ranges of temperatures.

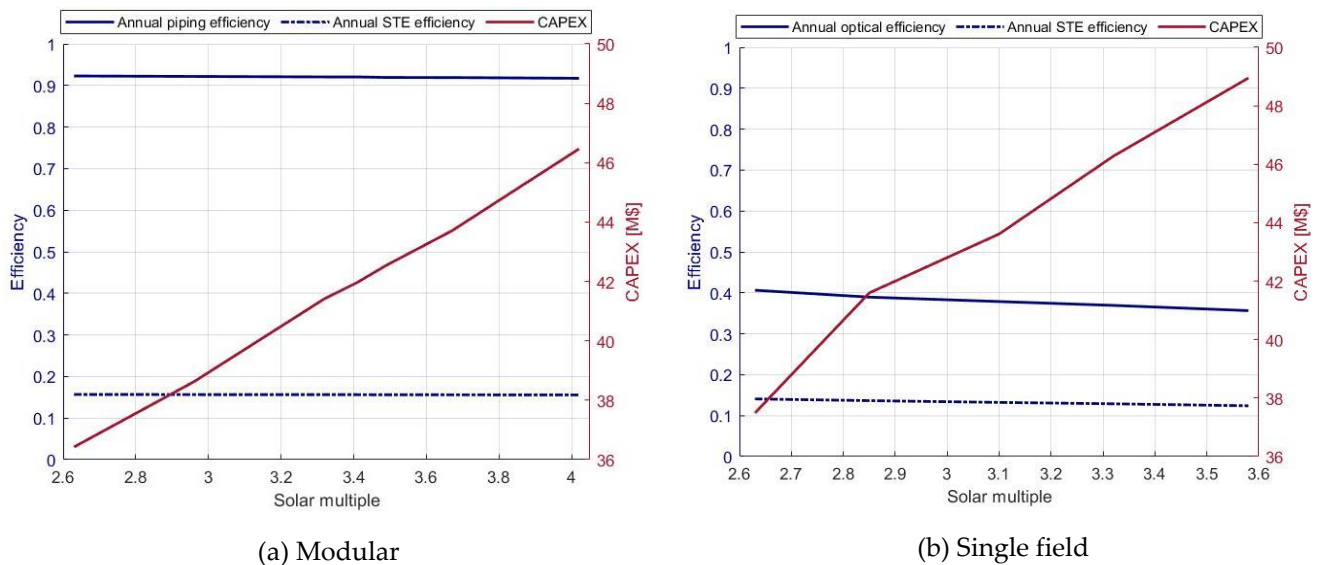


Figure 53 Annual efficiencies and investment cost as function of solar multiple for plants in the temperature range 550-730°C at optimal TES size

The four identified optimal configurations (modular and single field for two temperature ranges) are analysed in detail. In Table 11 and Table 12 the main characteristics of the plants at design conditions in the two ranges of temperature are reported. The higher solar multiple for the modular configurations is reached with lower heliostat surface with respect to the single field systems. The bigger dimension of the receiver of the single field systems leads to much higher pressure drops with respect to the small receiver of the modular configurations. On the other hand, the pressure drops due to the piping system in the modular systems are significantly higher with respect to the single field configurations, where the piping system only connects the only tower to the storage system. The overall effect is that the total pressure drops are higher in the single field configurations (Table 11).

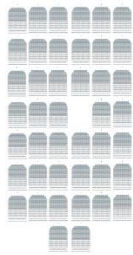
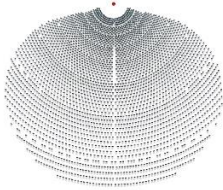
Temperature range 430-580 °C		
Parameters and geometry		
Number of modules	43	-
Heliostat size	3.6 m ²	25 m ²
Total reflective area	93 000 m ²	97 000 m ²
Tower height	27 m	75 m
Receiver size	0.9 x 0.9 m	5.1 x 5.1 m
Receiver tubes – diameter (Optimized)	13.7 mm	21.3 mm
HTF speed piping (Optimized)	1.5 m/s	1.5 m/s
HTF mass flow rate	273 kg/s	212 kg/s
Receiver pressure drop	0.2 bar	3.4 bar
Piping system maximum pressure drop	2.6 bar	0.1 bar
Total pressure drops	2.8 bar	3.5 bar
Solar multiple (Optimized)	3.4	2.75
TES size (Optimized)	14 h	12 h

Table 11 Main parameters of the modular and single field plants operating in the temperature range 430-580 °C

The plants operating in the temperature range 550-730°C benefit from a significantly higher power block efficiency. This leads to less heliostats necessary to deliver the desired power and so to slightly higher optimal solar multiples. The higher temperatures are accompanied by a smaller optimal diameter and higher pressure losses for the receiver of the single field plant. The higher temperatures of the HTF also lead to higher optimal HTF speed and higher pressure losses in the piping system (Table 12).

Temperature range 550-730 °C

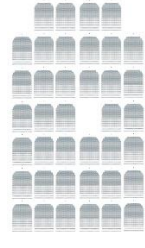
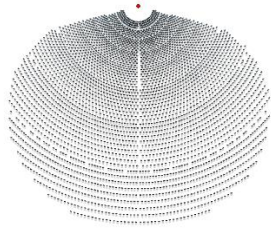
Parameters and geometry		
Number of modules	39	-
Heliostat size	3.6 m ²	25 m ²
Total reflective area	84 000 m ²	89 000 m ²
Tower height	27 m	75 m
Receiver size	0.9 x 0.9 m	4.85 x 4.85 m
Receiver tubes – diameter (Optimized)	13.7 mm	17.1 mm
HTF speed piping (Optimized)	1.6 m/s	1.6 m/s
HTF mass flow rate	188 kg/s	148 kg/s
Receiver pressure drop	0.2 bar	4.8 bar
Piping system maximum pressure drop	3.4 bar	0.1 bar
Total pressure drops	3.6 bar	4.9 bar
Solar multiple (Optimized)	3.50	2.85
TES size (Optimized)	14 h	13 h

Table 12 Main parameters of the modular and single field plants operating in the temperature range 550-730 °C

The optimal diameter for the tube of the receivers is determined as discussed in Section 2.3. As shown in Figure 54 pressure drops in the receiver decrease as the tube diameter increases, while thermal losses increase and the power absorbed by the heat transfer fluid reduces. The effect of pressure drops is particularly relevant for the receiver of the single field configurations, leading to bigger optimal diameters.

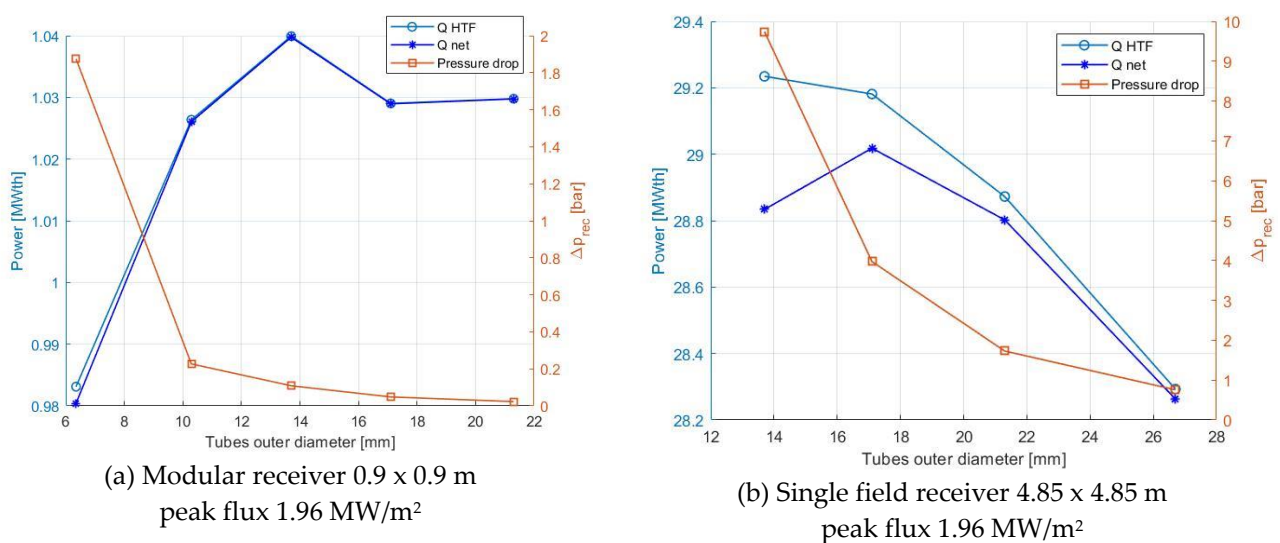


Figure 54 Optimization of the diameter of the receiver tubes operating in the temperature range 550-730°C

The design powers and performances of the four optimal configurations are showed in Figure 55. The higher heliostat area of the single field configuration provides higher power incident on the solar field. This is balanced, at design conditions, by a significantly lower optical efficiency with respect to the modular systems, which reduces the power incident on the receiver surface. The high flux on the receiver leads to good thermal efficiency for all the configurations, with the systems operating at higher temperature showing slightly less efficiency due to increased thermal losses. The piping thermal efficiency in the case of single field systems is almost equal to 1 with almost null thermal losses. In the case of modular configurations instead, thermal losses in the piping system become relevant, but there is no significant difference in performances between the 430-580°C and the 550-730°C systems as the insulant layers are designed accordingly.

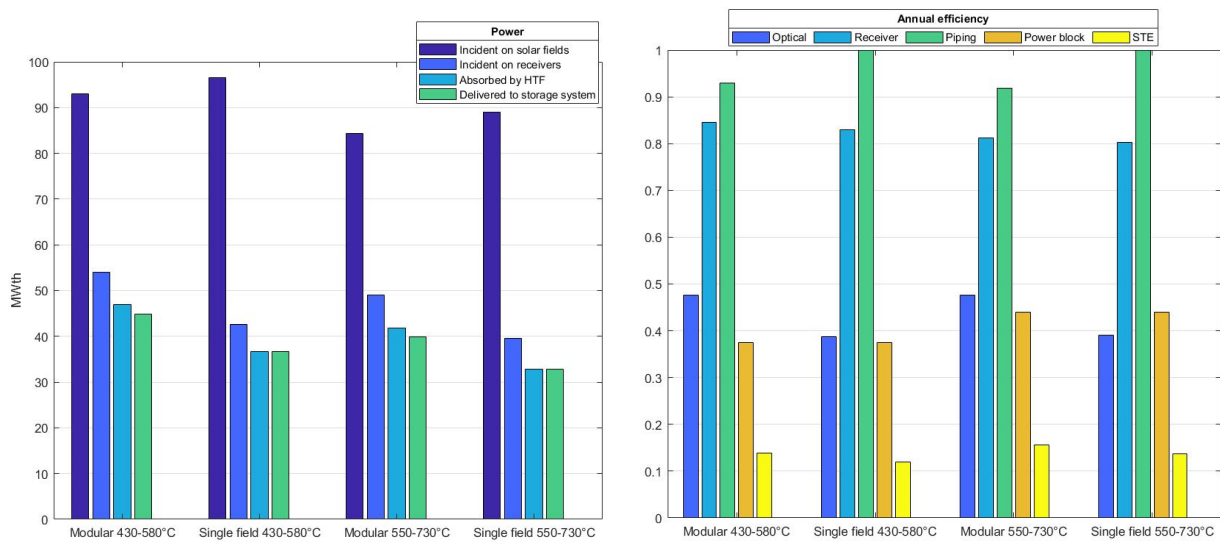


Figure 55 Design powers and efficiencies of the four optimal configurations

The off-design performances of the investigated optimal configurations significantly affect the annual energy production. The modular configurations are more affected by the decrease of the performances in off design conditions with respect to the single field configurations, as shown in Figure 56. Optical efficiency reduces around 10%, from ~58% at design conditions to ~48% for the annual evaluation, for the modular systems. On the other hand, for the single field systems this reduction is around 5%. This aspect, combined with the higher heliostat area of the single field reduces the difference in the annual energy incident on the receiver between modular and single field configurations. The piping efficiency for the modular systems reduces around 3%, from ~96% at the design point to ~93% for the annual evaluation. On the other hand, the piping efficiency for the single field systems remains around 1. For these reasons the annual solar to electric efficiencies of modular configurations (13.8% and 15.6%) are closer to the annual solar to electric efficiencies of single field configurations (12% and 13.7%) with respect to the design solar to electric efficiency values.

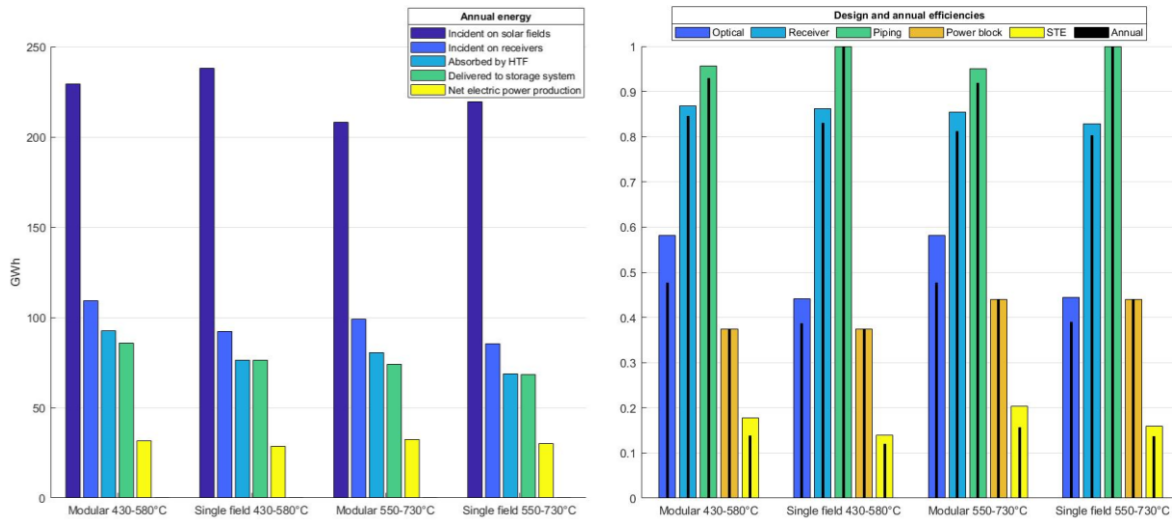


Figure 56 Annual energy and efficiencies of the four optimal configurations

The reason behind the relevant decrease of optical efficiency in off design conditions for the modular systems can be seen in the map of the optical efficiency of the module as function of azimuth and zenith angles. When the solar azimuth is close to $-100^{\circ}/+100^{\circ}$ and the zenith angle is sufficiently low the optical efficiency decreases significantly. This is due to the cornfield disposition of the heliostats: around these values of azimuth and zenith angles the squared heliostats are aligned along the direction of their shadows thus reducing the shading efficiency (Figure 57). The peak of this effect is around 100° and not around 90° because of the squared shape of the heliostats and their orientation. At 90° the heliostats are oriented more diagonally then at 100° and therefore project less shadow on the adjacent heliostats.

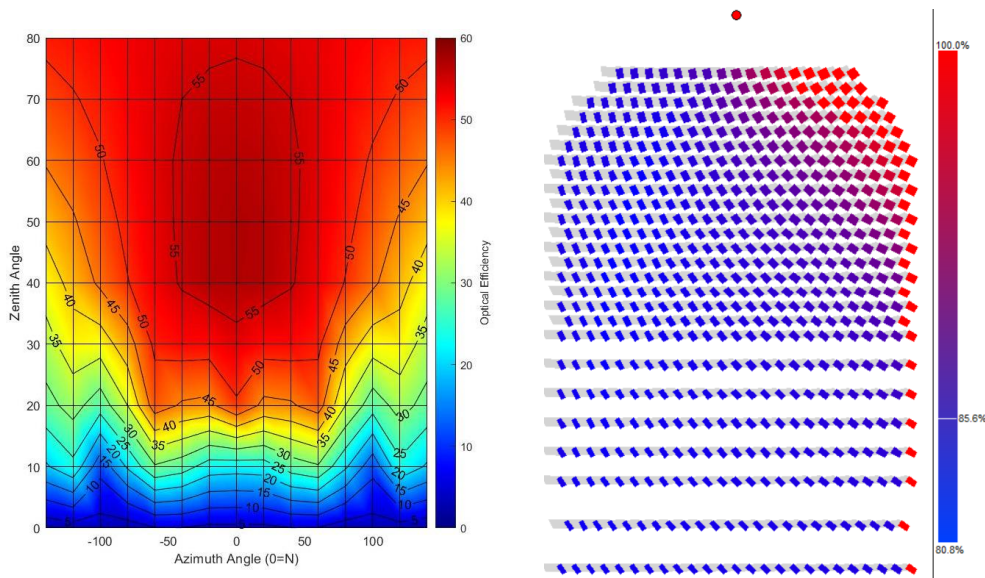


Figure 57 Optical efficiency map of modular field and shading efficiency for zenith angle equal to 15° and azimuth angle equal to 100°

The receiver and piping efficiencies in off design conditions for the temperature range $550-730^{\circ}\text{C}$ are represented in Figure 58. The smaller receiver of the modular plants

achieves slightly higher efficiency values with respect to the bigger single field receiver. The modular plant receiver efficiency is more affected by off design operation, especially in the region for thermal power input from 50% to 100% of the design value. The piping thermal efficiency in the case of the single field configuration is essentially constant and close to 1, as previously commented. The piping thermal efficiency of the modular system is significantly affected by a reduction of power input in the receiver as the mass flow rate is adjusted to keep the same inlet and outlet temperatures.

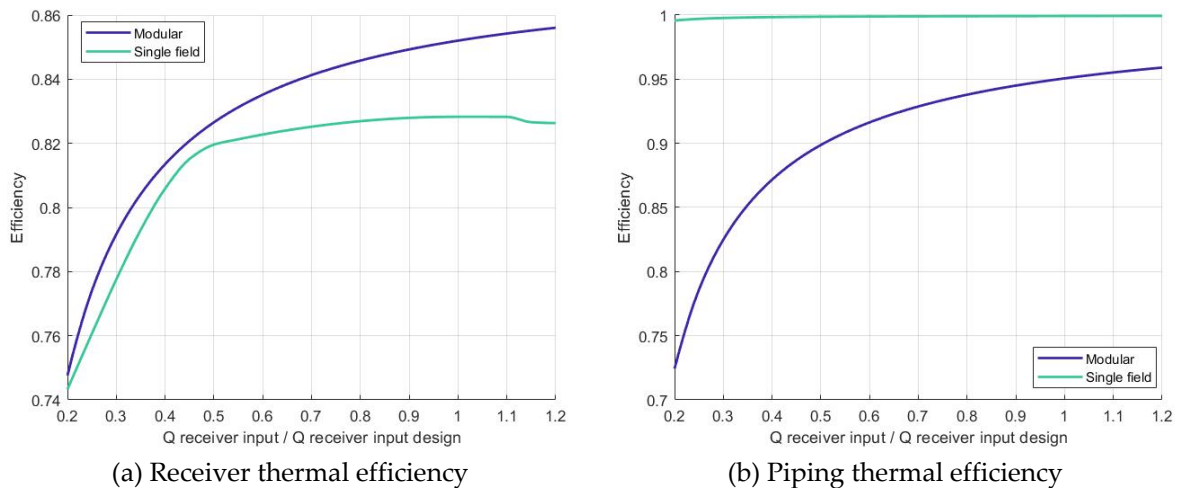


Figure 58 Receiver and piping off design efficiencies for the plants operating in the temperature range 550-730°C

The investment costs of the four optimal configurations are reported in Figure 59. The cost of heliostats and site improvement is one of the main cost items, representing around 30% of total costs. It is lower for the modular configurations as they need less reflective area to deliver the same power at design conditions. Although the receivers used in the modular systems are significantly smaller with respect to the single field receiver, a high number of receivers is required thus increasing the overall cost. On the other hand, the much more economical steel lattice towers used in the modular systems allow to reduce the cost with respect to the single steel monopole tower used in the single field systems. The piping cost is almost negligible in the single field configurations. In the modular cases it remains a small percentage of total costs, around 2-3%. The TES system and the power block account together for ~50% of the total costs. The TES cost is higher for the modular configurations due to the higher optimal thermal storage size. The difference between the cost of the power block operating in the temperature range 430-580°C, with design efficiency of 0.375, and the cost of the power block operating in the temperature range 550-730°C, with design efficiency of 0.44, is almost negligible. The systems operating in the higher temperature range present overall lower investment cost. The modular configurations show higher total investment costs with respect to their single field counterparts, mainly because of the cost of the receivers.

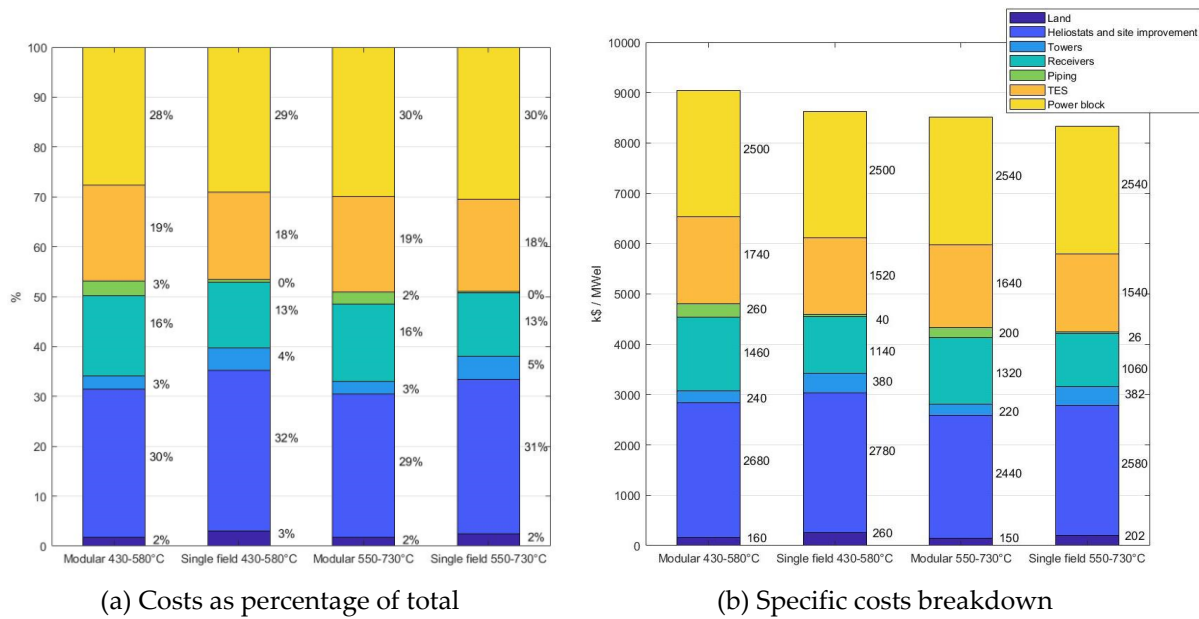


Figure 59 Investment costs of the four optimal configurations

The most important performance and economic parameters of the four optimal configurations are reported in Table 13. The difference in annual energy production and total investment costs between modular and single field configurations are very small. This results in very similar values of LCOE. Nevertheless, the modular plants are able to achieve slightly lower LCOE and higher capacity factor with respect to the single field plants. The systems operating in the temperature range 550-730°C provide better performances at lower cost reaching ~7% lower LCOE with respect to the systems operating at lower temperatures. For this reason, the 430-580°C case is not furtherly investigated and from this point on only the 550-730°C case is considered.

	Modular 430-580°C	Single field 430-580°C	Modular 550-730°C	Single field 550-730°C
AEP [GWh]	29.9	27.9	30.2	29.5
CAPEX _{tot} [M\$]	54.3	51.8	51.1	49.9
LCOE [\$/MWh]	176	180	164	167
CF	68 %	64 %	69 %	67 %

Table 13 Performance and economic parameters of the four optimal configurations

To try to improve the performances of the modular system the tower height and receiver size are optimized as function of LCOH. As mentioned in Section 3.3 the cost correlation used for the receiver is changed: a cost correlation as function of the receiver area is used instead of one depending on the receiver thermal input. Increasing the receiver size the annual optical efficiency of the solar field increases, while the annual thermal efficiency of the receiver decreases (Figure 60). Higher towers lead to better annual optical efficiency while the annual thermal efficiency remains almost unchanged. At the same time increasing the tower height and the receiver size implies higher investment costs. The trade-off among these effects leads to an optimal tower height of 34 m and an optimal receiver size of 1.5 m². With the

identified optimal module geometry, the solar multiple and TES size of the plant are again optimized. The optimal values obtained are solar multiple equal to 3.7, which corresponds to 34 modules, and TES size of 15 h.

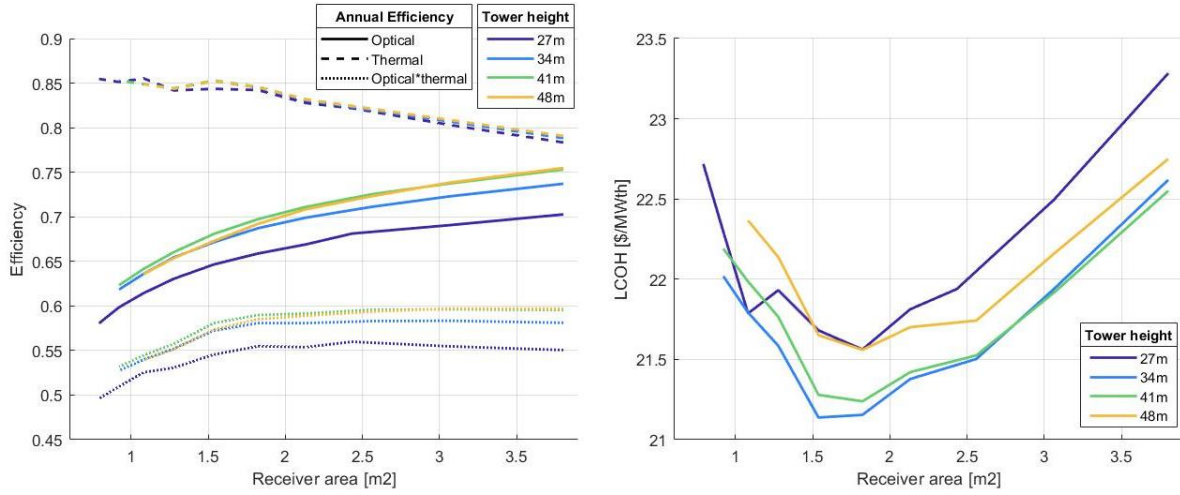


Figure 60 Module optical efficiency, thermal efficiency and LCOH as function of receiver size and tower height

For the single field plant the tower height and the receiver are also optimized as function of LCOH. In this case the optimal solar multiple is assumed equal to 3 based on the previously conducted analysis. The results are reported in Figure 61. The same trends of annual efficiency of the modular system can be observed as function of receiver area and tower height. The lower limit for the receiver area is defined by the maximum allowed flux on the receiver surface. The optimal values obtained are tower height equal to 100 m and receiver area of 25 m².

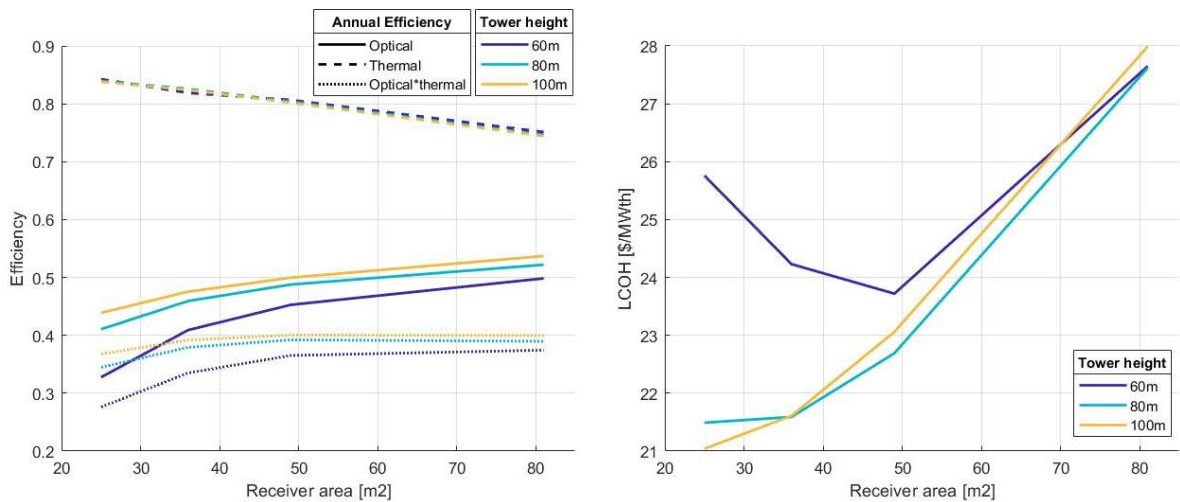


Figure 61 Single field optical efficiency, thermal efficiency and LCOH as function of receiver size and tower height

The main parameters and performance indicators of the optimal configurations are reported in Table 14. The modular configuration provides a slightly higher annual

energy production with respect to the single field configuration. Nevertheless, the higher investment cost of the modular systems provides a final LCOE which is very close to the LCOE of the single field system. The optimization of tower height and receiver size provides a 7 % reduction of the LCOE for the modular configuration, while it provides a 9 % reduction for the single field configuration.

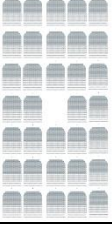
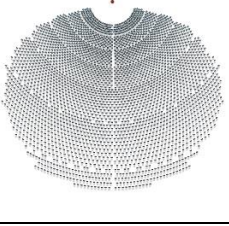
		
Number of modules	34	-
Tower height (Optimized)	34 m	100 m
Receiver size (Optimized)	1.25 x 1.25 m	5 x 5 m
Solar multiple (Optimized)	3.7	3.0
TES size (Optimized)	15 h	13 h
Design power incident on receiver	1.5 MW _{th}	40 MW _{th}
Annual STE efficiency	17.1 %	15.4 %
AEP	31.0 GWh	29.2 GWh
CAPEX _{tot}	48.7 M\$	45.1 M\$
LCOE	153 \$/MWh	152 \$/MWh
CF	71 %	67 %

Table 14 Main parameters and performance indicators of the two optimal configurations

The costs breakdown and the design and annual efficiencies of the two configurations are reported in Figure 62. The optimization of tower height and receiver size leads to an improvement of 16 % of the annual optical efficiency for the modular plant, and of 11 % for the single field plant. The overall solar to electric efficiency increases from 15.6 % to 17.1 % for the modular system, while it increases from 13.7 % to 15.4 % for the single field system. The higher flux on the receiver of the single field provides higher thermal efficiency with respect to the modular receiver. The change in the used cost correlation for the receiver reduces the cost associated with this component, in particular for the single field receiver.

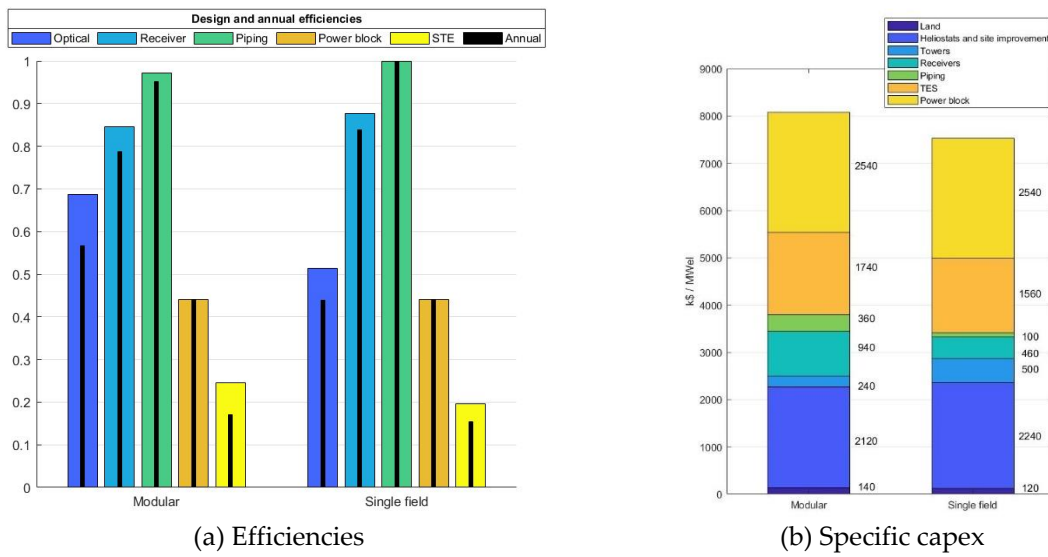


Figure 62 Design and annual efficiencies and specific capex of the two optimal configurations

The discussed results show that the modular configuration can be competitive with its single field counterpart thanks to better performances but also at higher cost. To furtherly investigate the possible advantages of the modularity of CSP plants two aspects are considered. The cornfield configuration seems to limit the off-design optical efficiency of the modular solar field; for this reason, alternative heliostat layouts are investigated. The small power size of the module (1.5 MW_{th} incident on the receiver) leads to a high optimal number of modules increasing the costs, for this reason different module sizes are investigated.

4.2. Part II – Module optimization

Three solar field layouts are investigated, as discussed in Section 3.4. For each layout, tower height and receiver size are optimized as function of LCOH. The results for the three optimal configurations are reported in Table 15. The radial circular layout shows the highest annual optical efficiency and produces the same annual thermal energy as the cornfield layout, with a lower number of heliostats. This results in the lowest value of LCOH. In the radial rectangular configuration, the heliostat placement allows to reach better optical efficiency with respect to the cornfield layout, resulting in a lower LCOH.


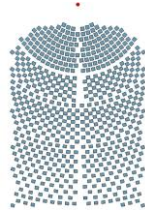
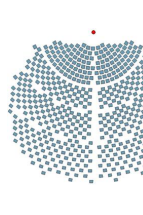
	Cornfield	Radial rectangular	Radial circular
Layout			
Number of heliostats	618	625	589
Tower height (Optimized)	34 m	34 m	27 m
Receiver size (Optimized)	1.25 x 1.25 m	1.25 x 1.25 m	1.25 x 1.25 m
Design power incident on receiver	1.5 MW _{th}	1.5 MW _{th}	1.5 MW _{th}
Annual optical efficiency	56.7 %	57.0 %	59.7 %
Annual thermal efficiency	78.4 %	78.7 %	78.5 %
Annual heat production	2.37 GWh	2.42 GWh	2.39 GWh
CAPEX	566 k\$	558 k\$	543 \$
LCOH	21.2 \$/MWh	20.4 \$/MWh	20.3 \$/MWh

Table 15 Results of different optimized solar field layouts

The optical efficiencies of the three configurations as function of azimuth and zenith angles are shown in Figure 63. The radial configurations allow to eliminate the effect of heliostat alignment when the azimuth angle is around $-100/+100^\circ$, thus increasing the annual optical efficiency. This effect is expected to become even more relevant increasing the size of the module, for this reason the cornfield layout is discarded and substituted for the next analysis with a surrounded field layout.

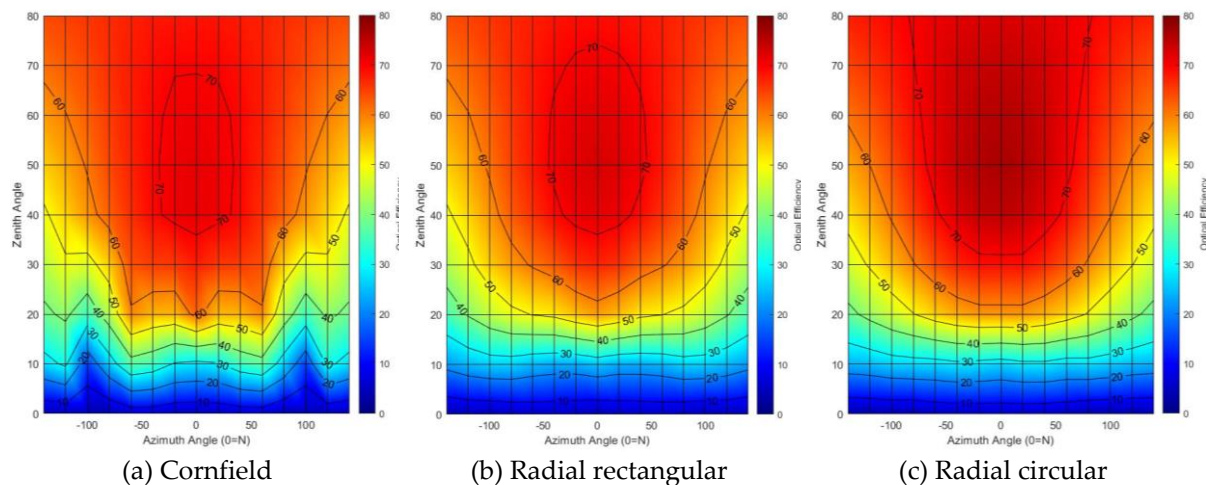


Figure 63 Optical efficiency map of the three optimal configurations

The radial rectangular, the radial circular, and the surrounded layouts are used to investigate the effect on performances and costs of the module size, expressed as the thermal power delivered at design conditions to the receiver. The power is varied from 1 MW_{th} to 10 MW_{th} and for each power and each layout the tower height and receiver size are optimized as function of LCOH. The optical efficiencies obtained for the three module layouts are shown in Figure 64, as function of tower height and receiver area.

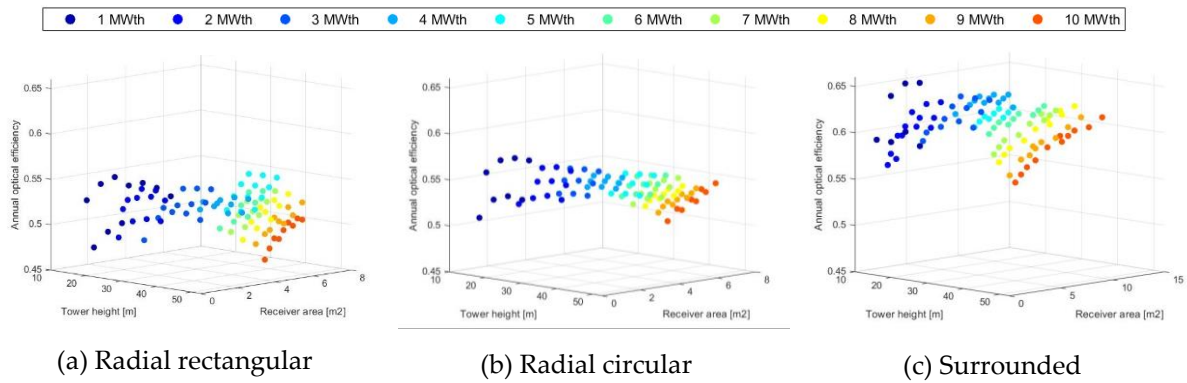


Figure 64 Annual optical efficiency for different tower height, receiver area, module power and module layout

In Figure 65b the annual optical efficiency of the radial circular layout is shown, as representative of the three layouts. The annual optical efficiency improves significantly increasing receiver area and tower height. At the same time the annual optical efficiency decreases considerably with the size of the module. In Figure 65b the annual optical efficiencies of the three layouts together are reported. The surrounded configurations provide higher annual optical efficiency with respect to the two polar configurations as heliostats have better positioning. For the same reason the radial circular layout presents slightly better optical performances with respect to the radial rectangular layout.

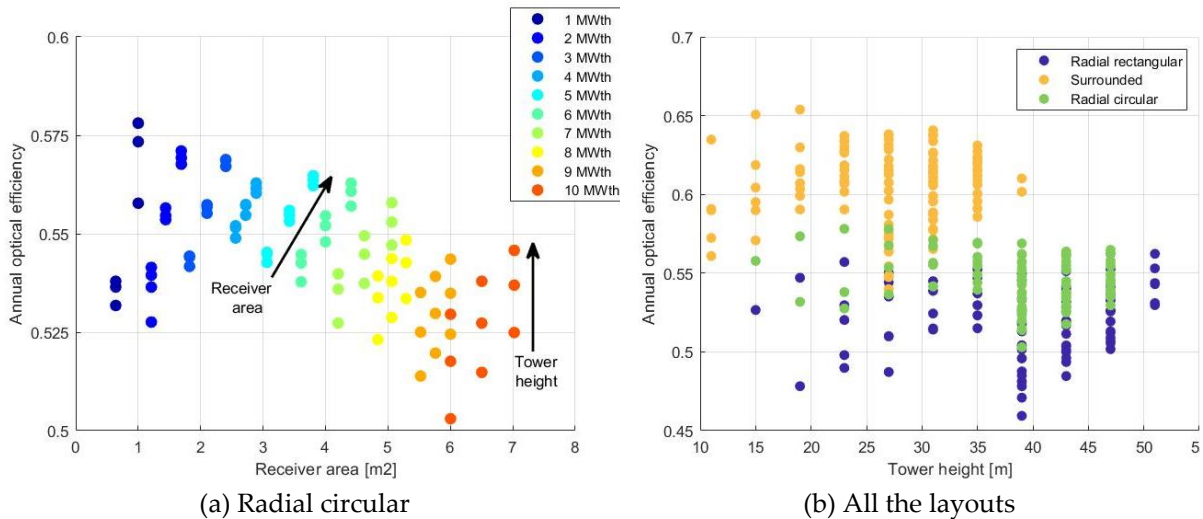


Figure 65 Annual optical efficiency as function of receiver area for different module layouts

The annual thermal efficiencies of the receivers of the three different layouts for different tower heights and receiver areas are shown in Figure 66. The receiver thermal efficiency of the two polar layouts slightly increases with the size of the module: the spacing between the receiver tubes accounts for less surface as the receiver size increases. The receiver thermal efficiency of the surrounded layout increases significantly with the power, as the flux is more evenly distributed on the receiver

surface and receiver size can be reduced remaining below the limit threshold for the maximum peak flux.

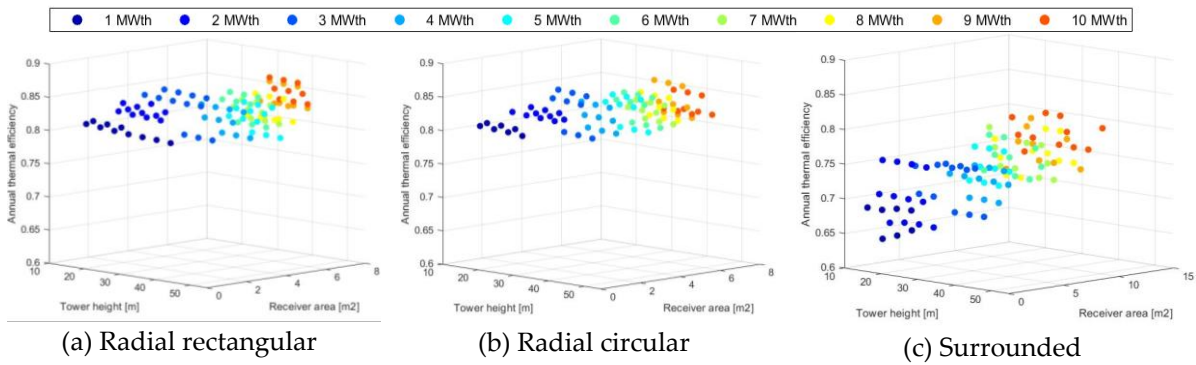


Figure 66 Annual receiver thermal efficiency for different tower height, receiver area, module power and module layout

In Figure 67a the receiver annual thermal efficiency of the radial circular layout is reported, as representative of the three layouts. The receiver annual thermal efficiency strongly depends on the receiver area, as it affects the average flux on the receiver. Increasing the receiver area generally leads to a significant decrease of the thermal performances. Increasing the tower height has a very limited negative effect on the receiver thermal efficiency. In Figure 67b the annual thermal efficiency is shown for the three layouts together. The cylindrical receiver model used in the surrounded configuration leads to lower thermal efficiencies with respect to the billboard receiver model used in the polar configurations. This is due to the fact that the flux is less evenly distributed on the receiver surface. To remain below the maximum peak flux limit bigger receivers are needed, and at the same time the average flux on the receiver reduces, significantly decreasing the performances.

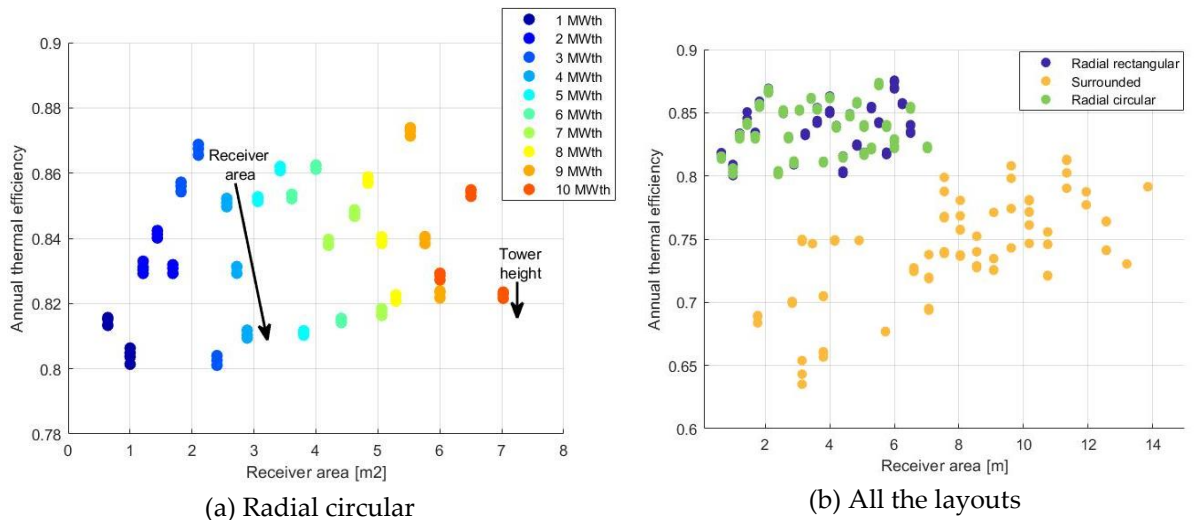


Figure 67 Annual receiver thermal efficiency as function of receiver area for different module layouts

The combined effects of tower height, receiver area, and module power on optical and thermal performances are reported in Figure 68. In Figure 68a and Figure 68b the

optical-thermal efficiencies of the radial circular and the surrounded layouts are shown. For the radial circular configuration, the decrease of optical efficiency increasing the module size is the prevalent effect, thus leading to an overall decrease of performances as the module power increases. The same is true for the radial rectangular configuration. For the surrounded layout the increase of thermal efficiency with module size is the prevalent effect, thus leading to an overall increase of performances as the module power increases. In Figure 68c the optical-thermal efficiencies of the three layouts are reported. The higher optical efficiency of the surrounded layout balances the lower thermal efficiency leading to overall similar performances with respect to the polar layouts.

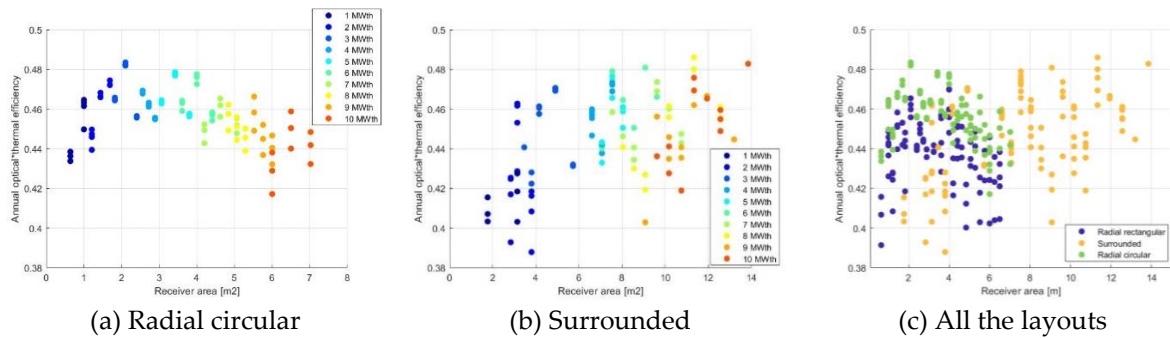


Figure 68 Annual optical-thermal efficiency as function of receiver area for different module layouts

For each module size investigated the values of receiver size and tower height that maximize the optical-thermal efficiency are shown in Figure 69. The optimal receiver area increases almost linearly with the thermal power incident on the receiver. The optimal tower height increases significantly up to 5 MW_{th}. From this point the tower height is not increased further to avoid the much higher costs due to the change in tower type, and to avoid the related much higher LCOH. For this reason, the optical and thermal performances for higher tower heights are not available.

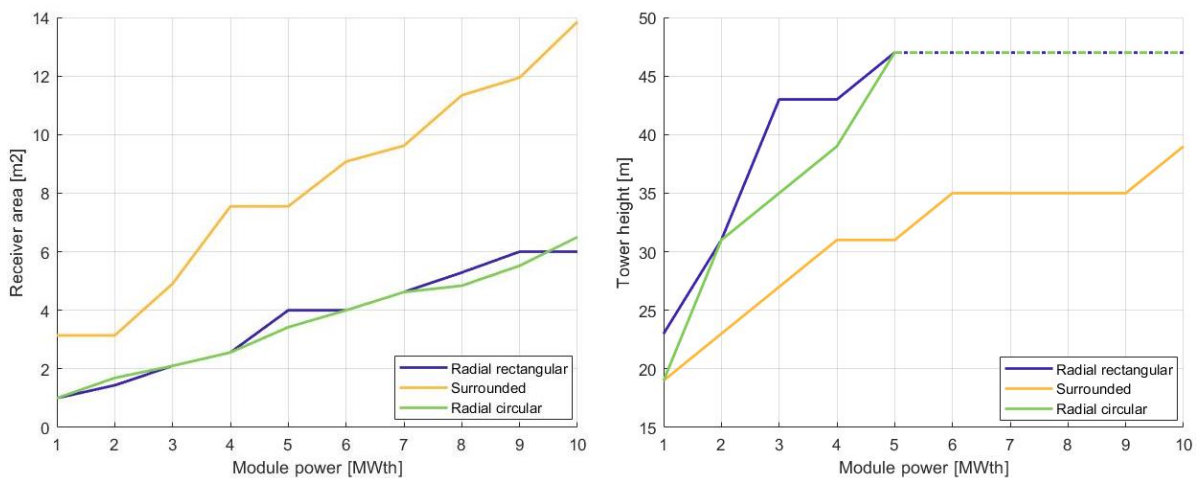


Figure 69 Receiver area and tower height that maximize the optical-thermal efficiency for each module size (expressed as thermal power incident on the receiver)

From the obtained results, for each one of the investigated configurations, the optical efficiency and the thermal efficiency can be estimated for any value of tower height, receiver area, and module power around the computed points. In Figure 70 the interpolated values for the surrounded configuration are shown.

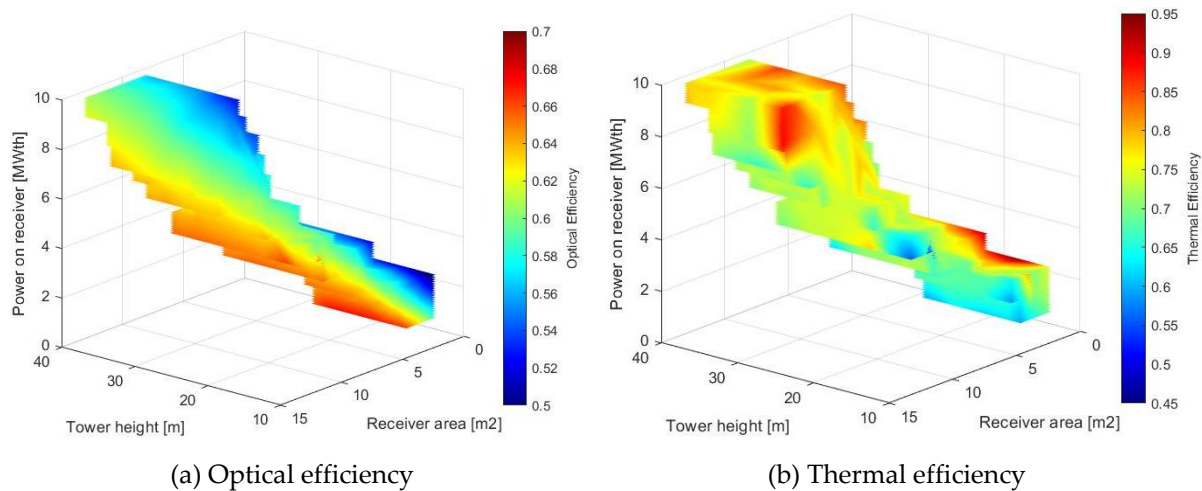


Figure 70 Interpolated values of optical efficiency and thermal efficiency in the regions close to the computed points for the modular surrounded layout

With the cost assumptions reported in Table 9 the LCOH for the different investigated modular configurations can be evaluated. The results for the radial circular and the surrounded layouts are reported in Figure 71. In Figure 71a the LCOH values of the radial circular layout as function of tower height are illustrated. The change of the tower technology and the associated cost correlation for tower heights greater than 45 m significantly increases the LCOH of the radial circular layout. For this reason, the optimal values of tower height that minimize the LCOH are all below 45m. In Figure 71c the LCOH values of the radial circular layout as function of receiver area are shown. The LCOH generally increases when increasing the receiver area, as the higher thermal efficiency is counterbalanced by significantly higher costs. Very small modules, around 1-2 MW_{th}, and very large modules, around 9-10 MW_{th}, present higher LCOH values with respect to modules in the mid-size range. The same considerations are valid for the radial rectangular layout. In Figure 71b and Figure 71d the LCOH values for the surrounded layout are reported. As in the case of the polar layouts increasing the receiver area results in higher values of LCOH. The tower heights that allow to minimize the LCOH remain below the threshold of 45 m. Increasing the module size reduces the LCOH of the surrounded layout, as thermal efficiency improves significantly.

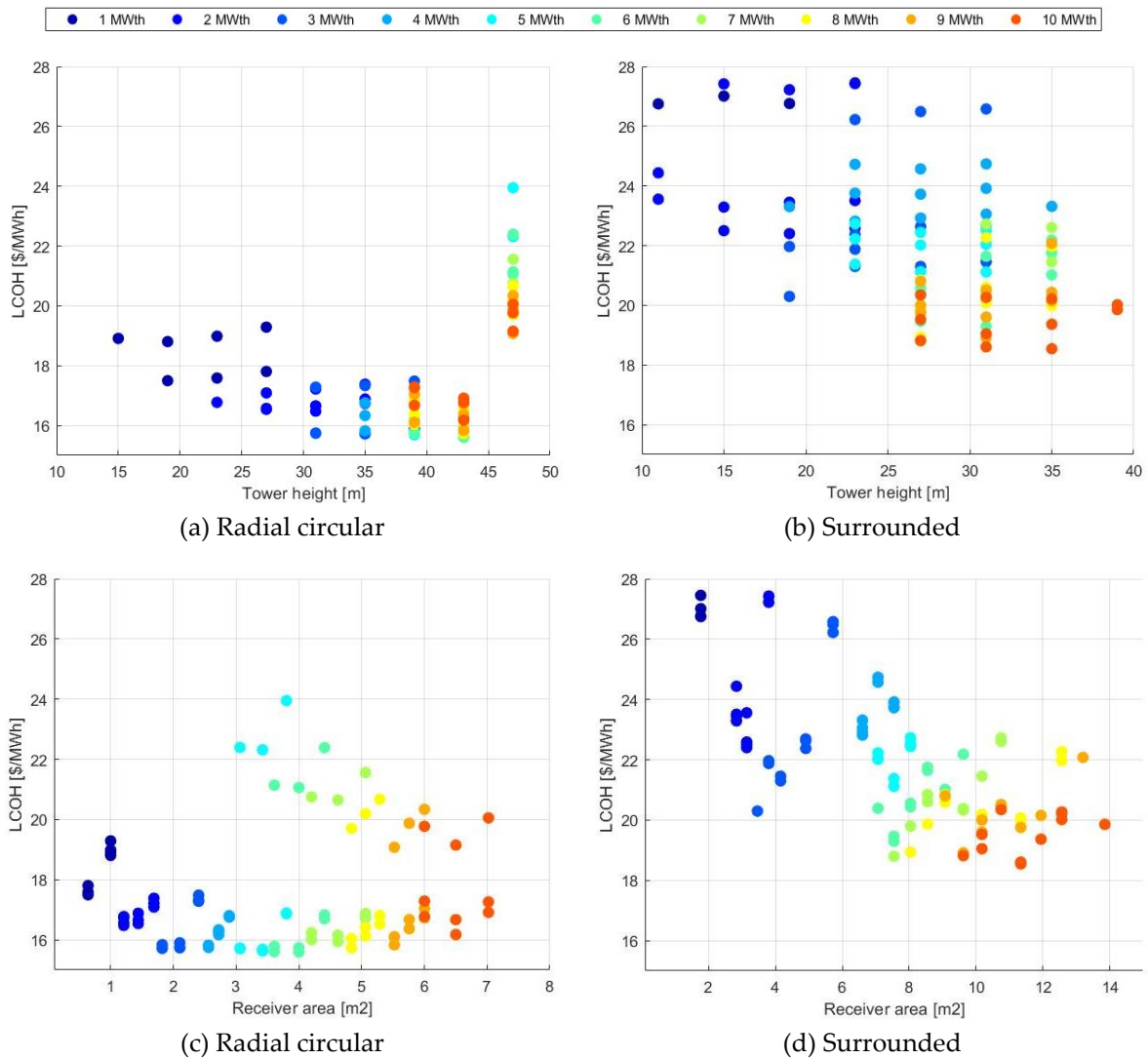


Figure 71 LCOH as function of tower height and receiver area for the radial circular and the surrounded layouts

The LCOH obtained for the three modular layouts are compared with the LCOH obtained for two single field plants. The first single field plant considered is the optimized polar single field plant discussed in Section 4.1, with solar multiple equal to 3, tower height of 100 m and a 5 x 5 m receiver. The second single field plant is a surrounded plant with solar multiple equal to 3.6. The tower height and the receiver area are optimized, and the obtained values are 60 m for the tower height and 43 m² for the receiver area. The LCOH values of the modular configurations, and the two LCOH values of the optimized single field configurations, are shown in Figure 72. The modular surrounded layout reaches very similar LCOH values to the single field surrounded configuration. The radial rectangular and the radial circular modular layout reach lower LCOH values with respect to the single field configurations.

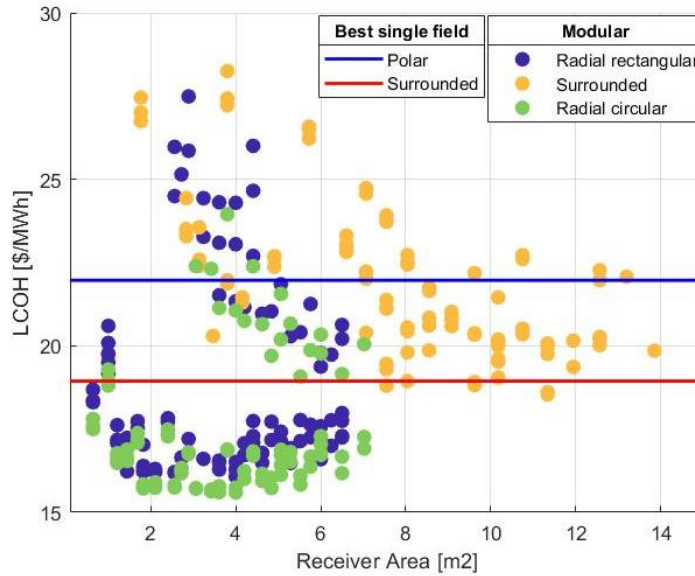


Figure 72 LCOH values of the three modular layouts and the two optimal single field configurations

For each module layout and each module size the optimal values of tower height and receiver size that minimize the LCOH are identified. In Figure 73 the identified values are reported, together with the values of tower height and receiver area that optimize the optical-thermal efficiency. In the case of the radial rectangular and the radial circular layouts the values of receiver area and tower height that optimize the LCOH, and the values that optimize the optical-thermal efficiency are very close. In the case of the surrounded layout the values of receiver area and tower height that optimized the LCOH are significantly lower than the values that optimize the optical-thermal efficiency. In the surrounded layout the improvement of optical-thermal performances is not enough to compensate the cost increase associated with higher towers and bigger receivers.

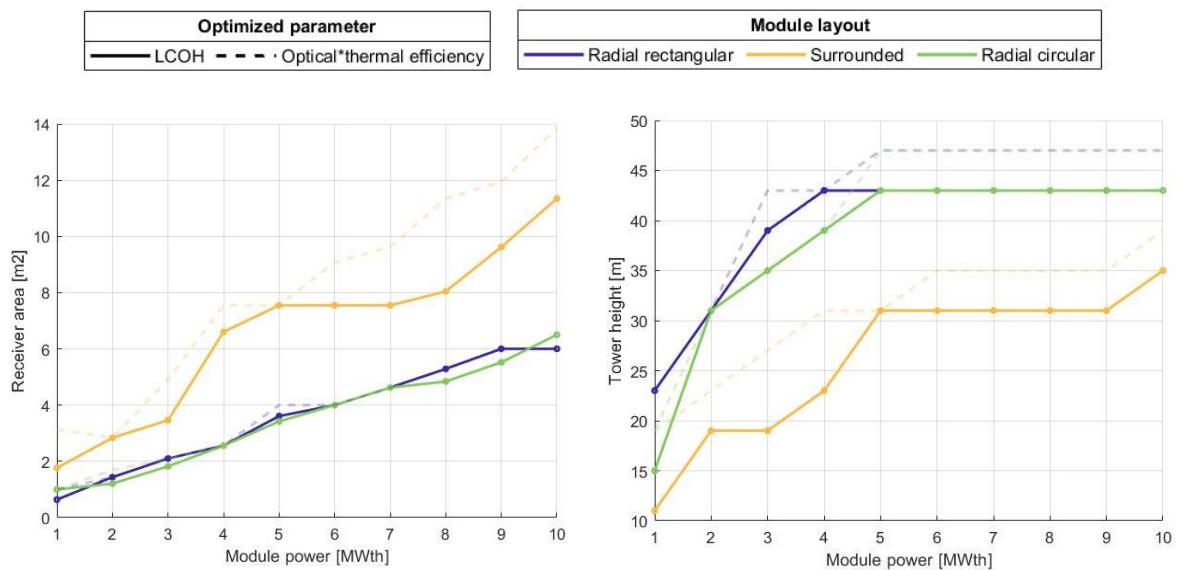


Figure 73 Receiver area and tower height that minimize the LCOH for each module layout

For each module size and each module layout the geometry corresponding to the identified values of tower height and receiver area that optimize the LCOH are selected for the analysis of the LCOE. For each one of the 30 selected geometries (10 for each module layout, 1 for each module size) the solar multiple is changed adjusting the number of modules, and the corresponding piping thermal efficiency and solar to electric efficiency are evaluated. In Figure 74 the obtained values of piping annual thermal efficiency for the radial circular layout are reported as function of the solar multiple and the number of modules. Increasing the solar multiple decreases the piping performances, as a higher number of modules is required. This effect is more relevant for bigger module sizes as the total number of modules is lower and the addition of one module to increase the solar multiple has bigger impact. The piping efficiency mainly depends on the number of modules: a higher number of modules implies a more extended piping network and increased thermal losses. This effect is particularly relevant for a small number of modules (1 to 6). Increasing the number of modules, the piping efficiency becomes more sensitive to the size of the modules. Very small and very big modules result in lower piping efficiency with respect to mid-size modules.

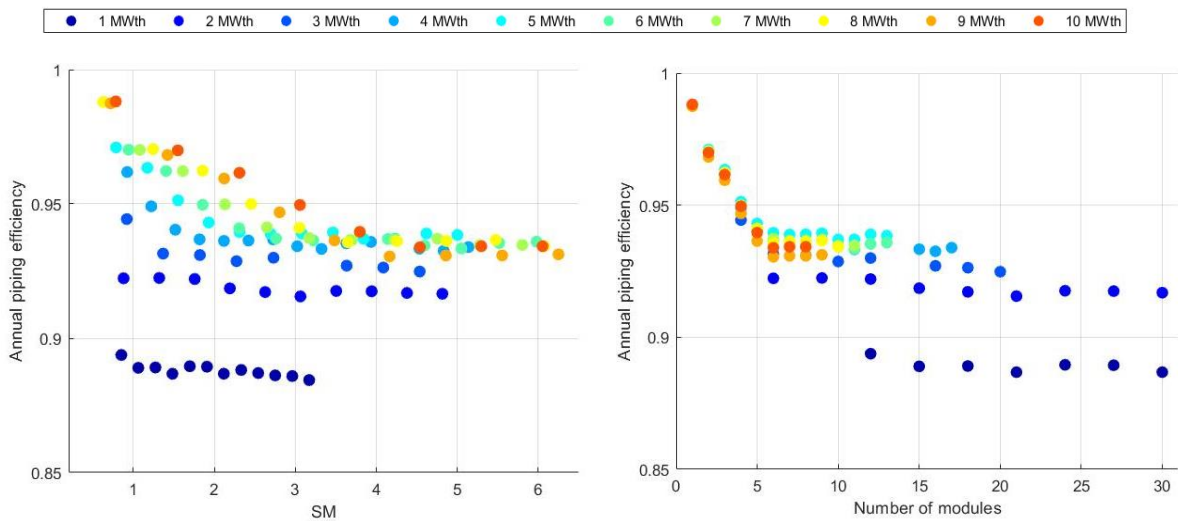


Figure 74 Piping annual thermal efficiency as function of solar multiple and number of modules for the radial circular layout optimal geometries

With the obtained values it is possible to evaluate the piping annual thermal efficiency for any number of modules and module size in the region close to the computed points, as shown in Figure 75.

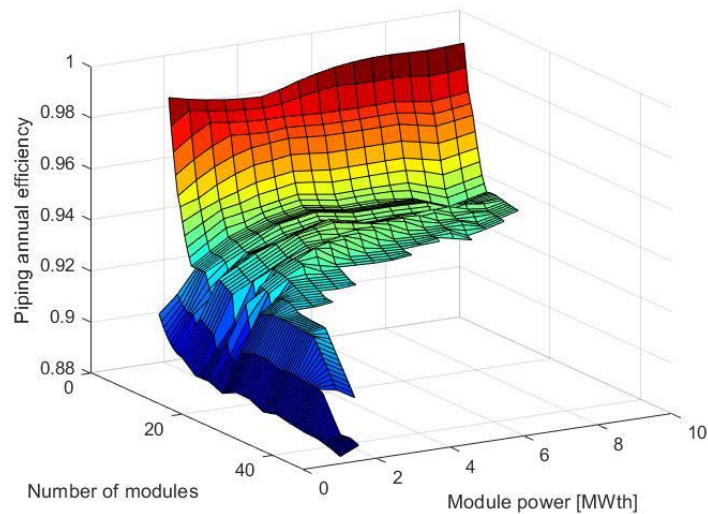


Figure 75 Piping annual thermal efficiency as function of number of modules and power of the module for the radial circular layout

The annual solar to electric efficiencies of the radial circular and the surrounded layouts, as function of solar multiple and number of modules, are reported in Figure 76. The considerations referring to the radial circular layout also apply to the radial rectangular layout as they present very similar results. The STE efficiency of all the configurations decreases when the solar multiple and the number of modules increase, as the reduction of the piping efficiency significantly affects the system. This effect is particularly relevant for a low number of modules as shown in Figure 76c and Figure 76d. In the case of the radial circular layout, given a certain solar multiple, very small modules (1-2 MW_{th}) and very large modules (9-10 MW_{th}) are less efficient than modules in the mid-size range, as the better piping performances of large modules are not enough to balance the worse optical-thermal performances. On the other hand, in the case of the surrounded layout, for a given solar multiple the largest module is more efficient as it presents higher piping efficiency and also higher thermal-optical efficiency. It is important to remind that the module geometries selected for each layout and each size are the one optimizing the LCOH and not the thermal-optical efficiency; this can create more differences in the efficiency values of different module sizes. For all the different layout configurations investigated the values of STE efficiency are almost in the same range of 17-21 %.

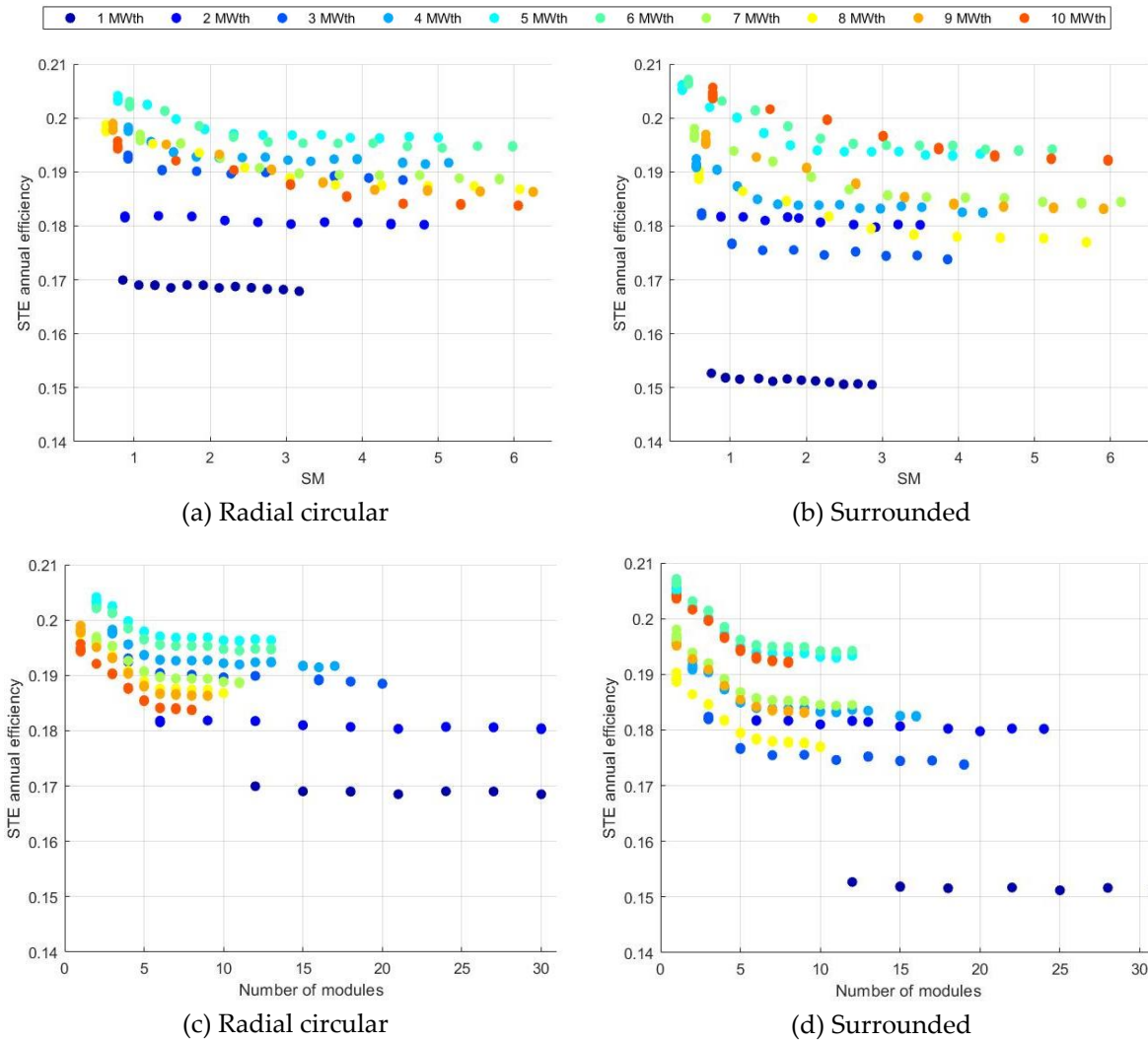


Figure 76 Annual solar to electric efficiency as function of solar multiple and number of modules, for the radial circular and the surrounded layouts

For each module layout, each module size, and each solar multiple the TES size is varied and the LCOE is computed to identify the optimal configuration. The results for the radial circular configuration are reported in Figure 77. In Figure 77a the results for the 5 MW_{th} radial circular module are shown. Increasing the solar multiple the optimal TES size increases. The size of the module has very limited effect on the optimal TES size, as illustrated in Figure 77b, where the optimal TES size, for each solar multiple and module thermal power, is reported. At very high values of solar multiple the optimal TES becomes constant.

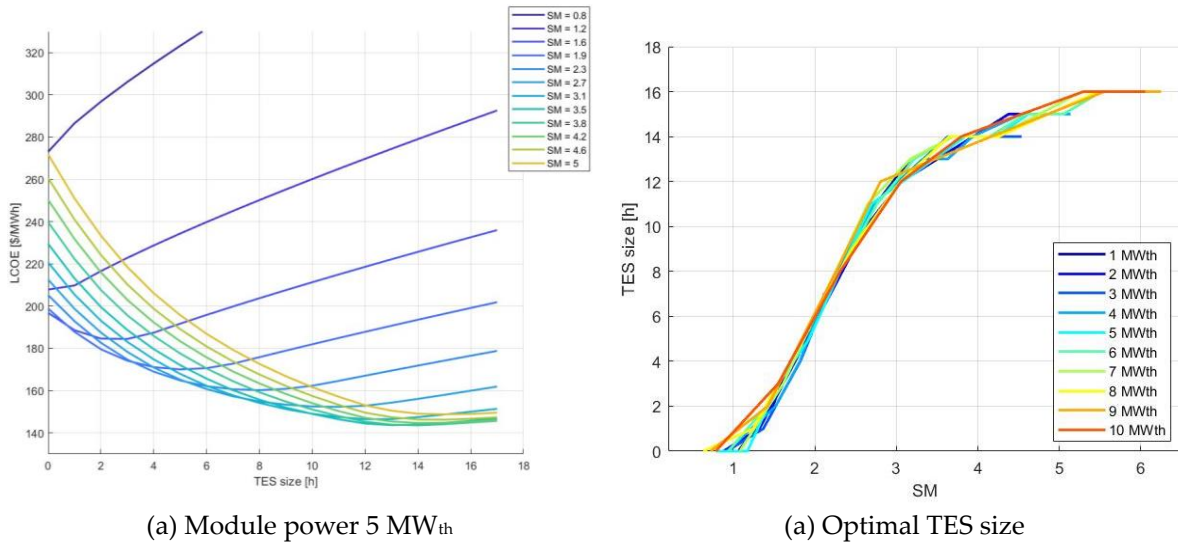


Figure 77 LCOE as function of SM and TES size for the 5 MW_{th} module and optimal TES size as function of SM and module power for the radial circular layout

The LCOE values of the different configurations with optimized TES size are shown in Figure 78. The LCOE depends significantly on the solar multiple, while it is much less dependent on the module size. The surrounded layout configurations present higher LCOE values with respect to the two polar layouts, mainly because of the higher cost associated to the receiver.

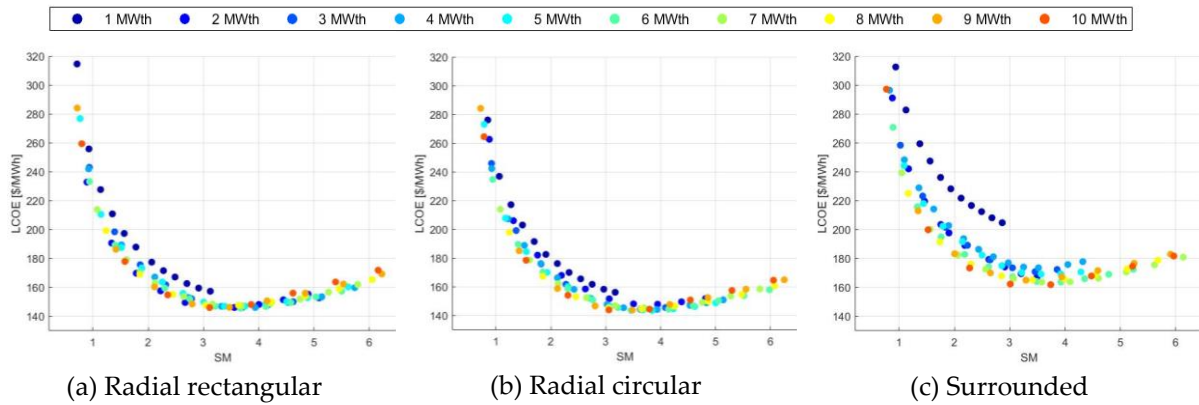


Figure 78 LCOE as function of solar multiple for different module power and layout with optimized TES size

For each module thermal power and for each module layout the optimal solar multiple and the optimal number of modules are identified, as shown in Figure 79. For any module layout and module size the optimal solar multiple is in the range 3-4. This leads to very small differences in the optimal number of modules among the three different module layouts. The lower optimal solar multiple for very small and very big module sizes reflects the piping efficiency trends discussed before.

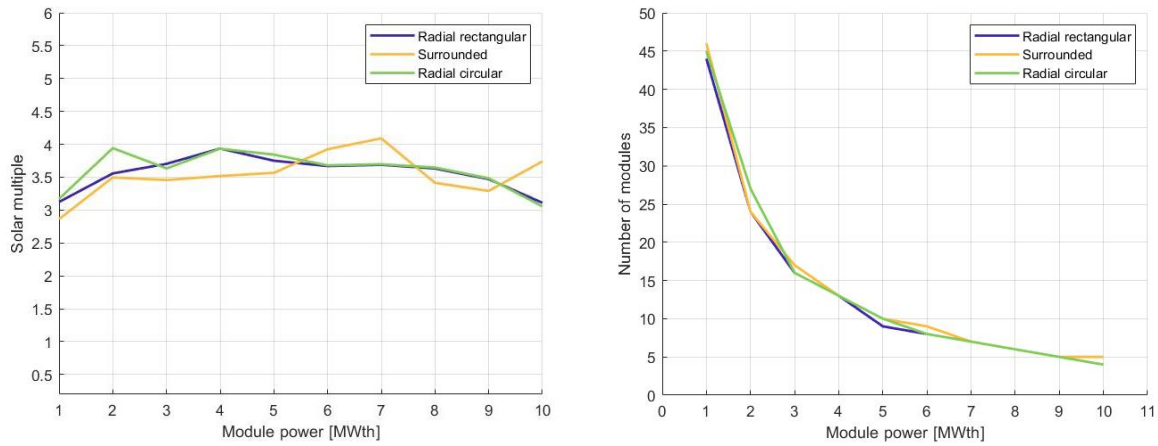


Figure 79 Optimal solar multiple and number of modules for each considered layout

The LCOE values of the optimized modular and single field configurations are shown in Figure 80. In the case of the radial rectangular and the radial circular layouts the optimization of TES size and solar multiple leads to very similar LCOE values independently from the module size. The radial circular layout performs slightly better than the radial rectangular layout. For the surrounded layout bigger modules present lower LCOE values, mainly because of the higher receiver cost. A very small module of 1 MW_{th} leads to very high LCOE values for any module layout, as the high number of modules significantly reduces the piping efficiency. The surrounded module reaches LCOE values higher than the one obtained with a corresponding single field plant: they present similar performances, but the modular layout is affected by the higher cost associated to the piping system. In the case of the polar layouts the modular configuration allows to reach noticeably lower LCOE values with respect to the single field counterparts. This is due to the better efficiency of the modular configurations at a very similar cost with respect to the single field layouts.

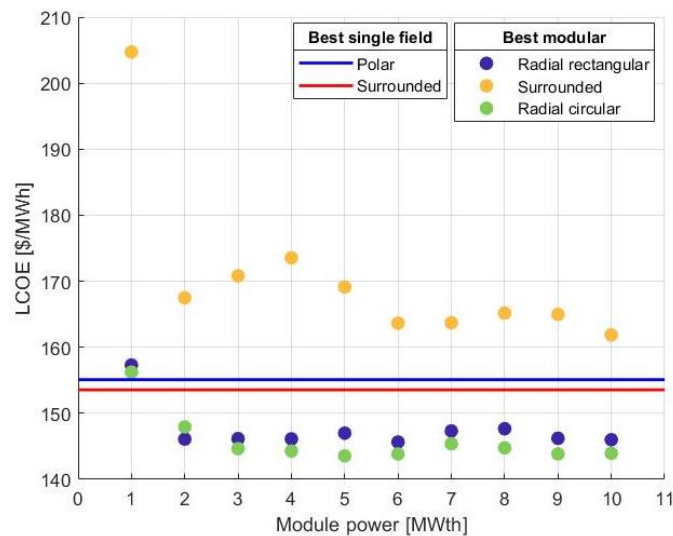


Figure 80 LCOE values of the optimal modular and single field configurations

For each module layout the configurations with the lowest LCOE are compared in detail with the two optimal single field configurations. The results are reported in Table 16. The best radial rectangular configuration has 8 modules of 6 MW_{th} of power, and optimal solar multiple equal to 3.7. The best radial circular configuration presents 10 modules of 5 MW_{th} of power, and optimal solar multiple equal to 3.8. The best surrounded configuration comprises 5 modules of 10 MW_{th} of power, and solar multiple equal to 3.7.

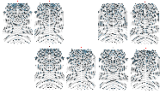
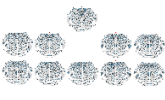
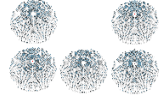
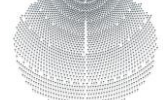

	Radial rectangular	Radial circular	Modular surrounded	Single field polar	Single field surrounded
Layout					
Number of modules	8	10	5	-	-
Reflective area	76 920 m ²	74 450 m ²	68 800 m ²	75 800 m ²	69 840 m ²
Tower height (Optimized)	43 m	43 m	35 m	90 m	60 m
Receiver size (Optimized)	2 x 2 m	1.85 x 1.85 m	1.9 x π x 1.9 m	5.5 x 5.5 m	3.7 x π x 3.7 m
Solar multiple (Optimized)	3.7	3.8	3.7	3.1	3.6
TES size (Optimized)	14 h	14 h	13	13 h	13 h
Design power incident on receiver (Optimized)	6 MW _{th}	5 MW _{th}	10 MW _{th}	40 MW _{th}	47 MW _{th}
Annual STE efficiency	18.6 %	19.6 %	19.4 %	16.5 %	18.8 %
AEP	31.3 GWh	31.4 GWh	29.2 GWh	29.4 GWh	30.1 GWh
CAPEX _{tot}	46.5 M\$	45.9 M\$	48.3 M\$	46.4 M\$	45.4 M\$
LCOE	145.7 \$/MWh	143.6 \$/MWh	161.8 \$/MWh	155.1 \$/MWh	153.6 \$/MWh
CF	71.5 %	71.8 %	66.6 %	67.0 %	68.7 %

Table 16 Main parameters and performances of the modular and single field optimal configurations

The annual efficiencies and the specific cost of each configuration are shown in Figure 81. The modular configurations present significantly higher optical efficiencies with respect to the single field polar configuration. Instead, the single field surrounded configuration shows optical efficiency similar to the modular configurations. The single field configurations benefit from higher piping performances with respect to the modular layouts. The investment cost related to the heliostats is lower in the surrounded layouts, thanks to the better optical performances. The smaller heights of the towers adopted in the modular configurations allow to adopt steel lattice tower at

much lower investment cost. The surrounded configurations present higher receiver cost due to the higher necessary receiver area. The single field configurations show significantly lower investment cost for the piping system.

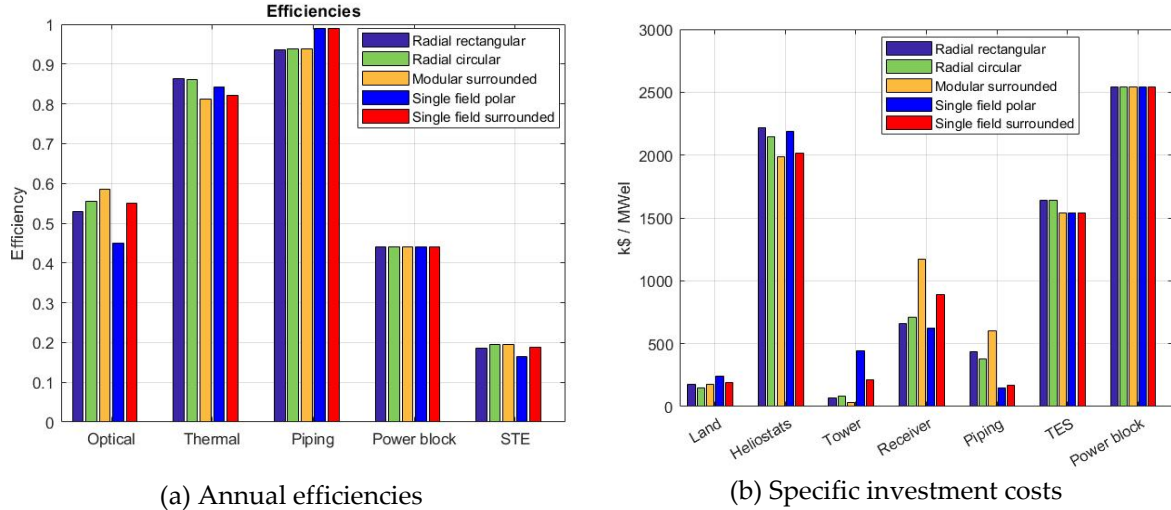


Figure 81 Annual efficiencies and specific investment cost for the optimal modular and single field configurations

Finally, the power block size is varied from the original 5 MW_{el} to 2.5 MW_{el} and 7.5 MW_{el}, to evaluate the impact on solar multiple and performances. The results are shown in Figure 82. The optimal solar multiple is lower for increased power block size, as a higher number of modules is needed to reach high solar multiple values, especially for small modules. When the power block size decreases the optimal solar multiple remains almost in the same range around values of 3-4. This variation is not uniform for big modules as the addition/removal of one module significantly varies the solar multiple.

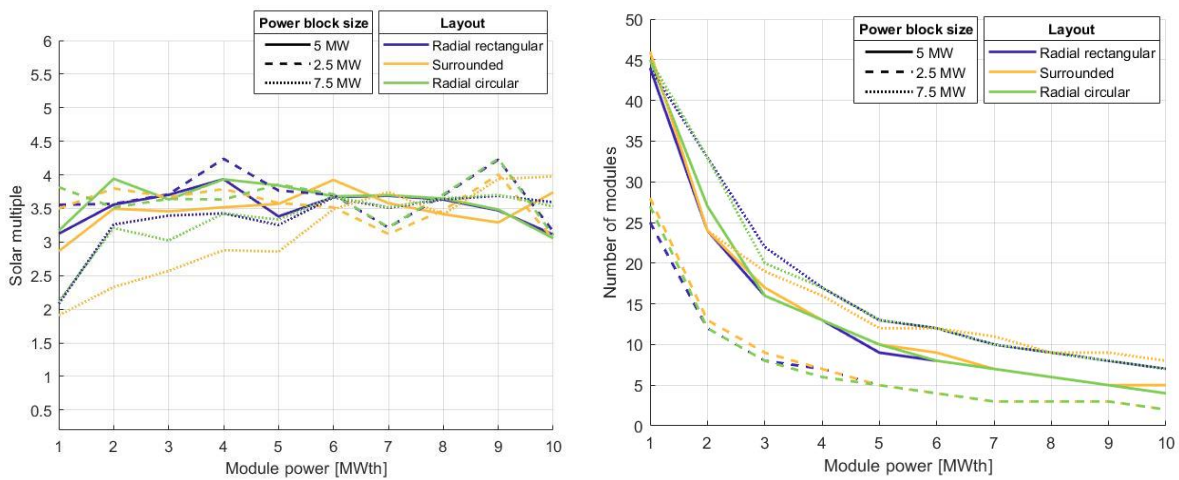


Figure 82 Effect of power block size on optimal solar multiple and number of modules for the three different module layouts

The effect of the size of the power block on the LCOE values obtained for the optimal modular configurations is illustrated in Figure 83. For polar layouts and small module sizes the increase of power block size results in a slight decrease of the LCOE, as they are less affected by the addition of modules. Big module sizes instead go from 4-5 modules to 7-8 modules, the piping efficiency reduces significantly and the LCOE increases. The reduction of power block size increases the LCOE for small module sizes, while it is beneficial for big modules, as 2-3 modules are enough to provide the optimal solar multiple.

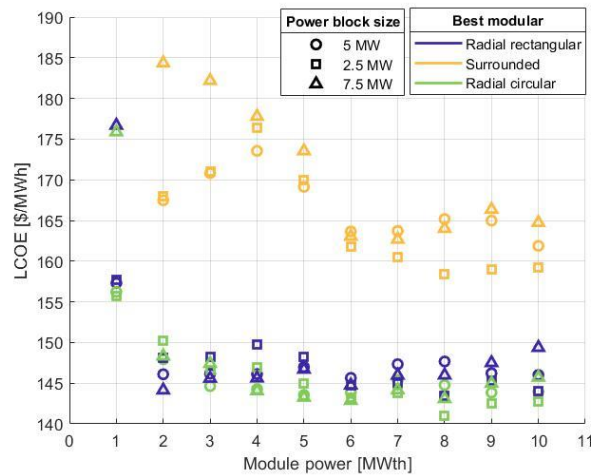


Figure 83 LCOE for different layouts, different module sizes and different power block sizes. Lastly, the piping cost is varied by $\pm 25\%$ for each configuration. The results are reported in Figure 84. The values of optimal solar multiple for all the layouts remain in the range between 3 and 4, but the variation of piping cost can lead to the adoption of configurations with ± 1 module for some module sizes with respect to the baseline case.

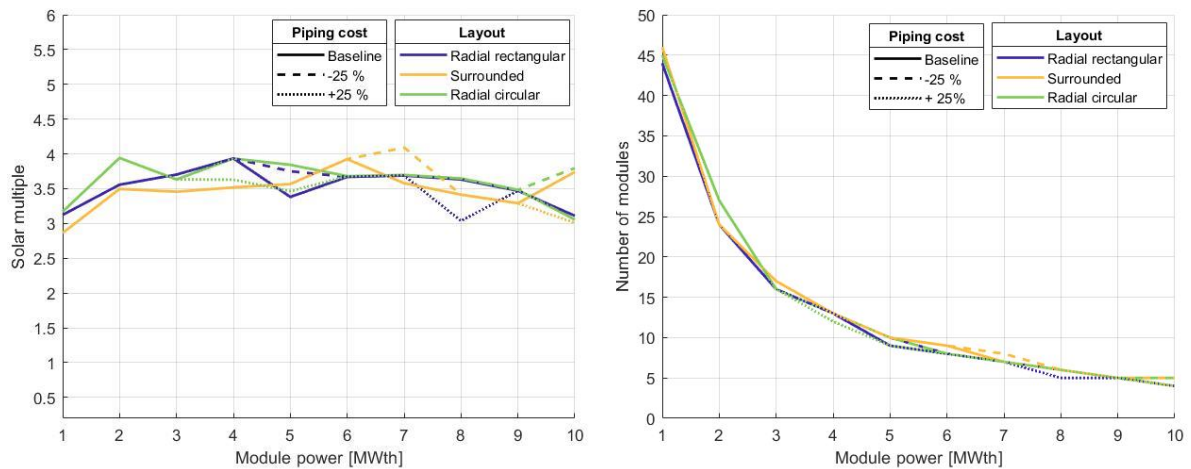


Figure 84 Effect of piping cost variation on optimal solar multiple and number of modules for the three different module layouts

The obtained LCOE values are shown in Figure 85. A 25 % variation in the piping cost leads to an increase/decrease of 1-1.5 % in the values of LCOE obtained with the modular configurations, while it leaves practically unchanged the values obtained with the single field configurations.

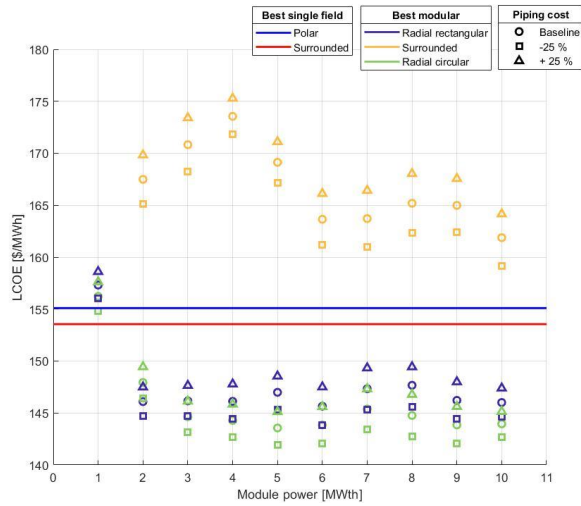


Figure 85 LCOE for different layouts, different module sizes and different piping cost

5 Conclusion

This thesis work investigated from a techno-economic perspective different possible modular configuration for a CSP tower plant. The first part of the work focused on modules adopting a cornfield heliostat disposition and operating in two temperature ranges. The configurations operating in the higher temperature range performed better, with a ~7% lower LCOE, and were selected for the optimization of tower height, receiver area, solar multiple, and TES size. The optimized modular configuration showed a value of LCOE very similar to the value of the corresponding optimized single field plant. To better exploit the possibility of the modular approach different heliostat disposition and different module sizes were analysed. For each configuration the best tower height and receiver area were identified by minimizing the LCOH. From the computed points the optical and thermal efficiency for any values of tower height, receiver area, module size, and for three different heliostat disposition can be estimated. For each optimal module geometry, the best plant design, in terms of solar multiple and TES size, was selected by minimizing the LCOE.

The obtained results provide possible selection criteria for the optimal number of modules, solar multiple, and module size, for a modular tower plant. The optimal solar multiple for all the investigated configurations was in the range from 3 to 4, with a corresponding optimal TES size in the range 12-14 h. The radial circular modular configuration, formed by 10 modules of 5 MW_{th} of power, proved to be the best candidate with a LCOE of 143.6 \$/MWh. The best radial rectangular modular configuration, with 8 modules of 6 MW_{th} of power, and optimal solar multiple equal to 3.7, reached a LCOE of 145.6 \$/MWh. The best surrounded modular configuration, with 5 modules of 10 MW_{th} of power, and solar multiple equal to 3.7, reached a LCOE of 161.8 \$/MWh. The best single field configuration presented a LCOE of 153.6 \$/MWh, a value 6.5 % higher than the LCOE obtained with the best modular configuration.

It is important to note that the modelling of solar field, receiver, and piping system was implemented to have a high degree of accuracy, while the TES and the power block system were treated with a much simpler approach, neglecting heat exchangers and thermal losses in the storage tanks. This approach was intended to focus the analysis on the subsystems that are different between the modular and the single field configurations. Also, aspects related to materials compatibility and corrosion using liquid sodium as heat transfer fluid were not thoroughly investigated. It is important to underline that the obtained values of LCOH and LCOE strongly depend on the assumed costs for the different system components. Due to the high uncertainty

associated to cost correlations and to the difficulty to retrieve accurate and reliable cost data the economic parameters are subjected to significant variability. Nevertheless, the economic parameters were obtained applying coherent cost assumptions between modular and single field configurations, proving that the modular layout can be competitive. It is also important to stress that possible cost reductions due to the modularization of system components were not considered and could play a relevant role in making modular configurations more convenient.

Future works should investigate the effect of heliostat size on system costs and performances. Also, the receiver aspect ratio should be varied to evaluate possible advantages in terms of optical-thermal efficiency and costs, especially for the surrounded layouts. Plants with power blocks of increased size, e.g., 25-50 MW_{el}, should be investigated, as the constant optical efficiency obtained with the modular approach could provide a more significant advantage with respect to the single field configurations, where solar fields of increasing size are required.

Bibliography

- [1] bp, "bp Statistical Review of World Energy 2022," BP p.l.c., London, 2022.
- [2] Ember, "Global Electricity Review 2022," Ember, London, 2022.
- [3] International Energy Agency, "World Energy Outlook 2022," International Energy Agency, Paris, 2022.
- [4] IPCC, "Climate Change 2022: Impacts, Adaptation and Vulnerability," Cambridge University Press, Cambridge (UK), 2022.
- [5] NREL, "Concentrating Solar Power Gen3 Demonstration Roadmap," NREL, 2017.
- [6] International Energy Agency, "Technology Roadmap Concentrated Solar Power," IEA, Paris, 2010.
- [7] SolarPACES, "CSP Projects Around the World," Solarpaces, 2020. [Online]. Available: <https://www.solarpaces.org/csp-technologies/csp-projects-around-the-world/>.
- [8] REN21, "Renewables 2022 Global Status Report," REN21, Paris, 2022.
- [9] J. H. Lim, B. B. Dally, A. Chinnici and G. J. Nathan, "Techno-economic evaluation of modular hybrid concentrating solar power systems," *Energy*, vol. 129, pp. 158-170, 2017.
- [10] L. Crespo and F. Ramos, "Making central receiver plants modular, more efficient and scalable," *AIP Conference Proceedings*, vol. 2303, 2020.
- [11] C. Tyner and D. Wasyluk, "eSolar's Modular, Scalable Molten Salt Power Tower Reference Plant Design," *Energy Procedia*, pp. 1563-1572, 01 January 2014.
- [12] L. Crespo, A. Ramos, F. Ramos and D. Crespo, "Revisiting field layout designs for large STE tower plants," *AIP Conference Proceedings*, vol. 2033, 2018.

- [13] M. Puppe, S. Giuliano, C. Frantz, R. Uhlig, R. Flesch, R. Schumacher, W. Ibraheem, S. Schmalz, B. Waldmann, C. Guder, D. Peter, C. Schwager, C. T. Boura, S. Alexopoulos and M. Spiegel, "Techno-economic optimization of molten salt solar tower plants," *AIP Conference Proceedings*, vol. 2033, 2018.
- [14] J. García-Barberena, A. Monreal, A. Mutuberría and M. Sánchez, "Towards Cost-competitive Solar Towers – Energy Cost Reductions based on Decoupled Solar Combined Cycles (DSCC)," *Energy Procedia*, vol. 49, pp. 1350-1360, 2014.
- [15] J. Sorbet, M. Iñigo, J. García-Barberena and A. Bernardos, "Advanced power cycles and configurations for solar towers: Techno-economical optimization of the decoupled solar combined cycle concept," *AIP Conference Proceedings*, vol. 2033, 2018.
- [16] J. E. Rea, C. J. Oshman, M. L. Olsen, C. L. Hardin, G. C. Glatzmaier, N. P. Siegel, P. A. Parilla, D. S. Ginley and E. S. Toberer, "Performance modeling and techno-economic analysis of a modular concentrated solar power tower with latent heat storage," *Applied Energy*, vol. 217, pp. 143-152, 2018.
- [17] T. Lindquist, J. Karlsson, J. Wallmänder, R. Guedez, H. Maria-Lina, J. Jakob, D. Gloss, J. Lindh, A. Hertin, M. Nilsson, A. Abou-Taouk, K. Kjellin and H. Bouzekri, "A novel modular and dispatchable CSP Stirling system: Design, validation, and demonstration plans," *AIP Conference Proceedings*, vol. 2126, 2019.
- [18] K. Kopilovsky, "Earth Times," 18 May 2012 . [Online]. Available: <https://earthtimes.org/energy/aora-solar-energy-tulips/1997/>. [Accessed 05 February 2023].
- [19] W. Weisinger, "EnergyPedia," 7 April 2016. [Online]. Available: https://energypedia.info/images/d/d5/2._Mr_William_Weisinger_-_Solar_Ethiopia%2C_biogas_hybrid.pdf. [Accessed 2023 February 05].
- [20] Lloyd Energy Systems Pty Ltd, "Lake Cargelligo Solar Thermal Project Final Public Report," 2011.
- [21] C. F. 光略咨询, "CSP Focus," July 2022. [Online]. Available: http://www.cspfocus.cn/en/report/detail_39.htm. [Accessed 07 February 2023].
- [22] E. Morosini, G. Gentile, M. Binotti and G. Manzolini, "Techno-economic assessment of small-scale solar tower plants with modular billboard receivers and innovative power cycles," in *ATI Annual Congress*, Bari, 2022.

- [23] M. J. Wagner and T. Wendelin, "SolarPILOT: A power tower solar field layout and characterization tool," *Solar Energy*, vol. 171, pp. 185-196, 2018.
- [24] Haynes International, "Haynes International," [Online]. Available: https://haynesintl.com/docs/default-source/pdfs/new-alloy-brochures/high-temperature-alloys/brochures/230-brochure.pdf?sfvrsn=ae7229d4_86. [Accessed 08 03 2023].
- [25] Ferrobend, "Ferrobend," [Online]. Available: <https://ferrobend.com/dimensions/ansi-asmepipe/b36.10m/>. [Accessed 03 06 2022].
- [26] A. S. Foust, L. A. Wenzel, C. W. Clump, M. Louis and L. B. Andersen, *Principles Of Unit Operations*, John Wiley & Sons Inc, 1980.
- [27] S. W. C., "Long-wave radiation from clear skies," *Q.J.R. Meteorol. Soc.*, vol. 89, no. 381, pp. 339-348, 1963.
- [28] A. M. Bonanos, M. C. Georgiou, K. G. Stokos and C. N. Papanicolas, "Engineering aspects and thermal performance of molten salt transfer lines in solar power applications," *Applied Thermal Engineering*, vol. 154, pp. 294-301, 2019.
- [29] K. Mikityuk, "Heat transfer to liquid metal: Review of data and correlations for tube bundles," *Nuclear Engineering and Design*, vol. 239, no. 4, pp. 680-687, 2009.
- [30] Engineering ToolBox, "Steel Pipes - Calculate Thermal Expansion Loops," 2008. [Online]. Available: https://www.engineeringtoolbox.com/steel-pipe-expansion-loop-d_1069.html. [Accessed 09 03 2023].
- [31] F. M. White, *Fluid Mechanics*, 7 ed., McGraw Hill, 2011.
- [32] I. E. Idel'chik, *Handbook of hydraulic resistance*, 4 ed., Begell House, 2007.
- [33] G. Gentile, G. Picotti, M. Binotti, M. E. Cholette and G. Manzolini, "Dynamic thermal analysis and creep-fatigue lifetime assessment of solar tower external receivers," *Solar Energy*, 2022.
- [34] M. Sarvghad, T. C. Ong, S. Bell, R. Rumman, S. D. Maher, J. W. Woodcock, G. A. G. Will, D. A. Lewis and T. A. Steinberg, "On the compatibility of liquid sodium as heat transfer fluid for advanced concentrated solar thermal energy systems," *Solar Energy Materials and Solar Cells*, vol. 246, 2022.

- [35] M. Stewart, "Pipe expansion and flexibility," in *Surface Production Operations*, Boston, 2016, pp. 731-812.
- [36] T. Conroy, M. N. Collins, J. Fisher and R. Grimes, "Thermohydraulic analysis of single phase heat transfer fluids in CSP solar receivers," *Renewable Energy*, vol. 129, pp. 150-167, 2018.
- [37] Vast Solar, "Vast Solar Knowledge Sharing Events and Activities – Narrative Reports," Vast Solar Pty Ltd, Darlinghurst NSW, 2019.
- [38] C. W. Wood and K. Drewes, "Vast Solar: improving performance and reducing cost and risk using high temperature modular arrays and sodium heat transfer fluid," in *SolarPACES Conference*, 2019.
- [39] U.S. Department of Energy, "Quadrennial Technology Review 2015 - Supercritical Carbon Dioxide Brayton Cycle," 2016.
- [40] C.-A. Asselineau, J. Pye and J. Coventry, "Exploring efficiency limits for molten-salt and sodium external cylindrical receivers for third-generation concentrating solar power," *Solar Energy*, vol. 240, pp. 354-375, 2022.
- [41] T. Conroy, M. N. Collins and R. Grimes, "Integrated optical-thermal-mechanical model for investigations into high temperature sodium receiver operation," *Solar Energy*, vol. 194, pp. 751-765, 2019.
- [42] R. Jacob, M. Belusko, A. Inés Fernández, L. F. Cabeza, W. Saman and F. Bruno, "Embodied energy and cost of high temperature thermal energy storage systems for use with concentrated solar power plants," *Applied Energy*, vol. 180, pp. 586-597, 2016.
- [43] G. Manzolini, G. Lucca, M. Binotti, G. Lozza and R. Energy, "A two-step procedure for the selection of innovative high temperature heat transfer fluids in solar tower power plants," *Renewable Energy*, vol. 177, pp. 807-822, 2021.
- [44] G. Augsburger and D. Favrat, "From Single- to Multi-Tower Solar Thermal Power Plants: Investigation of the Thermo-Economic Optimum Transition Size," in *SolarPACES 2012 Conference on Concentrating Solar Power and Chemical Energy System*, Marrakesh, Morocco, 2012.
- [45] L. Vant-Hull, K. Lovegrove and W. Stein, "Central tower concentrating solar power (CSP) systems," in *Concentrating Solar Power Technology*, Woodhead Publishing, 2012, pp. 240-283.

- [46] A. De la Calle, A. Bayon and J. Pye, "Techno-economic assessment of a high-efficiency, low-cost solar-thermal power system with sodium receiver, phase-change material storage, and supercritical CO₂ recompression Brayton cycle," *Solar Energy*, vol. 199, pp. 885-900, 2020.
- [47] N. Blair, N. Diorio, J. Freeman, P. Gilman, S. Janzou, T. Neises and M. Wagner, "System Advisor Model (SAM) General Description," National Renewable Energy Laboratory, 2018.
- [48] M. A. Meybodi and A. C. Beath, "Impact of cost uncertainties and solar data variations on the economics of central receiver solar power plants: An Australian case study," *Renewable Energy*, vol. 93, pp. 510-524, 2016.
- [49] A. S. Alsagri, A. D. Chiasson and M. A. Gadalla, "Viability Assessment of a Concentrated Solar Power Tower With a Supercritical CO₂ Brayton Cycle Power Plant," *Journal of Solar Energy Engineering*, 2019.
- [50] IRENA, "Renewable Energy Technologies: cost analysis series. Concentrated solar power," IRENA, 2012.
- [51] F. Rovense, M. Á. Reyes-Belmonte, M. Romero and J. González-Aguilar, "Thermo-economic analysis of a particle-based multi-tower solar power plant using unfired combined cycle for evening peak power generation," *Energy*, vol. 240, 2022.
- [52] M. Bauer, "De-Risking Solar Receivers to Achieve SunShot Targets," *Energies*, vol. 15, 2022.
- [53] A. Giostri, M. Binotti, C. Sterpos and G. Lozza, "Small scale solar tower coupled with micro gas turbine," *Renewable Energy*, vol. 147, pp. 570-583, 2020.
- [54] F. Zaversky, I. Les, M. Sánchez, B. Valentin, J.-F. Brau, F. Siros, J. McGuire and F. Berard, "Techno-Economic Optimization and Benchmarking of a Solar-Only Powered Combined Cycle with High-Temperature TES Upstream the Gas Turbine," 2020.
- [55] V. Cheang, R. Hedderwick and C. McGregor, "Benchmarking supercritical carbon dioxide cycles against steam Rankine cycles for Concentrated Solar Power," *Solar Energy*, vol. 113, pp. 199-211, 2015.
- [56] M. T. Islam, N. Huda, A. Abdullah and R. Saidur, "A comprehensive review of state-of-the-art concentrating solar power (CSP) technologies: Current status and

research trends," *Renewable and Sustainable Energy Reviews*, vol. 91, pp. 987-1018, 2018.

- [57] IRENA, "Renewable Power Generation Costs in 2020," International Renewable Energy Agency, Abu Dhabi, 2021.
- [58] C. S. Turchi, M. Boyd, D. Kesseli, P. Kurup, M. Mehos, T. Neises, P. Sharan, M. Wagner and W. Timothy, "CSP Systems Analysis – Final Project Report," National Renewable Energy Laboratory, 2019.
- [59] A. Pidaparathi, "Heliostat Cost Reduction for Power Tower Plants," 2017.
- [60] R. Musi, B. Grange, S. Sgouridis, R. Guedez, P. Armstrong, A. Slocum and N. Calvet, "Techno-economic analysis of concentrated solar power plants in terms of levelized cost of electricity," in *AIP Conference Proceedings*, 2017.
- [61] UNEP, "Global Material Flows and Resource Productivity. An Assessment Study of the UNEP International Resource Panel," United Nations Environment Programme, Paris, 2016.
- [62] P. Rosado, H. Ritchie and M. Roser, "Energy," *Our World in Data*, 2022.

A Appendix A

Land purchase			
Value	Unit	Year	Reference
0.5-2.18	\$/m ²	2005	Augsburger 2013 [44]
1.0-2	\$/m ²	2012	Vant-Hull 2012 [45]
1.73	\$/m ²	2012	De la Calle 2020 [46]
2.47	\$/m ²	2017	Rea 2018 [16]
3.3	\$/m ²	2018	Puppe 2018 [13]
2.47	\$/m ²	2020	SAM – NREL 2020 [47]

Table 17 Land purchase cost by different sources

Site improvement			
Value	Unit	Year	Reference
12.46	\$/m ² _{helio}	2012	De la Calle 2020 [46]
10	\$/m ² _{helio}	2017	Rea 2018 [16]
15-21	\$/m ² _{helio}	2017	Meybodi 2017 [48]
16	\$/m ² _{helio}	2018	SolarPILOT – NREL [23]
16	\$/m ² _{helio}	2019	Alsagri 2019 [49]
16	\$/m ² _{helio}	2020	SAM– NREL 2020 [47]
$1.1 \cdot \left(\frac{A_{land}[km]}{2.8} \right)^{0.3687}$	M\$	2003	Augsburger 2013 [44]

Table 18 Site improvement cost by different sources

Heliostat			
Value	Unit	Year	Reference
196	\$/m ² (120 m ²)	2010	IRENA 2012 [50]
237	\$/m ² (<30 m ²)	2010	IRENA 2012 [50]
200	\$/m ²	2012	Vant-Hull 2012 [45]
90	\$/m ²	2012	De la Calle 2020 [46]
176	\$/m ² (1-8 m ²)	2013	García-Barberena 2013 [14]
196.7	\$/m ² (120 m ²)	2013	Augsburger 2013 [44]
90-150	\$/m ²	2017	Meybodi 2017 [48]
143	\$/m ²	2018	Sorbet 2018 [15]
145	\$/m ²	2018	SolarPILOT – NREL [23]
200	\$/m ²	2018	Conroy 2018 [36]
143	\$/m ²	2018	Puppe 2018 [13]
150	\$/m ²	2019	Alsagri 2019 [49]
100	\$/m ² (48.5 m ²)	2019	Rovense 2022 [51]
140	\$/m ² (149 m ²)	2020	SAM – NREL 2020 [47]
110	\$/m ²	2021	Bauer 2021 [52]

Table 19 Heliostat cost by different sources

Tower				
Type	Value	Unit	Year	Reference
Concrete 75-250 m	$1.6 \cdot \left(\frac{H[m]}{75}\right)^{1.797}$	M\$	2013	Augsburger 2013 [44]
Steel lattice ~ 30 m	$\frac{H[m]}{1000}$	M\$	2019	Giostri 2019 [53]
Concrete ~ 120-220 m	$3 \cdot e^{0.0113 \cdot H[m]}$	M\$	2020	SolarPilot, SAM – NREL [23]

Steel monopole 50-200 m	$1.50227 - 0.00879597 \cdot H[m] + 0.000189709 \cdot H^2$	M\$	2020	Zaversky 2020 [54]
Concrete ~ 200 m	$0.06788 \cdot H[m]$	M\$	2021	Bauer 2021 [52]

Table 20 Tower cost for different types and height by different sources

Receiver				
Value	Unit	Year	Reference	
127	\$/kW _{th}	2005	Augsburger 2013 [44]	
216	\$/kW _{th}	2014	Cheang 2015 [55]	
$3.52 \cdot (Q_{rec} [MW_{th}])^{0.44}$	M\$	2014	Lim 2017 [9]	
126.5	\$/kW _{th}	2018	Puppe 2018 [13]	
77	\$/kW _{th}	2021	Bauer 2021 [52]	
$52.0685 \cdot \frac{A_{rec} [m^2]}{560.77}$	M\$	2012	De la Calle 2020 [46]	
30	k\$/m ² ($A_{rec} < 130 \text{ m}^2$)	2020	Zaversky 2020 [54]	
50	k\$/m ² ($130 \text{ m}^2 < A_{rec} < 400 \text{ m}^2$)			
100	k\$/m ² ($> 400 \text{ m}^2$)			
$103 \cdot \left(\frac{A_{rec} [m^2]}{1571}\right)^{0.7}$	M\$	2020	SolarPILOT, SAM – NREL [23]	

Table 21 Receiver cost as function of receiver thermal power or receiver area by different sources

TES				
Type	Value	Unit	Year	Reference
2 tanks + HTF pump + Electrical heaters	15.67	\$/kWh _{th}	2012	De la Calle 2020 [46]
	22	\$/kWh _{th}	2014	Cheang 2015 [55]
	20-25	\$/kWh _{th}	2017	Rea 2018 [16]

	15.5-50	\$/kWh _{th}	2017	Meybodi 2017 [48]
	27.5	\$/kWh _{th}	2018	Puppe 2018 [13]
	24	\$/kWh _{th}	2019	Alsagri 2019 [49]
	22	\$/kWh _{th}	2020	SAM - NREL 2020 [47]
	22-24.2	\$/kWh _{th}	2021	Bauer 2021 [52]
	3300	\$/m ³	2018	Sorbet 2018 [15]
2 tanks (430 – 580 °C) + other costs	$(10.74 + 10.74 + 9.75) \cdot \left(\frac{V[m^3]}{15650}\right)^{0.8}$	M\$\$	2021	Manzolini 2021 [43]
2 tanks (550 - 730 °C) + other costs	$(10.74 + 19.34 + 9.75) \cdot \left(\frac{V[m^3]}{15650}\right)^{0.8}$	M\$		
Storage medium (Solar salts)	0.8	\$/kg		
Storage medium (NaCl-MgCl ₂)	0.25	\$/kg		

Table 22 Thermal energy storage system cost by different sources

Supercritical CO₂ power block				
Type	Value	Unit	Year	Reference
Cycle	977	\$/kW _{el}	2012	De la Calle 2020 [46]
Cycle	1140	\$/kW _{el}	2019	Alsagri 2019 [49]
Recompressed cycle (TIT 550 °C)	2493	\$/kW _{el}	2022	Morosini 2022 [22]
Recompressed cycle (TIT 700 °C)	2543	\$/kW _{el}		

Table 23 Power block cost by different sources

O&M			
Value	Unit	Year	Reference
$2.92 + 0.0151 \cdot P_{el}[MW]$	M\$/y	2014	Lim 2017 [9]
0.054	\$/kWh	2008	Augsburger 2013 [44]
0.02-0.035	\$/kWh	2010	IRENA 2012 [50]
0.031	\$/kWh	2013	García-Barberena 2013 [14]
0.02-0.04	\$/kWh	2014	IRENA 2012 [50]
0.034	\$/kWh	2017	Islam 2018 [56]
0.022	\$/kWh	2018	Sorbet 2018 [15]
0.02	\$/kWh	2020	IRENA 2020 [57]
2	%CAPEX	2019	Turchi 2019 [58]
1.5	%CAPEX	2020	Zaversky 2020 [54]

Table 24 Operation and maintenance cost by different sources

Indirect costs				
Type	Value	Unit	Year	Reference
Contingency	7	%CAPEX	2012	De la Calle 2020 [46]
	10	%CAPEX	2015	Rovense 2022 [51]
	5	%CAPEX	2016	Pidaparathi 2017 [59]
	15	%CAPEX	2017	Musi 2017 [60]
	7	%CAPEX	2018	SolarPILOT – NREL [23]
	7	%CAPEX	2019	Alsagri 2019 [49]
	7	%CAPEX	2020	SAM – NREL 2020 [47]
	11	%CAPEX	2012	De la Calle 2020 [46]
	5	%CAPEX	2014	Pidaparathi 2017 [59]

Engineering, procurement, and construction (EPC)	11	%CAPEX	2019	Alsagri 2019 [49]
	13	%CAPEX	2020	SAM – NREL 2020 [47]
Installation	15	%CAPEX	2015	Rovense 2022 [51]
Project	15	%CAPEX	2018	Sorbet 2018 [15]
Insurance	0.5-1	%CAPEX	2010	IRENA 2012 [50]
	0.4	%CAPEX	2017	Musi 2017 [60]
	0.5	%CAPEX	2019	Turchi 2019 [58]
	0.5	%CAPEX	2020	SAM – NREL 2020 [47]

Table 25 Indirect costs for different categories by different sources

List of Figures

Figure 1 Workflow of the thesis work.....	2
Figure 2 World primary energy consumption by source [1]	3
Figure 3 Share of global electricity generation by source [2]	4
Figure 4 Energy-related and process CO ₂ emissions, 2010-2050 and temperature rise in 2100 by scenario [3]	5
Figure 5 Total installed capacity and electricity generation by source in the NZE scenario, 2010-2050 [3]	6
Figure 6 Flexibility needs and supply by region and scenario [3]	6
Figure 7 CSP projects around the world, 2020 [7]	8
Figure 8 Concentrated solar thermal power global capacity, by country and region [8]	8
Figure 9 Global weighted-average LCOEs from newly commissioned, utility scale renewable power generation technologies [8]	9
Figure 10 Main CSP technologies [6].....	10
Figure 11 The Ivanpah Solar Electric Generating System	10
Figure 12 Molten-salt power tower with direct storage of salts [5]	11
Figure 13 Falling particle receiver system with integrated storage and heat exchange for a power cycle [5].....	13
Figure 14 Conceptual design of gas-phase receiver system with a modular indirect PCM thermal storage system [5]	13
Figure 15 Modular field layout	16
Figure 16 Considered heliostat field layouts for a 100 MW _{el} , 8 hours storage plant...	17
Figure 17 Plant layout of the multi tower system.....	20
Figure 18 Scheme of the proposed plant concept	21
Figure 19 General scheme of the DSCC concept (only one representative tower-receiver-gas turbine unit is shown)	23
Figure 20 Solar thermal to electricity via advanced latent heat storage (STEALS) plant scheme.....	25

Figure 21 Lake Cargelligo power plant.....	28
Figure 22 Sierra SunTower Facility.....	29
Figure 23 Module 1 of Yumen Xinneng power plant	29
Figure 24 Methodology flow chart	32
Figure 25 Radial stagger layout method	34
Figure 26 Cornfield layout method	34
Figure 27 Example of field layout obtained with SolarPILOT	36
Figure 28 Example of a receiver heat flux map obtained from SolarPILOT.....	36
Figure 29 Example of results obtained from SolarPILOT.....	37
Figure 30 Thermal resistance network in the case of two circumferential control volume for each quarter of circumference [22]	40
Figure 31 Example of receiver tube diameter optimization for a cylindrical receiver	43
Figure 32 Discretization analysis for a 4.5 m x 4.5 m billboard receiver	44
Figure 33 Required number of control volumes for different receiver sizes.....	45
Figure 34 Discretization analysis of the multi-pass receiver model for different receiver sizes	46
Figure 35 Modular field modelled layout.....	47
Figure 36 Input matrix for a possible 12 modules plant layout.....	47
Figure 37 Expansion loop.....	53
Figure 38 Loss coefficients $\xi_{c.st}$ and $\xi_{c.s}$ as function of flow rates and pipe sections and converging tee scheme [32]	56
Figure 39 Diverging tee scheme	56
Figure 40 Piping system losses as function of HTF velocity	58
Figure 41 Example of optical efficiency map as function of azimuth and elevation angles.....	60
Figure 42 Receiver pressure drops and thermal efficiency as function of receiver thermal power input.....	61
Figure 43 HTF pump electric consumption and piping thermal efficiency as function of receiver thermal power input	62
Figure 44 Work flow scheme of the first part of the case study (Section 3.3), on the left, and of the second part of the case study (Section 3.4), on the right.....	68
Figure 45 Aerial picture of Jemalong power plant	69
Figure 46 Jemalong plant scheme [37].....	69

Figure 47 Time series of transient DNI and receiver outlet temperature, 13 May 2019 [38]	71
Figure 48 Alternative solar field layouts considered	72
Figure 49 Layout configurations initially considered	75
Figure 50 Layout configurations considered after the cornfield layout is discarded .	75
Figure 51 Solar multiple and TES size optimization as function of LCOE for the temperature range 430-580 °C	78
Figure 52 Solar multiple and TES size optimization as function of LCOE for the temperature range 550-730 °C	78
Figure 53 Annual efficiencies and investment cost as function of solar multiple for plants in the temperature range 550-730°C at optimal TES size	79
Figure 54 Optimization of the diameter of the receiver tubes operating in the temperature range 550-730°C	81
Figure 55 Design powers and efficiencies of the four optimal configurations.....	82
Figure 56 Annual energy and efficiencies of the four optimal configurations.....	83
Figure 57 Optical efficiency map of modular field and shading efficiency for zenith angle equal to 15° and azimuth angle equal to 100°	83
Figure 58 Receiver and piping off design efficiencies for the plants operating in the temperature range 550-730°C	84
Figure 59 Investment costs of the four optimal configurations.....	85
Figure 60 Module optical efficiency, thermal efficiency and LCOH as function of receiver size and tower height.....	86
Figure 61 Single field optical efficiency, thermal efficiency and LCOH as function of receiver size and tower height.....	86
Figure 62 Design and annual efficiencies and specific capex of the two optimal configurations	88
Figure 63 Optical efficiency map of the three optimal configurations	89
Figure 64 Annual optical efficiency for different tower height, receiver area, module power and module layout.....	90
Figure 65 Annual optical efficiency as function of receiver area for different module layouts.....	90
Figure 66 Annual receiver thermal efficiency for different tower height, receiver area, module power and module layout	91

Figure 67 Annual receiver thermal efficiency as function of receiver area for different module layouts	91
Figure 68 Annual optical-thermal efficiency as function of receiver area for different module layouts	92
Figure 69 Receiver area and tower height that maximize the optical-thermal efficiency for each module size (expressed as thermal power incident on the receiver)	92
Figure 70 Interpolated values of optical efficiency and thermal efficiency in the regions close to the computed points for the modular surrounded layout.....	93
Figure 71 LCOH as function of tower height and receiver area for the radial circular and the surrounded layouts.....	94
Figure 72 LCOH values of the three modular layouts and the two optimal single field configurations	95
Figure 73 Receiver area and tower height that minimize the LCOH for each module layout.....	95
Figure 74 Piping annual thermal efficiency as function of solar multiple and number of modules for the radial circular layout optimal geometries	96
Figure 75 Piping annual thermal efficiency as function of number of modules and power of the module for the radial circular layout	97
Figure 76 Annual solar to electric efficiency as function of solar multiple and number of modules, for the radial circular and the surrounded layouts	98
Figure 77 LCOE as function of SM and TES size for the 5 MW _{th} module and optimal TES size as function of SM and module power for the radial circular layout.....	99
Figure 78 LCOE as function of solar multiple for different module power and layout with optimized TES size	99
Figure 79 Optimal solar multiple and number of modules for each considered layout	100
Figure 80 LCOE values of the optimal modular and single field configurations.....	100
Figure 81 Annual efficiencies and specific investment cost for the optimal modular and single field configurations.....	102
Figure 82 Effect of power block size on optimal solar multiple and number of modules for the three different module layouts	102
Figure 83 LCOE for different layouts, different module sizes and different power block sizes	103
Figure 84 Effect of piping cost variation on optimal solar multiple and number of modules for the three different module layouts.....	103

Figure 85 LCOE for different layouts, different module sizes and different piping cost
..... 104

List of Tables

Table 1 Summary of research articles on modular solar tower plants	15
Table 2 Mirror performance parameters [23]	35
Table 3 Optical parameters of the receiver model [22]	39
Table 4 Input parameters of the receiver model	40
Table 5 Tube diameters and corresponding thickness considered for the optimization	42
Table 6 Thermal properties of piping materials [28]	49
Table 7 Concentrated loss elements and types	55
Table 8 Piping costs	65
Table 9 Cost assumptions for the comparison of the plants	66
Table 10 Considered heliostat layouts and their design optical performances	77
Table 11 Main parameters of the modular and single field plants operating in the temperature range 430-580 °C	80
Table 12 Main parameters of the modular and single field plants operating in the temperature range 550-730 °C	81
Table 13 Performance and economic parameters of the four optimal configurations	85
Table 14 Main parameters and performance indicators of the two optimal configurations	87
Table 15 Results of different optimized solar field layouts	89
Table 16 Main parameters and performances of the modular and single field optimal configurations	101
Table 17 Land purchase cost by different sources	113
Table 18 Site improvement cost by different sources	113
Table 19 Heliostat cost by different sources	114
Table 20 Tower cost for different types and height by different sources	115
Table 21 Receiver cost as function of receiver thermal power or receiver area by different sources	115

Table 22 Thermal energy storage system cost by different sources.....	116
Table 23 Power block cost by different sources	116
Table 24 Operation and maintenance cost by different sources.....	117
Table 25 Indirect costs for different categories by different sources	118

